

**NUMERICAL MODELLING OF SOIL-STRUCTURE INTERACTION
USING EFFICIENT RADIATING BOUNDARY CONDITIONS**

*Thesis submitted in partial fulfillment
of the requirements for the degree*

of

Doctor of Philosophy

in

Civil Engineering



**INTERNATIONAL INSTITUTE OF
INFORMATION TECHNOLOGY**

HYDERABAD

International Institute of Information Technology Hyderabad
(Deemed to be University)
Hyderabad - 500 032, INDIA
February -2023

International Institute of Information Technology
Hyderabad, India

CERTIFICATE

It is certified that the work contained in this report, titled “**Numerical Modelling of Soil-Structure Interaction using Efficient Radiating Boundary Conditions**” by Mr. Ravi Shankar Badry, has been carried out under my supervision and is not submitted elsewhere for a degree.

March-2023

Advisor: Prof. Pradeep Kumar Ramacharla
Professor of Civil Engineering
Earthquake Engineering Research Centre
International Institute of Information Technology
Hyderabad 500032
India

Acknowledgements:

This PhD thesis could not have been possible without the assistance, understanding, and guidance rendered by numerous people throughout the tenure. First and foremost, I express my appreciation and sincere gratitude to my supervisor, Prof. Pradeep Kumar Ramacharla, for his continuous support of my PhD study and research and for his patience, motivation, enthusiasm, and immense knowledge. His guidance helped me throughout the research and writing of this thesis.

I am very thankful to my thesis committee, Prof. M. Venkateswarlu (IIIT -Hyderabad), Dr. Rehana Shaik (IIIT -Hyderabad), Dr. Suresh Das (IISER) and Dr. Surendra Nath Somala (IIT -Hyderabad) for reviewing the PhD research proposal and giving the valuable suggestions.

I am thankful to get constant encouragement and support from all my research colleagues, the staff of the Earthquake Engineering Research Centre (EERC) and my colleagues at ARUP. Special thanks go to Maruti Kotti for his remarkable help in clearing the technical doubts. Also, I extend my sincere regards to all non-teaching staff at IIIT-H for their timely help.

Words are not enough to thank my family for the support they have given during this long and sometimes very difficult journey. I am very thankful to my beloved wife, Dr. Pallavi Badry, for her love and continuous support that have been given during this long and sometimes very difficult journey. The special thanks go to my kids, Dhriti and Bhargav, for adjusting to the difficult times they came across during the PhD course work and the research.

Abstract

Since the 1964 Niigata earthquake (the epicentre is located at the continental shelf off the northwest coast of Honshu, Japan), dynamic soil-structure interaction has been considered an important factor in many important structures such as tall buildings, bridges, nuclear power plants, etc. As soil-structure interaction analysis is a complex phenomenon, researchers have developed different techniques through experimental, analytical, and numerical approaches. Amongst all the techniques numerical methods are found more reliable in the design of structures to include the effects of soil-structure interaction. However, radiating waves from structure are one of the major concerns in numerical modelling of the soil-structure interaction.

To solve the radiating wave propagation problems using finite element analysis (FEA), it is required that the boundary must be terminated at some finite location. This truncation of the model at the finite boundary will cause the reflection of radiating waves. The reflected waves from the boundary will affect the solution and may lead to instabilities in the numerical analysis. Therefore, it is necessary to provide an artificial boundary condition that will transmit the outwardly propagating waves with minimal or negligible reflections.

The primary objective of this research is to develop an efficient radiating boundary condition for numerical simulation of wave propagation in nonlinear, unbounded spatial domains. Despite several attempts by the researchers, the challenge of developing a computationally efficient absorbing boundary condition (ABC) to resemble the Sommerfeld radiation condition has not been well addressed.

Absorbing Boundary Conditions (ABC), also called Local Absorbing Boundary Conditions are simple and computationally efficient, but they produce spurious reflections when the wave impinges on the boundary in a direction other than the normal. Absorbing layer techniques are efficient in absorbing outwardly propagating wave energy, but these techniques require many layers. Researchers have also attempted to combine the Absorbing Boundary Conditions (ABC) with the Layers by Increasing Damping (ALID) to utilize the advantages of both methods. Since ABC is only applicable to wave propagation in elastic media, the attempt to combine the two techniques becomes unsuccessful due to an impedance mismatch.

In this thesis, a new absorbing boundary condition for wave propagation in a viscoelastic medium (VABC) is proposed. The method is an extension of the standard ABC proposed by Lysmer and Kuhlemeyer (1969). The proposed method does not converge to Kelvin-type viscoelastic materials but can be applied to Maxwell-type viscoelastic materials, i.e., only mass proportional damping is considered. The accuracy of the method is studied for viscoelastic wave propagation problems, and the results are compared with the standard ABC and analytical solutions.

The analytical and numerical results show that the VABC boundary conditions are promising in absorbing the wave energy when the damping ratio is less than 20% and produces the reflections when damping ratio is more than 20% due to dropping the higher order terms in the expansion. The VABC produces spurious reflections when the waves are not impinging in

the normal direction, and reflections increase as the angle between the wave propagation and the normal direction increases.

The study extends to provide an efficient absorbing method by combining VABC boundary conditions with Absorbing Layers by Increase in Damping (ALID). The main objective of ALID is to attenuate the reflected waves from VABC in cases of angle incidence. The combination of ALID and VABC, i.e., ALID+VABC, is achieved by matching the impedance of VABC with the last layer of ALID.

Results from ALID+VABC are compared with other methods such as ABC, ALID, and SRM (Stiffness Reduction Method). A sensitivity analysis is carried out to verify the efficiency of absorbing the propagation wave energy at various loading frequencies. ALID+VABC has been found to be numerically efficient across a wide range of loading frequencies when compared to the other methods. The method also requires shorter absorbing region lengths, which allows for a smaller number of absorbing layers. However, all the absorbing layer methods such as ALID, ALID+VABC, SRM, and PML are poor at allowing smooth propagation of the wave through layers when waves are entering at a higher incident angle.

Dynamic Soil-Structure-Interaction analysis is carried out on a three-dimensional tall building with 20 stories using ABC, ALID, and ALID+VABC as a radiating boundary condition. The complete Soil-Structure-Interaction (SSI) analysis is carried out in two stages. First, a nonlinear static analysis is carried out with gravity loading. The absorbing layers in ALID and ALID+VABC were also present in the static analysis since the damping properties did not influence the analysis. Later, nonlinear dynamic analysis is carried out using El Centro earthquake loading. The Domain Reduction Method is used to apply the earthquake motion. 1D wave propagation is used to obtain the forces for free-field motion at the boundary interface, and these forces are applied in dynamic analysis.

Static analysis results show that the model with absorbing layers, i.e., ALID and ALID+VABC, produces more displacements compared to ABC since the finite elements in the absorbing layers are subjected to gravitational loads (dead loads) from above. This proves that the absorbing layers can be used to reduce the actual model domain if they are modelled appropriately so that the size of the resulting model will not be increased with ALID and ALID+VABC.

The time history response of the structure under El Centro earthquake loading (the earthquake occurred in the Imperial Valley in south-eastern Southern California in 1940) shows that ALID and ALID+VABC perform better than ABC boundary conditions. The study also shows that ALID and ALID+VABC work well even if the absorbing medium length is 0.33λ . However, a minimum of 30 layers are recommended in the absorbing region.

Table of Contents

Acknowledgements:.....	IV
Abstract.....	V
Table of Contents.....	VII
List of Figures.....	X
List of Tables.....	XII
Symbols.....	XIII
Abbreviations.....	XVI
1. INTRODUCTION.....	1
1.1 Theory and background.....	1
1.2 Method of Analysis.....	2
1.2.1 Direct Method.....	2
1.2.2 Multistep Method.....	3
1.3 Major challenges.....	5
1.4 Scope and Objectives of the study.....	6
1.5 Organization of the Thesis.....	6
2. Literature Review.....	8
2.1 Introduction.....	8
2.2 Absorbing boundary conditions.....	8
2.3 Absorbing layer techniques.....	10
2.4 Boundary element methods.....	12
2.5 Infinite element methods.....	12
2.6 Conclusions.....	13
3. Finite element displacement-based formulation.....	14
3.1 Introduction.....	14
3.2 Principle of virtual work.....	14
3.3 Finite element discretization.....	14
3.4 Solution for the nonlinear dynamic equilibrium equations.....	16
3.4.1 Nonlinear static analysis.....	16
3.4.2 Nonlinear dynamic analysis.....	18
3.5 Contact interfaces.....	19
3.5.1 Introduction:.....	19
3.5.2 Penalty based node to node contact element.....	20

3.5.3	Algorithm for nonlinear static analysis.....	21
3.5.4	Algorithm for nonlinear dynamic analysis.....	23
3.6	Material Modelling.....	24
3.6.1	Linear elastic material:.....	24
3.6.2	Elastic-Plastic Materials.....	25
3.6.3	Viscoelastic Materials:.....	29
3.7	Summary.....	31
4.	Absorbing Boundary Conditions for wave propagation in.....	32
	Viscoelastic materials (VBAC).....	32
4.1.	Introduction.....	32
4.2.	Theory and Formulation of the method.....	32
4.3.	Effect of higher-order terms.....	34
4.4.	Convergence analysis.....	35
4.4.1.	Effect of Rayleigh damping parameters and frequency content on the convergence	36
4.4.2	Rheological interpretation of mass proportional damping.....	36
4.5	Numerical examples.....	37
4.5.1.	1D p-wave propagation.....	37
4.5.2.	2D scalar P-wave propagation.....	42
4.5.3.	2D viscoelastic wave propagation.....	48
5.	Absorbing Layers combined with VABC (ALID+VABC).....	54
5.1	Introduction.....	54
5.2.	Theory.....	54
5.2.1	Absorbing Layers by Increasing Damping (ALID).....	54
5.2.2	Combining ALID and VABC.....	55
5.3.	Numerical examples.....	56
5.3.1.	1D p-wave propagation.....	56
5.3.2.	2D scalar P-wave propagation.....	64
5.3.3.	2D wave propagation:.....	68
5.4.	Conclusions:.....	71
6.	Numerical modelling of Soil-Structure-Interaction for Tall Building.....	72
6.1	Introduction.....	72
6.2	Model details:.....	73
6.2.1	Superstructure:.....	73
6.2.2	Substructure and Foundation:.....	75

6.2.3 Soil Modelling and interface Modelling:.....	75
6.3 Numerical analysis:.....	75
6.3.1 Static analysis.....	77
6.3.2 Dynamic Analysis.....	80
6.4. Conclusions.....	82
7. Summary.....	84
7.1 Summary.....	84
7.2 Conclusions.....	84
7.3 Limitations of the Study.....	85
7.4 Suggestions for future work.....	86
7.5 Research Contributions.....	86
8. References:.....	87
APPENDIX A: Finite Element Formulation.....	91
A.1: Finite Element Formulation for 8-Node brick element.....	91
A.2: 4-Node quadrilateral element for plane strain condition.....	94
A-3: Formulation of beam element.....	95

List of Figures

Figure 1.1. Soil structure interaction effect and wave propagation (Maheshwari 2004)	2
Figure 1.2. Direct Method of Soil structure interaction analysis (Kramer, 1996)	3
Figure 1.3. Kinematic interaction for vertically propagating S wave (Kramer, 1996).	4
Figure 1.4. Inertial interaction (Kramer, 1996).	4
Figure 2.1. Absorbing boundary conditions	9
Figure 2.2. Energy ratios for incident P and S wave ($\nu=0.25$) (Georges, 2011)	9
Figure 2.3. Energy ratios for various Poisson's ratios ν (Georges, 2011)	9
Figure 2.4. PML adjacent to a truncated domain attenuates an outgoing wave.	11
Figure 2.5. 2D plane strain model with absorbing later boundary (Semblat et al., 2010)	12
Figure 3.1. Iterative procedure for Initial Stiffness Method	18
Figure 3.2. Time marching of central difference explicit solver	18
Figure 3.3. Thin interface elements (Desai, 1984)	19
Figure 3.4. Node-to-node interface element (Katona, 1983)	20
Figure 3.5. Contact friction idealization using springs in the Penalty Method	21
Figure 3.6. Mohr-Coulomb and Drucker-Prager failure surfaces	26
Figure 3.7. Isotropic hardening	26
Figure 3.8. Kinematic hardening	27
Figure 3.9. Schematic representation of Radial return mapping	28
Figure 3.10. Hysteresis of stress-strain curve for Elastic and Viscoelastic deformations	30
Figure 3.11. Mechanical models of viscoelastic materials	30
Figure 4.1. The convergence of Taylor Series for $1 - x$ for the different degree of polynomials	35
Figure 4.2. Configuration for one-dimensional wave propagation model	37
Figure 4.3. Displacements at different locations for 5%, 10% and 20% damping ratios	39
Figure 4.4. Reflections near the boundary ($L=990m$)	40
Figure 4.5. Displacements at $L=990m$ for 5%, 10% and 20% damping ratios	41
Figure 4.6. Reflections near the boundary ($L=990m$)	41
Figure 4.7. 2D Plane strain model for the pure P-Wave propagation	42
Figure 4.8. Source field displacement for the finite element model	42
Figure 4.9. Displacements at 3.50 m radius: (a) $\alpha = 1$, (b) $\alpha = 2$, (c) $\alpha = 4$ and (d) $\alpha=5$	43
Figure 4.10. Displacements at 4.0 m radius (a) $\alpha = 1$, (b) $\alpha = 2$, (c) $\alpha = 4$ and (d) $\alpha=5$	43
Figure 4.11. Snapshot of Pressure distribution (N/m^2) when damping coefficient, $\alpha = 1$: (a) time $t=2sec$, (b) time $t=3sec$ (c) time $t=3.2sec$ and (d) time $t=3.5sec$	45
Figure 4.12. Snapshot of Pressure distribution (N/m^2) when damping coefficient, $\alpha = 2$: (a) time $t=2sec$, (b) time $t=3sec$ (c) time $t=3.2sec$ and (d) time $t=3.5sec$	46
Figure 4.13. Snapshot of Pressure distribution (N/m^2) when damping coefficient, $\alpha = 4$: (a) time $t=2sec$, (b) time $t=3sec$ (c) time $t=3.2sec$ and (d) time $t=3.5sec$	47
Figure 4.14. 2D Plane strain model for wave propagation	48
Figure 4.15. Displacements in Y direction at A: (a) damping coefficient, $\alpha = 10$, (b) $\alpha = 15$	48
Figure 4.16. Displacements in Y direction at B: (a) damping coefficient, $\alpha = 10$, (b) $\alpha = 15$	49
Figure 4.17. Displacements in X direction at C: (a) damping coefficient, $\alpha = 10$, (b) $\alpha = 15$	49
Figure 4.18. Displacements in Y direction at C: (a) damping coefficient, $\alpha = 10$, (b) $\alpha = 15$	50

Figure 4.19. Snapshot of pressure distribution (N/m^2) when damping coefficient, $\alpha = 10$: (a) time $t=0.8$ sec, (b) time $t=1.0$ sec and (c) time $t=1.1$ sec	51
Figure 4.20. Snapshot of shear stress distribution (N/m^2) when damping coefficient, $\alpha = 10$: (a) time $t=1.4$ sec, (b) time $t=2.1$ sec and (c) time $t=2.5$ sec	52
Figure 5.1: Wave propagation angle change when propagating through absorbing layers	55
Error! Bookmark not defined.	
Figure 5.2. Configuration for one-dimensional wave propagation model	57
Figure 5.3. Forces at 5m: a) full-time record and b) zoomed response	58
Figure 5.4. Displacement at 5m: a) full-time record b) zoomed response	58
Figure 5.5: Forces at middle of AoS i.e., at 200 m	59
Figure 5.6: Maximum percentage of reflections	60
Figure 5.7. Forces at 5m for 1.5λ and λ : a) full time record, and b) zoomed response	61
Figure 5.8. Displacements at 5m for 1.5λ and λ : a) time history, and b) zoomed response	61
Figure 5.9. Percentage of reflection vs load frequency for 1D wave propagation	63
Figure 5.10. Percentage of reflection vs load frequency	64
Figure 5.11. 2D Plane strain model for pure P-Wave propagation	64
Figure 5.12. Displacements at 3.50 m radius	65
Figure 5.13. Displacements vs load frequency at 3.50m radius	65
Figure 5.14. Snapshot of pressure distribution (N/m^2) at time $t = 5.5$ sec	67
Figure 5.15. Percentage of reflection vs load frequency for 2D scalar wave propagation	68
Figure 5.16: 2D plane strain model for wave propagation in an infinite domain	68
Figure 5.17: Snapshot of Pressure distribution (N/m^2) @2.38 sec	70
Figure 5.18: 2D plane strain model for wave propagation in an infinite domain	70
Figure 5.19: Reflection coefficients for ALID, VABC and SRM	71
Figure 6.1: Plan view of Finite Element Model Superstructure	72
Figure 6.2: Full soil structure interaction model	74
Figure 6.3: Substructure and Foundation system	74
Figure 6.4: 3D Numerical Modelling of Soil	75
Figure 6.5: Interface boundary layer for seismic loading using DRM approach	76
Figure 6.6: Acceleration Time History applied at the interface layer	77
Figure 6.7: z-displacements (m) under self-weight a). ABC b) ALID and ALID+VABC	78
Figure 6.8: z-displacements (m) at raft level under self-weight a). ABC b) ALID and ALID+VABC	79
Figure 6.9: Displacement time history at the top centre of the building	80
Figure 6.10: Displacement time history at the Pile Top near the centre of the building	81
Figure 6.11: Storey displacement contour in ABC, ALID and ALID+VABC configurations	81
Figure 6.12: Storey drift in ABC, ALID and ALID+VABC configurations	82
Figure A-1: 8 noded 3-D brick element in parent coordinate system	91
Figure A-2: 4-Node quadrilateral element	94

List of Tables

Table 4.1. Mass proportional damping for different damping ratios	38
Table 4.2. Maximum reflections for different damping ratios	40
Table 5.1. One dimensional model parameters:	62

Table 6.1: Material Properties
Table 6.2: Details of columns

73
73

Symbols

Scalars

a	Dimensionless constant for absorbing boundary condition
b	Dimensionless constant for absorbing boundary condition
E	Youngs modulus
\acute{E}	Complex Youngs modulus
E_0	Seismic waves that are reaching soil-foundation interface
E_1	Transmitted seismic waves through soil-foundation interface into the structure
f_x	Force in x direction
f_y	Force in y direction
f_z	Force in z direction
F_0	Reflected waves from soil foundation interface
F_1	Waves returned from the top of structure travelling downwards
F_2	Waves from the structure reflected at foundation and soil interface
$F_{(\sigma)}$	Yield criterial for nonlinear material
$G_{(\sigma)}$	Potential flow criteria for nonlinear materials
H	Shape function
i	Imaginary Number
J_{2D}	Second invariant of the deviatoric stress
k_x	Stiffness in x direction
k_y	Stiffness in y direction
k_z	Stiffness in z direction
$p_{(\sigma)}$	Hydrostatic pressure
R_1	Radiating waves
u	displacement in x direction
\hat{u}	displacement in x direction in element local axis
\acute{u}	velocity in x direction
v	displacement in y direction

\hat{v}	displacement in y direction in element local axis
\dot{v}	velocity in y direction
V_p	primary wave velocity
V_s	shear wave velocity
w	displacement in z direction
\hat{w}	displacement in z direction in element local axis
\dot{w}	velocity in z direction
$W_{f \square}$	Total internal stored strain energy
α	Mass proportional Rayleigh damping coefficient
β	Mass proportional Rayleigh damping coefficient
ζ	Damping ratio
θ	Friction angle
μ	Friction coefficient
ν	Poisons ratio
ρ	Mass density
$\hat{\rho}$	Complex mass density, consist of real and imaginary parts of density.
σ	Normal stress
τ	Shear stress
φ	Dilatancy angle
ω	Angular frequency
ω_d	Design angular frequency

Vectors

f^b	External body force vector
f^e	External force vector
f^i	Internal force vector
f^s	External surface traction vector
N	Direction of plastic flow $N = \frac{dG_{(\sigma)}}{d\sigma}$
s	Deviatoric stress $s = \sigma - p_{(\sigma)}I$
x	directional vector $x = \{x, y, z\}$

u	Nodal displacement vector
\bar{u}	Virtual displacements vector
\hat{u}	Node displacements vector in element local axis
u_{II}	Nodal displacement vector due to inertial interaction alone
u_{KI}	Nodal displacement vector due to kinematic interaction alone
\dot{u}	Nodal velocity vector
\ddot{u}	Node acceleration vector
\dot{u}_{ff}	Free field acceleration vector
\dot{u}_{KI}	Nodal acceleration vector due to kinematic interaction alone
\dot{u}_{II}	Nodal acceleration vector due to inertial interaction alone
\dot{u}_b	Nodal acceleration vector due to seismic at the seismic boundary
ε	Strain vector $\varepsilon = \left\{ \varepsilon_{xx}, \varepsilon_{yy}, \varepsilon_{zz}, \varepsilon_{zy}, \varepsilon_{zx}, \varepsilon_{xy} \right\}^T$
ε^p	Plastic strain vector
$\bar{\varepsilon}$	Virtual strains vector
σ	Stress vector $\sigma = \left\{ \sigma_{xx}, \sigma_{yy}, \sigma_{zz}, \sigma_{zy}, \sigma_{zx}, \sigma_{xy} \right\}^T$
σ_{tr}	Trial stress vector
Δf	Balance force vector
Δu	Incremental displacement vector
$\Delta \dot{u}$	Incremental velocity vector
$\Delta \ddot{u}$	Incremental acceleration vector

Matrices

B	Strain-displacement matrix
C	Damping matrix
D	Elastic Stress-Strain Matrix
H	Shape function matrix
I	3x3 Identity matrix
K	Stiffness matrix
\dot{K}	Complex stiffness matrix
M	Mass matrix

\hat{M} Complex mass matrix

Abbreviations

ABC	Absorbing Boundary Conditions or Local Absorbing Boundary Conditions
ALID	Absorbing Layers by Increase in Damping
ALID+VABC	Absorbing Layers by Increase in Damping Combined with Absorbing Boundary Conditions for Viscoelastic Wave Propagation
CALM	Caughey Absorbing Layer Method
FEA	Finite Element Analysis
MNRM	Modified Newton Raphson Method
NRM	Newton Raphson Method
PML	Perfectly Matched Layers
SSI	Soil-Structure-Interaction
VABC	Absorbing Boundary Conditions for Viscoelastic Wave Propagation
VSAB	Viscous Spring Artificial Boundary

1. INTRODUCTION

Since the 1964 Niigata earthquake (the epicentre is located at the continental shelf off the northwest coast of Honshu, Japan), dynamic soil-structure interaction has been considered an important factor in many important structures such as tall buildings, bridges, nuclear power plants, etc. As soil-structure interaction analysis is a complex phenomenon, researchers have developed different methodologies such as experimental, analytical, and numerical approaches. Amongst all the methodologies numerical methods are found more reliable in the design of structures to include the effects of soil-structure interaction. However, the major challenge in numerical simulation is modelling the semi-infinite soil medium.

In this chapter, a brief introduction to theoretical aspects of soil-structure interaction, including radiating boundary conditions and the major challenges involved, is presented along with a problem statement.

1.1 Theory and background

The classical theory of soil-structure interaction was established in the early 1960s. Earlier, structures were assumed to be fixed at their bases in the process of analysis and design under dynamic loading. However, structures are supported by the soil. When the soil support is included in the dynamic analysis, its flexibility reduces the overall stiffness of the combined system and increases the time period of the system. The change in the natural period may alter the seismic response significantly.

The effects of SSI have been illustrated in Figure 1.1. When the seismic wave (E0) generated by the fault motion reaches the foundation, it is separated into two types: transmitted waves (E1) and reflected waves (F0). The transmission waves travel through the building, reach the top of the building, and travel back towards the foundation shown as F1. At this stage, the structure-soil-structure interaction phenomenon takes place. Some of the waves will be transmitted into the ground, while the rest will be reflected into the structure as F2. The waves that are transmitted to the soil are known as radiating waves, shown as R1. The seismic waves reflected into the structure continue to be trapped in the structure, and the structure starts to vibrate continuously for a long time.

In numerical simulation of soil-structure interaction analysis, modelling a semi-infinite soil medium is not feasible, and hence it has to truncate at a finite distance. However, the major concern is the radiating waves; when these waves reach the truncated boundary, they will be reflected into the domain and cause errors in the analysis results. Also, modelling a large domain to avoid reflections causes an increase in the computational memory requirement as well as the time required for dynamic analysis. Therefore, radiating boundary conditions must be applied around the soil model to absorb all the outwardly propagating waves without reflecting into the soil medium.

There are many methods to model the radiating boundary conditions. Each of these methods has its own advantages and disadvantages. Detailed discussions on the existing radiating boundary conditions are presented along with the literature reviews in Chapter 2.

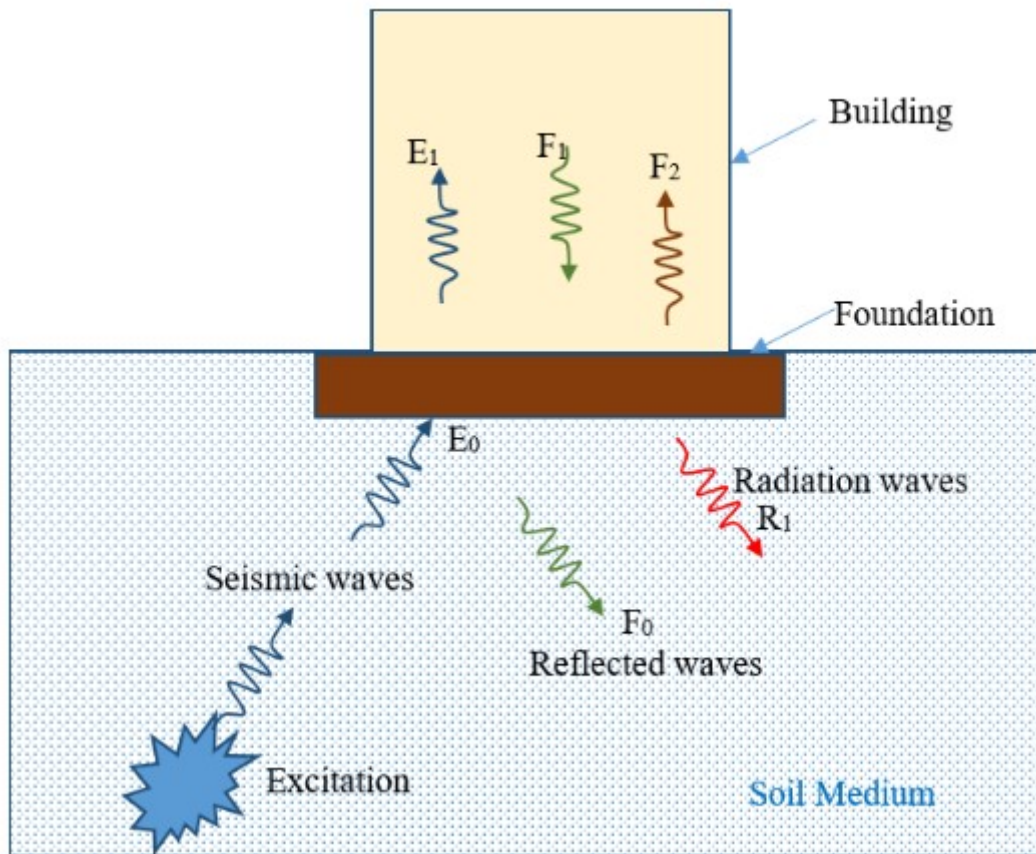


Figure 1.1. Soil structure interaction effect and wave propagation (Maheshwari 2004)

1.2 Method of Analysis

Dynamic analysis of SSI can be done using the direct method and the substructure method. Details of these methods are explained in this section.

1.2.1 Direct Method

In the direct method, the soil and structure are modelled together in a single step. Free-field input motions are specified along the base and sides of the models, as shown in Figure 1.2, and the resulting response of the interacting system is computed from the equation of motion.

$$M \dot{u} + Ku = -M \dot{u}_{ff} \quad (1.1)$$

Where M and K are the system mass and stiffness, \dot{u} and u are the nodal accelerations and displacements and \dot{u}_{ff} are the specified free-field accelerations at the boundary nodes.

The major drawback of this method is modelling large soil domain and analysis time to apply free-field motion and to avoid reflections of radiation waves. However, the recent advances like Domain Reduction Method (Bielak et al., 2003; Yoshimura et al., 2003) and Effective Seismic Input Method with suitable radiating boundary conditions reduces the requirement of soil model size.

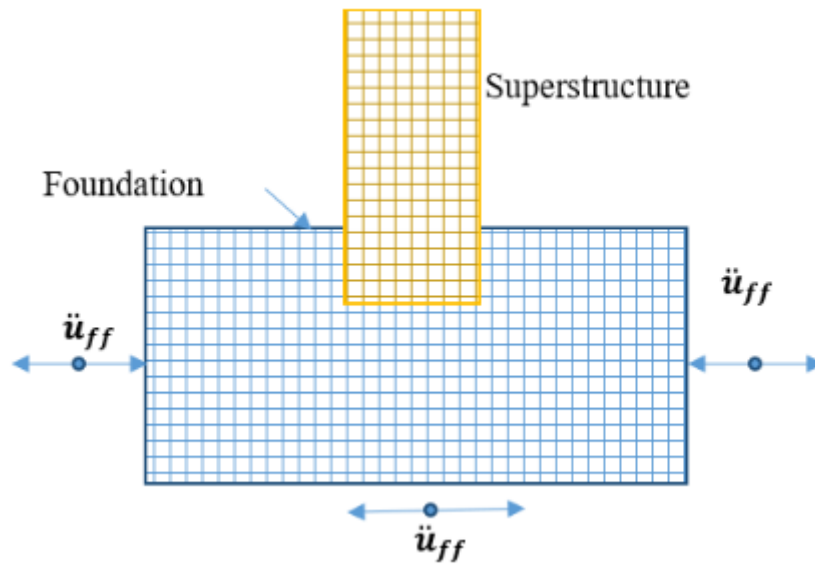


Figure 1.2. Direct Method of Soil structure interaction analysis (Kramer, 1996)

1.2.2 Multistep Method

In the substructure or multistep method, the analysis is split into multiple steps based on the principle of superposition to isolate the two primary actions of SSI (Wolf, 1985). Basically, the dynamic soil-structure interaction consists of two interactions, namely, kinematic interaction and inertial interaction.

Kinematic Interaction

Kinematic interaction is a scattering phenomenon due to a mismatch in the dynamic impedance between the foundation structure and the surrounding soil. However, the foundation stiffness is different from that of the adjacent soil, and this causes reflection and refraction of the incoming seismic waves as these waves pass through the soil-foundation interface. Therefore, the kinematic interaction represents the structural response due to the free-field ground motion, including the scattering effects. The magnitude of the phenomenon depends on the geometry of the structure, the foundation size and embedment, the kinematics of the incident free-field motion, and the angle of incidence of the seismic waves. As a special ideal case, no kinematic interaction occurs if the foundation is built at the ground surface (i.e., a shallow foundation) with matching impedance of foundation soil and is hit by a vertically propagating Shear wave (Figure 1.3).

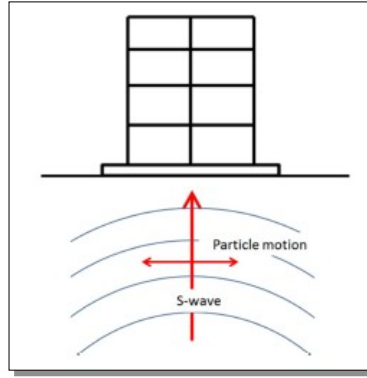


Figure 1.3. Kinematic interaction for vertically propagating S wave (Kramer, 1996).

The deformations due to kinematic interaction alone can be computed assuming that the foundation has stiffness but no mass. The equation of motion for kinematic interaction is

$$M_{soil} \dot{u}_{KI} + K u_{KI} = - M_{soil} \dot{u}_b \quad (1.2)$$

Where, M_{soil} is the mass of the soil system assuming that the structure, and foundation are massless and \dot{u}_b are nodal accelerations due to seismic at the seismic boundary.

Inertial Interaction

When the system gets excited, the mass of the structure starts transferring the inertial force into the soil; the phenomenon is called inertial interaction. This is the result of the dynamic coupling between a structure and its supporting ground. The deformability of the soil increases the kinematic degrees of freedom of the structure. In addition, the ground can dissipate the vibration energy through the radiation damping and hysteresis damping of soils. In general, the inertial and dissipative properties of the soil-foundation system make the dynamic response of the foundation frequency-dependent. Figure 1.4 shows the inertial forces arising from the excitation of the ground.

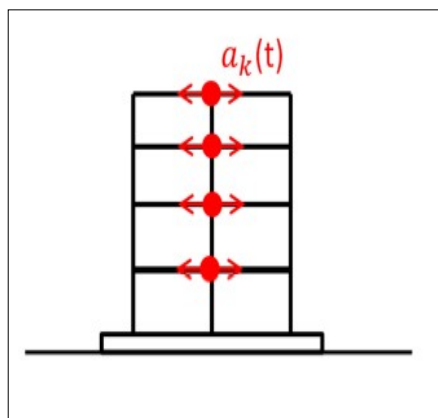


Figure 1.4. Inertial interaction (Kramer, 1996).

If the deformability and energy dissipation of a supporting soil are accounted for, the response of a structure to a given ground motion would be substantially different from that of a fixed-base structure. The magnitude of this difference will depend on the mismatch between the stiffness of the superstructure-foundation system and the stiffness of the supporting

ground. Thus, the inertial interaction would be negligible for structures founded on rock or very stiff soils because, in such cases, the structural response would be almost identical to that of a fixed-base structure. On the other hand, the interaction effect could be quite significant for structures founded on highly deformable, soft soils. The governing equation for SSI is given as

$$M \dot{u}_H + K u_H = - M_{st} (\dot{u}_b + \dot{u}_{KI}) \quad (1.3)$$

Where, M_{st} is the mass of the system assuming that the soil is massless. \dot{u}_b and \dot{u}_{KI} represents the inertial loading on the structure foundation system. This inertial loading depends on the base motion and foundation input motion, which reflects the effects of kinematic interaction.

Combination of Kinematic and Inertial Interaction

Adding the kinematic and inertial interaction equation of motion, i.e., equations 1.2 and 1.3, will give the complete equation of motion (Direct Method), i.e., equation 1.1. Though the method avoids the requirement of radiating boundary conditions, this cannot be applied to nonlinear dynamic soil-structure interaction analysis in view of the fact that superposition is only applicable to linear analysis.

1.3 Major challenges

The response of the structure under seismic excitation depends on many parameters, like the earthquake source, travel path including local site effects, soil-foundation-structure interaction, and the properties of the structure itself. Numerical modelling requires very careful attention to these parameters; a slight deviation in choosing any of the above parameters may affect the results significantly. Also, numerical modelling parameters such as finite element type, soil domain size, material models, type of interfaces, and boundary conditions play a critical role in obtaining the correct response of the structure.

Radiating boundary conditions is one of the major perturbations in the soil-structure interaction analysis since the numerical model must truncate at a finite distance without receiving the effect of the reflected waves. Major research work has been carried out in the field of absorbing boundaries for elastic wave propagation, such as a). Local Absorbing Boundary Conditions (Lysmer and Kuhlemeyer, 1969, White et al., 1977, Lindman, 1975, Engquist and Majda, 1977 and Mur, 1981), b). Absorbing Layers techniques which include Perfectly Matched Layers (Berenger, 1994), Caughey Absorbing Layer Method (Semblat et al., 2010), Absorbing Layers by Increasing Damping (Rajagopal et al., 2012), and Stiffness Reduction Method (Pettit et al., 2014), c). Boundary element method, d). Boundary element methods (Benergee et al. 1981; Beskos, 1997; Hall and Oliveto, 2003) and e). Infinite elements (Ungless, 1973; Zeinkeiwicz and Bettess, 1976; Andersion and Ungless, 1977; Bettess, 1978). A detailed literature review on these methods is presented in Chapter 2.

But the existing research studies are either not efficiently absorbing the waves on reaching the boundary or require modelling a very large domain to absorb the outgoing wave to get acceptable results. However, the soil material exhibits viscoelastic-plastic nonlinear behaviour. There exist several rheological models, material models, or damping models to

simulate viscoelastic wave propagation that can be used with the viscoelastic medium. These models require distinct absorbing boundaries, which can account for the viscosity or damping. Most of the absorbing boundary conditions are derived based on elastic or nonlinear wave propagation. Limited research has been carried out to provide absorbing boundaries for the wave propagation in the viscoelastic plastic soil medium, such as the Absorbing Layers by Increase in Damping (ALID) method, the Cauchy Absorbing Layer Method (CALM), etc.

1.4 Scope and Objectives of the study

In view of the major challenges discussed in the previous section, the main objective of this research is to develop the efficient radiating boundary conditions for the wave propagation in a viscoelastic-plastic nonlinear medium. The research work comprises the following.

1. Develop the Absorbing Boundary Conditions for wave propagation in a viscoelastic medium (VABC).
2. Develop the numerically efficient radiating boundary conditions by combining the absorbing layers and VABC (ALID+VABC)
3. Validate the newly developed boundary conditions and verify their advantages and limitations.
4. Apply the above new methods to soil-structure interaction problems and investigate the response of the structure.

1.5 Organization of the Thesis

Chapter 1 presents the introduction of soil-structure interaction, including the theoretical aspects of SSI analysis, major challenges involved in the numerical modelling of SSI analysis, and brief objectives of the current study.

In **Chapter 2**, an attempt has been made to present the state of art, literature review on different types of radiating boundary conditions available in literature along with advantages and limitations of the method

Chapter 3 presents the nonlinear finite element analysis methodology, including finite element formulations, contact interface elements, and the nonlinear material model adopted in the research work.

Chapter 4 provides the detailed formulations for newly developed absorbing boundary conditions for wave propagation in viscoelastic materials (VABC). Verification tests are carried out, and conclusions are provided.

Chapter 5 provides a methodology to combine Absorbing Layers combined with VABC (ALID+VABC). A detailed numerical analysis is carried out for the reflections when the wave impinges other than normal direction.

Chapter 6 covers the aspects of numerical modelling for a 20-story high-rise building, including modelling soil-structure interaction and the different radiating boundary condition configurations.

Chapter 7 summarizes the findings of the current study and provides conclusions along with validations and recommendations. Finally, the scope for possible future research is presented.

2. Literature Review

2.1 Introduction

One of the major challenges in the numerical analysis of the dynamic soil-structure interaction problem is modelling the boundary conditions. Modelling the wave propagation through solids requires the domain to extend to either an infinite or semi-infinite. To solve the wave propagation problems using finite element analysis (FEA), it is required that the boundary be terminated at some finite location. This truncation of the model at the finite boundary will cause the reflection of radiating waves. The reflected waves from the boundary will affect the solution and may lead to instabilities in the numerical analysis. Therefore, it is necessary to provide an artificial boundary condition that will transmit the outwardly propagating waves with minimal or negligible reflections. To address this problem, various methodologies have been developed, which can be broadly categorized as follows.

- Absorbing boundary conditions
- Absorbing layer methods
- Infinite elements
- Boundary element method etc.

In the subsequent sections, the detailed discussions are presented on these methods along with conclusions.

2.2 Absorbing boundary conditions

The viscous boundary conditions proposed by *Lysmer and Kuhlemeyer* (1969) are the first Absorbing Boundary Conditions for elastic wave propagation. These boundary conditions are extensively used in commercial software since they are very easy to implement, and their computational cost is almost negligible. The boundary conditions correspond to a situation where the boundary is supported on infinitesimal dashpots oriented normal and tangential to the boundary, as shown in Figure 2.1. The corresponding stress components in normal and tangential directions are

$$\sigma = a \rho V_p \dot{u} \quad (2.1)$$

$$\tau = b \rho V_s \dot{v} \quad (2.2)$$

Where σ and τ are the normal and shear stresses, \dot{u} and \dot{v} are the normal and tangential velocities respectively; ρ is the mass density; V_s and V_p are the velocities of S-waves and P-waves respectively; a and b are dimensionless parameters.

Figure 2.2 shows the reflected energy ratios for compressive and shear waves when they are approaching different incident angles. Also, the reflections are minimal when coefficients a and b are equal to unity. The reflections are minimal when the waves impinge in a normal direction. From Figure 2.3, it can also be observed that the reflections are increasing as the Poisson's ratio (ν) is increasing. Another drawback of these boundary conditions is that they are based on elastic wave propagation. Therefore, these boundaries must be placed at such a distance that the waves will be linearized before reaching the boundary.

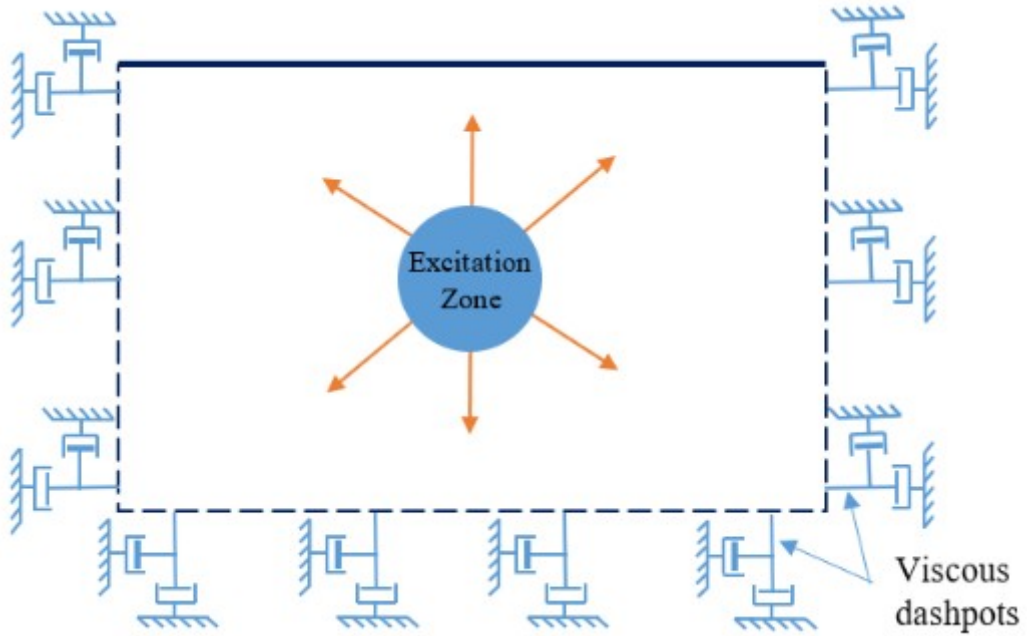


Figure 2.1. Absorbing boundary conditions

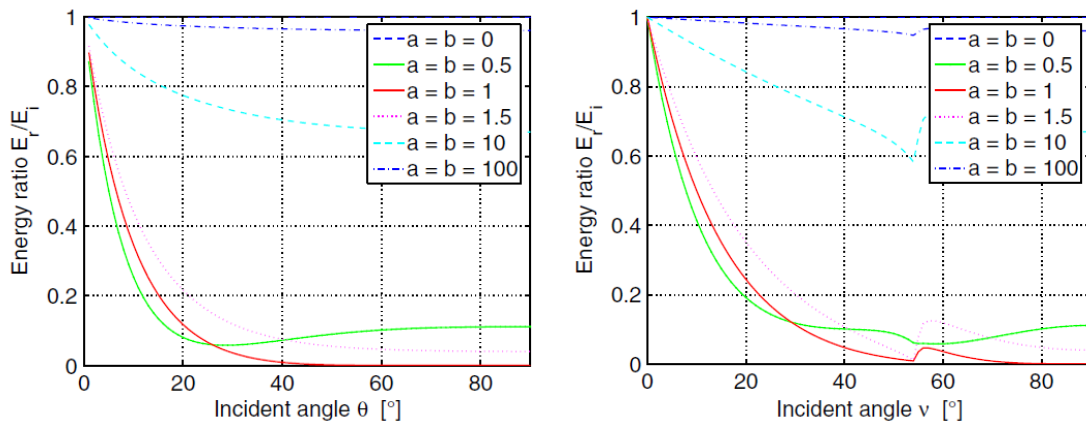


Figure 2.2. Energy ratios for incident P and S wave ($\nu=0.25$) (Georges, 2011)

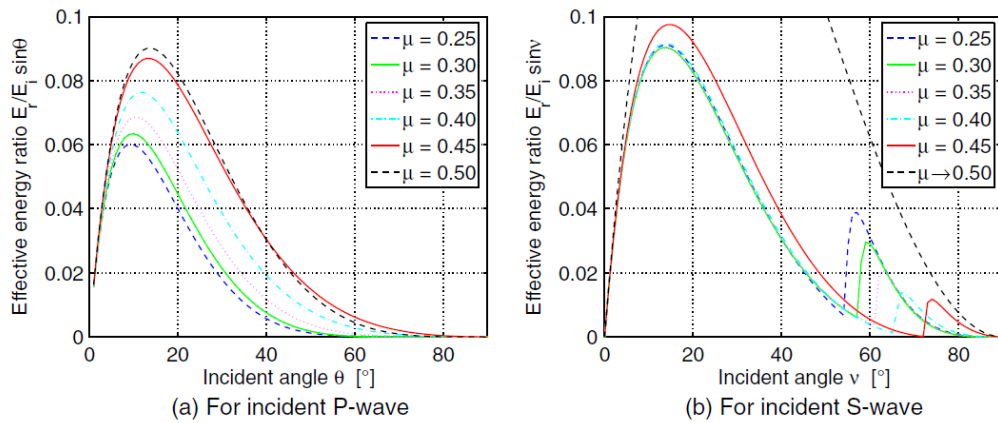


Figure 2.3. Energy ratios for various Poisson's ratios ν (Georges, 2011)

White et al. (1977) presented the unified boundary condition for anisotropic materials, a modification to the standard viscous boundary conditions, by choosing the appropriate dimensionless parameters a and b . However, Cohen (1980) and Kellezi (1998) found that for isotropic materials, the performance is slightly worse than standard boundary conditions.

Liu et al. (2006) proposed a viscous spring artificial boundary condition (VSAB) where the spring-dashpot system is modelled together to model the absorbing boundary condition. Zhicheng et al. (2016) used the modified spring constants in VSAB and compared the solution with the analytical and extended boundary conditions. It was reported that spring-dashpot provides accurate results with modified constant values for these coefficients. However, these boundary conditions are applicable to a specific type of problem where the input seismic location is well known and not suitable for absorbing radiation wave energy.

Higher-order boundary conditions have been proposed to model radiating boundary conditions by increasing the order of approximation. Lindman (1975) first proposed the higher-order boundary conditions using projection operators. Engquist and Majda (1977) and Mur (1981) proposed higher-order boundary conditions by expanding using the Taylor and Pade approximations. Saeed Izadian et al. (2021) proposed a semi-exact local absorbing boundary condition in the frequency domain. However, these procedures were developed for finite difference methods and cannot be applied directly to the finite element method.

Research is also carried out for developing the Absorbing Boundary Conditions for nonlinear wave propagation. Han and Yin (2007) proposed the boundary condition for nonlinear wave propagation, such as the Klein-Gordon equation. Han and Zhang (2008) proposed the local ABC for the Klein-Gordon nonlinear equation. Li and Wu (2011) extended the local boundary for the generalized nonlinear wave equation. The exact absorbing boundary condition has been proposed by Ting (1968) and can be applied for some special cases like plane wave propagation and cylindrical wave propagation. Like higher-order local boundary conditions, these procedures are also developed for finite difference methods.

2.3 Absorbing layer techniques

A few absorbing layers are provided around the area of study to absorb all the outwardly propagating energy. The major challenge with absorbing layer techniques is the change in damping between successive layers. If the damping change is high, then impedance mismatch is also high between successive layers, and hence there are reflections. Israeli and Orszag (1981) presented an absorbing layer technique using a sponge/damped layers to absorb outward propagating energy. Though this approach absorbs almost all outward propagating energy, it requires many elements.

Perfectly Matched Layers (PML) originally proposed by Berenger (1994), is an artificial absorbing layer technique. The basic idea of the PML is that the incident wave energy is absorbed inside the PML layers while matching impedance with non-PML layers. This property allows the PML to strongly absorb outgoing waves from the interior of a computational region without reflecting them back into the interior domain. These absorbing boundary conditions have been widely applied in recent years (Chew and Liu, 1996; Collino and Tsogka, 2001; Marcinkovich and Olsen, 2003; Komatitsch and Martin, 2007; Meza-Fajardo and Papageorgiou, 2008). However, the original equations were mainly developed

for finite difference schemes. PML has been successfully implemented in the time domain for an explicit dynamic solver by Basu (2009). Further, the PML technique has been used to create a new element type for absorbing the outgoing waves in elastodynamic problems by Chen Junwei et al., (2022). However, the resulting finite element formulations are very complex and require much computational time.

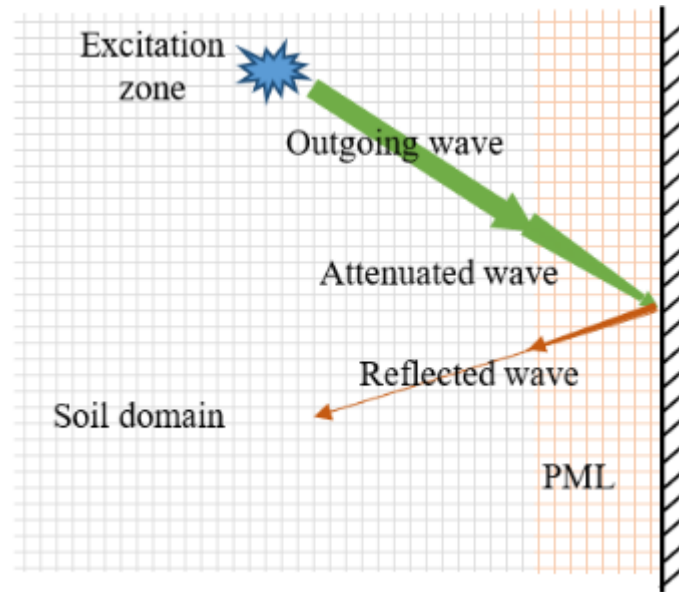


Figure 2.4. PML adjacent to a truncated domain attenuates an outgoing wave.

The Caughey Absorbing Layer Method (CALM) was proposed by Semblat et al. (2010), is a simple and reliable alternative to the Perfectly Matched Layer (PML). Like other absorbing layer methods (Israeli M. and Orszag, 1981; Rajagopal et al., 2012; Pettit et al., 2014; Rodrigues (2015)), the CALM consists of defining an absorbing layer at the boundaries of the elastic medium under consideration. This absorbing layer is modelled with the same elastic properties as the interior medium, but the Rayleigh damping is added to attenuate all waves that leave the interior domain. This method also requires many absorbing layers to absorb the outward propagating waves and hence requires much computational time Pettit et al., (2014).

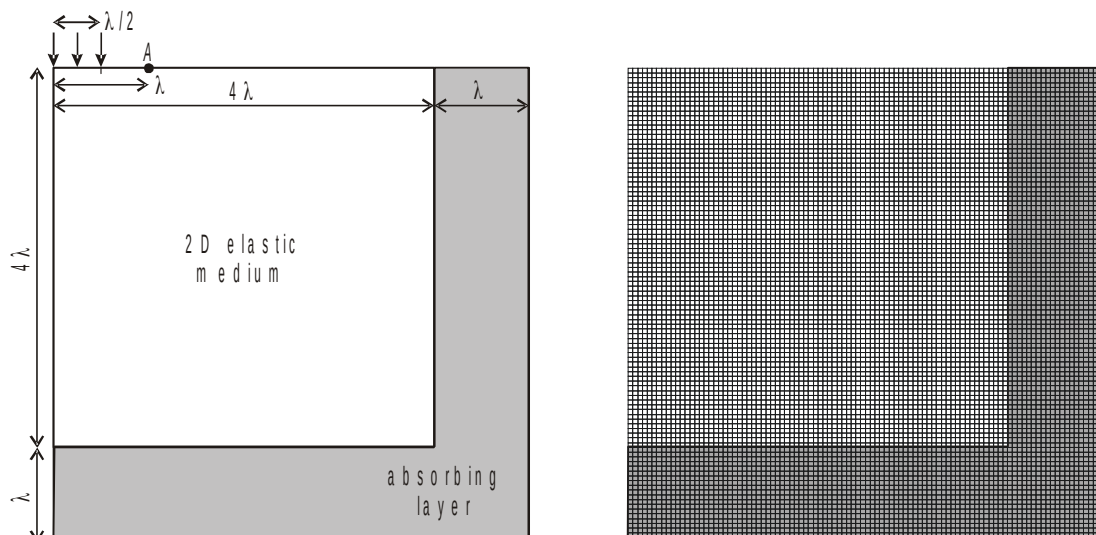


Figure 2.5. 2D plane strain model with absorbing later boundary (Semblat et al., 2010)

The Absorbing Layers by Increasing Damping (ALID) method is like the CALM absorbing layers method. Rajagopal et al. (2012) applied the mass proportional damping part of Rayleigh damping to the absorbing region. As a result, this method does not affect the stable time step required for the explicit finite element analysis scheme. The stiffness reduction method (SRM) was proposed by Pettit et al. (2014), in which Young's modulus is reduced exponentially, in addition to increasing mass proportional damping. Rajagopal et al. and Pettit et al. also provided the optimum values for the design of ALID and SRM to efficiently model the absorbing region.

Israeli and Orszag (1981) also presented a technique to combine the absorbing layers and local absorbing boundary conditions, in which the absorbing layer properties are modified such that the damping coefficient is zero at the boundary. The damping properties are gradually increased from zero at the beginning to a maximum in the middle of the layers and then reduced to zero at the end of the absorbing region. Therefore, absorbing layer properties are matched with the absorbing boundary conditions. However, this method needs twice the number of layers compared with that required for ALID.

2.4 Boundary element methods

The basic idea of the boundary element method (Benergee et al., 1981; Beskos, 1997; Hall and Oliveto, 2003) consists in solving an equation on the boundary of the domain only, while the radiation conditions are considered analytically using an integral equation. It also reduces the dimension of the problem to a surface in 3D and to a curve in 2D, thus decreasing the size of the problem to solve. However, the final problem involves full matrix which is generally non-symmetrical. There are also singularities in the integrals that need special attention for the numerical integrations. It is mainly limited to linear problems and to homogeneous domains; otherwise, one must introduce special and complex techniques to deal with nonlinear or non-homogeneous situations.

2.5 Infinite element methods

The idea of infinite elements (Bettess, 1992; Astley, 2000) is to provide an element that is stretched to infinity so that the effects of the semi-infinite region are included in the finite element modelling. These elements provide an effective way of modelling the near field with finite elements and the far-field with infinite elements. In literature, the infinite elements are broadly classified into three groups.

- Decay function
- Mapped
- Wave envelope
- Elastodynamic infinite elements

The decay function elements use the shape functions of regular finite elements multiplied with the decay function (Ungless, 1973; Zeinkeiwicz and Bettess, 1976; Andersion and Ungless, 1977; Bettess, 1978). Mapped infinite elements are developed by mapping the infinite domain onto the finite elements using mapping functions (Zeinkeiwicz et al., 1985). The accuracy of these elements depends on the order of the elements. Lower order elements are suffering from accuracy, and the higher-order elements are suffering from instabilities and ill-conditioning. The wave envelope and elastodynamic infinite element are treated as a special combination of the decay function and mapped infinite elements (Astley, 2000; Yun et al., 2007). However, these methods require complex transformations of mass and stiffness matrices from the frequency domain to the time domain.

2.6 Conclusions

Radiating boundary conditions is one of the major challenges in the soil-structure interaction analysis since the numerical model must truncate at a finite distance without receiving the effect of the reflected waves. To address the radiating boundary conditions problem, researchers have developed various kinds of formulations over a few decades, such as a). Local Absorbing Boundary Conditions, b). Absorbing Layers techniques, which include Perfectly Matched Layers, Caughey Absorbing Layer Method, Absorbing Layers by Increasing Damping, and Stiffness Reduction Method, c). Boundary element method, and d). Infinite elements.

Most of the existing methods are based on elastic wave propagation. But the soil material exhibits viscoelastic-plastic nonlinear behaviour. There exist several rheological models, material models, or damping models to simulate viscoelastic wave propagation that can be used with the viscoelastic medium. These models require distinct absorbing boundaries, which can account for the viscosity and damping. Limited research has been carried out to provide absorbing boundaries for the wave propagation in the viscoelastic plastic soil medium, such as the Absorbing Layers by Increase in Damping (ALID) method, the Cauchy Absorbing Layer Method (CALM), etc. However, these methods require modelling a very large domain to absorb the outgoing wave to get acceptable results. In view of these limitations in the available research, the proposed research presented the objectives of the study in Section 1.4.

3. Finite element displacement-based formulation

3.1 Introduction

The finite element method is one of the well-known numerical solution techniques for solving the boundary value problem. Finite element modelling for nonlinear dynamic soil-structure interaction analysis involves modelling the superstructure, foundation, soil medium, and the interactions between the structure and the substructure.

In this chapter, the dynamic equilibrium equation and finite element discretization of the spatial domain are presented. This chapter also provides the detailed procedure adopted in this research for the implementation of nonlinear analysis, nonlinear material modelling, and contact interfaces.

3.2 Principle of virtual work

The principle of virtual work states that, if the body is subjected to any arbitrary virtual displacements, \bar{u} in its state of equilibrium, then the external virtual work is equal to the internal virtual work (Bathe, 2010). Let's assume that a body is in equilibrium under the action of external body forces f^b and surface traction forces f^s at an internal stress state σ . If the body is subjected to a virtual displacement \bar{u} , then the strain energy of the body can be written as

$$\int_V \bar{\epsilon}^T \sigma dV = \int_V \bar{u}^T f^b dV + \int_T \bar{u}^T f^s dS \quad (3.1)$$

where $\bar{\epsilon}$ is the virtual strains associated with \bar{u} virtual displacements. If the body is in a dynamic state, then the total strain energy must include the inertial and viscous forces of the body in motion. Using the d'Alembert principle, total virtual strain energy can be updated by including the body's inertial forces $\int_V \bar{u}^T \rho \dot{u} dV$. Similarly, body viscous forces $\int_V \bar{u}^T c \dot{u} dV$ can be included along with inertial forces.

$$\int_V \bar{\epsilon}^T \sigma dV = \int_V \bar{u}^T f^b dV - \int_V \bar{u}^T (\rho \dot{u} + c \dot{u}) dV + \int_S \bar{u}^T f^s dS \quad (3.2)$$

where, \dot{u} and \ddot{u} are velocities and accelerations respectively. ρ and c are mass density and damping coefficients respectively. V and S represents total volume and surface area of body.

3.3 Finite element discretization

In the finite element analysis, the body is discretized into finite elements interconnected at the nodal points. The geometry and the field variables from the nodes are interpolated inside the element using Isoparametric formulations. Let's assume that H_i as the shape function of an

element corresponds to the connected node i . Then the Shape function matrix H^m , for an element m can be written as

$$H^m = \begin{bmatrix} H_1 & 0 & 0 & H_2 & 0 & 0 & \dots & H_N & 0 & 0 \\ 0 & H_1 & 0 & 0 & H_2 & 0 & \dots & 0 & H_N & 0 \\ 0 & 0 & H_1 & 0 & 0 & H_2 & \dots & 0 & 0 & H_N \end{bmatrix} \quad (3.3)$$

Where, N is the number of nodes of the element m .

Let's assume that \hat{u}_i , \hat{v}_i and \hat{w}_i are the nodal displacements of an element in element local axis corresponding to the connected node i . Then element displacement vector \hat{u} in can be written as

$$\hat{u}^T = \{\hat{u}_1 \hat{v}_1 \hat{w}_1 \hat{u}_2 \hat{v}_2 \hat{w}_2 \dots \hat{u}_N \hat{v}_N \hat{w}_N\} \quad (3.4)$$

The displacements u^m at any point within the element can be computed using element shape functions defined in equation 3.3.

$$u^m = H^m \hat{u}; \quad (3.5)$$

The strain-displacement matrix B of an element can be defined as

$$B = \begin{bmatrix} \frac{dH_1}{dx} & 0 & 0 & \frac{dH_2}{dx} & 0 & 0 & \dots & \frac{dH_N}{dx} & 0 & 0 \\ 0 & \frac{dH_1}{dy} & 0 & 0 & \frac{dH_2}{dy} & 0 & \dots & 0 & \frac{dH_N}{dy} & 0 \\ 0 & 0 & \frac{dH_1}{dz} & 0 & 0 & \frac{dH_2}{dz} & \dots & 0 & 0 & \frac{dH_N}{dz} \\ \frac{dH_1}{dy} & \frac{dH_1}{dx} & 0 & \frac{dH_2}{dy} & \frac{dH_2}{dx} & 0 & \dots & \frac{dH_N}{dy} & \frac{dH_N}{dx} & 0 \\ 0 & \frac{dH_1}{dz} & \frac{dH_1}{dy} & 0 & \frac{dH_2}{dz} & \frac{dH_2}{dy} & \dots & 0 & \frac{dH_N}{dz} & \frac{dH_N}{dy} \\ \frac{dH_1}{dz} & 0 & \frac{dH_1}{dx} & \frac{dH_2}{dz} & 0 & \frac{dH_2}{dx} & \dots & \frac{dH_N}{dz} & 0 & \frac{dH_N}{dx} \end{bmatrix} \quad (3.6)$$

If \bar{u} is the virtual nodal displacements, then the elemental virtual displacements, and virtual strains can be calculated using

$$\bar{u}^m = H^m \bar{u}; \quad \bar{\epsilon}^m = B \bar{u}; \quad (3.7)$$

Equation 3.2 provides the total strain energy of a continuum body. When this body is discretized using the M number of finite elements, the equation can be written as

$$\sum_{m=1}^M \int_{\nu} \bar{\epsilon}^{mT} \sigma dv = \sum_{m=1}^M \int_{\nu} \bar{u}^{mT} f^b dv - \sum_{m=1}^M \int_{\nu} \bar{u}^{mT} (\rho \dot{u}^m + c \dot{u}^m) dv + \sum_{m=1}^M \int_s \bar{u}^{mT} f^s ds \quad (3.8)$$

where V and ν represents the total volume of the body and volume of one finite element. Substituting 3.7 in 3.8 and rearranging the final equation yields

$$M \dot{u} + C \dot{u} + f^i = f^e \quad (3.9)$$

The equation 3.9 is also called a dynamic equilibrium equation. M , C , f^i and f^e are the mass matrix, damping matrix, internal force vector, and external force vector respectively. These are defined as

$$M = \sum_{m=1}^M \int_{\nu} H^T \rho H dv \quad (3.10a)$$

$$C = \sum_{m=1}^M \int_{\nu} H^T c N dv \quad (3.10b)$$

$$f^i = \sum_{m=1}^M \int_{\nu} B^T \sigma dv \quad (3.10c)$$

$$f^e = \sum_{m=1}^M \int_{\nu} H^T f^b dv + \sum_{m=1}^M \int_s H^T f^s ds \quad (3.10d)$$

Internal force vector f^i computation is trivial for linear materials as the stress-strain relation is linear and can be expressed as

$$\sigma = D * \epsilon \quad (3.11)$$

where, ϵ is strain vector, D material stress-strain matrix and σ is the stress vector. Substituting equations 3.11 and 3.7 in equation 3.10c and rearranging yields

$$f^i = Ku \quad (3.12)$$

where, K stiffness matrix that can be defined as

$$K = \sum_{m=1}^M \int_{\nu} B^T D B dv \quad (3.13)$$

Therefore, for linear material, the dynamic equilibrium equation can be written as

$$M \dot{u} + C \dot{u} + Ku = f^e \quad (3.14)$$

Computation of stiffness matrix and mass matrix for the elements used in this research are presented in Appendix A.

3.4 Solution for the nonlinear dynamic equilibrium equations

The dynamic equilibrium equation presented in equation 3.9 is the second-order differential equation. Numerous techniques are available to solve this equation over space and time. Apart from the nonlinear dynamic analysis, most of the practical problems required nonlinear static analysis. In fact, for problems involving dynamic soil-structure interaction, the initial stress state of the model needs to be solved using static analysis. In the sub-sections, both static analysis and dynamic analysis techniques are presented.

3.4.1 Nonlinear static analysis

The nonlinear static equilibrium equation is the subset of the dynamic equilibrium equation. The equilibrium equation can be obtained by dropping the dynamic term in the equation 3.9.

$$\sum_{m=1}^M \int_{\nu} B^T \sigma dv = f^e \quad (3.15)$$

In the above equation, strain-displacement matrix B , the stress vector σ and the nodal displacement vector u are all unknowns and interdependent on each other. Therefore, the solution to the above equation requires nonlinear iterative solvers. There are several schemes available, such as

- Initial Stiffness Method
- Newton Raphson Method (NRM)
- Modified Newton Raphson Method (MNRM) etc.,

Each of these methods has its advantages and disadvantages. In NRM, stiffness is updated at every iteration. Updating stiffness is numerically expensive. This method requires the development of an algorithm to estimate the tangent material modulus for each nonlinear material used in the model. In MNRM, stiffness is updated once per incremental load; therefore, it reduces the cost of frequent updating of the stiffness. But this method still requires the estimation of tangent material modulus requires additional implementation cost. In this research, the Initial Stiffness Method has been used to solve the nonlinear static problem.

Initial stiffness method

In this method, the global stiffness matrix is assembled only at the beginning of the analysis. The same stiffness matrix is used for all the load steps. The main disadvantage of this method is that it requires many iterations to converge on the solution. There are techniques like the “accelerated initial stiffness method” to accelerate the convergence. This research is limited to the original initial stiffness method but updated for contact interfaces.

In this method, first the global stiffness matrix K is assembled as defined in equation 3.13 at the beginning of the analysis. At each load step, the equations are solved for the displacement using equation 3.12. Let u_l be the displacements at load step l and f_l^e be the external load. The internal forces and displacements at $l+1$ are computed as follows.

First, the displacements at $l+1$ is assumed as same at l i.e.

$$u_{l+1} = u_l \quad (3.16)$$

The internal forces at $t + \Delta t$ is computed using

$$f_{l+1}^i = \sum_{m=1}^M \int_{\nu} B^T \sigma_{l+1} dv \quad (3.17)$$

The correction for the displacements is computed using

$$\Delta u = K^{-1} (f_{\square}^e - f_{l+1}^i) \quad (3.18)$$

Check the contact interface condition for internal forces corresponding to the displacements $u_{l+1} + \Delta u$. If the interface condition is changed between free, fixed, and slip condition then update the global stiffness matrix K to include the status of contacts and update the corrections for displacements using equation 3.18. Otherwise, displacements are updated using

$$u_{l+1} = u_{l+1} + \Delta u \quad (3.19)$$

The steps from equations 3.16 to 3.19 are repeated until the convergence criteria are met. Fig. 3.1 shows the pictorial representation of this method.

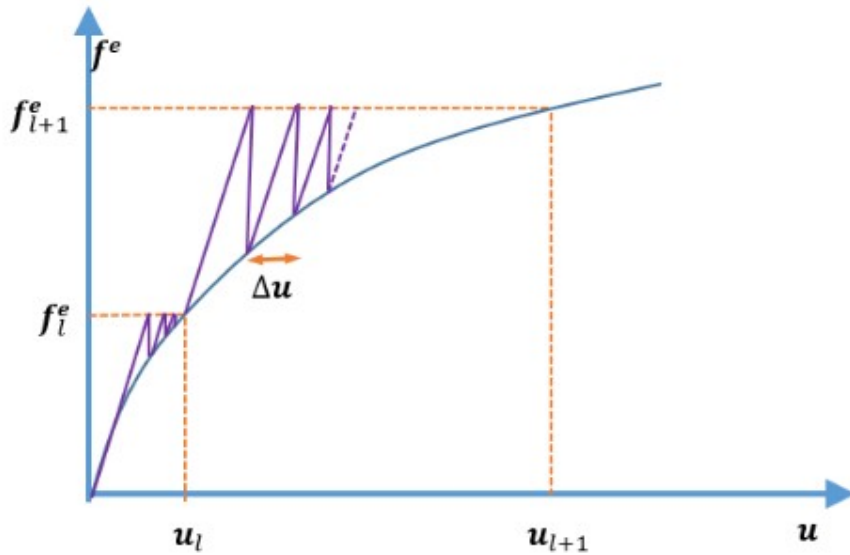


Figure 3.1. Iterative procedure for Initial Stiffness Method

3.4.2 Nonlinear dynamic analysis

There are many numerical techniques available in the literature for direct integration of the dynamic equilibrium equation. They can be broadly classified into Implicit schemes and Explicit methods. In this thesis, the central difference explicit scheme is adopted. The major disadvantage of the method is the requirement of a small-time step. However, for the seismic evaluation of soil-structure interaction problems, a small time step is very much required. The

major advantage of the explicit solvers is that they don't need the inversion of the stiffness matrix.

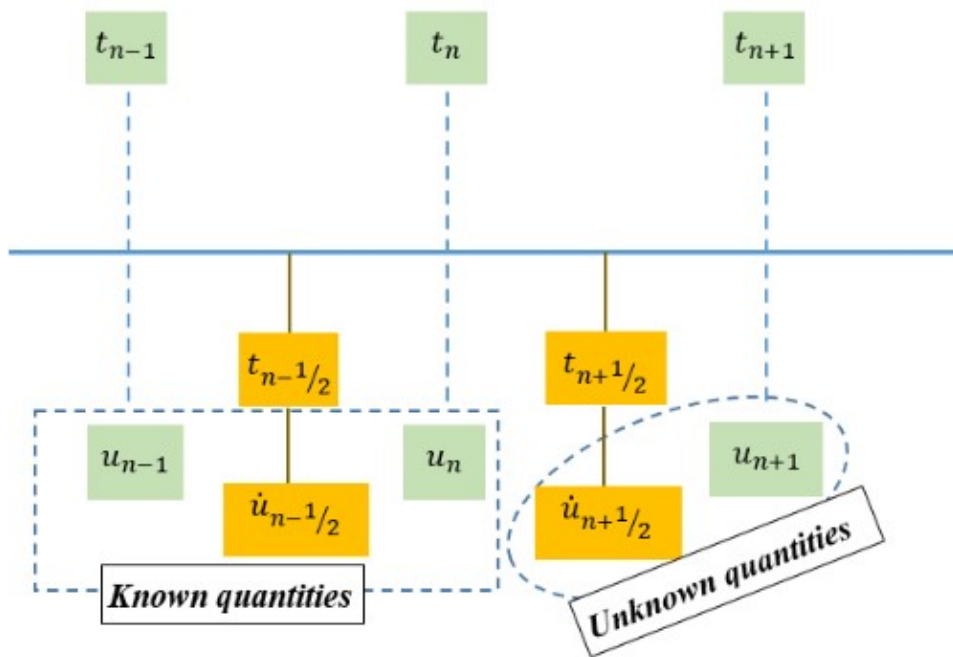


Figure 3.2. Time marching of central difference explicit solver

In this scheme, displacements u and accelerations \ddot{u} are computed at every time step, and velocities are computed in the middle of the time step as shown in the Fig. 3.2. The scheme assumes that the displacement u and accelerations \ddot{u} at current time step n and the velocities \dot{u} at the middle of current and previous time $n - \frac{1}{2}$ are known quantities.

The velocities at $n + \frac{1}{2}$ are computed using

$$\dot{u}_{n+\frac{1}{2}} = \dot{u}_{n-\frac{1}{2}} + \ddot{u}_n \Delta t_n \quad (3.20)$$

The displacements at $n+1$ are computed using

$$u_{n+1} = u_n + \dot{u}_n \Delta t_n \quad (3.21)$$

The acceleration at $n+1$ are computed using dynamic equilibrium equation

$$\ddot{u}_{n+1} = M^{-1} \left(f_{n+1}^e - f_{n+1}^i - C \dot{u}_{n+\frac{1}{2}} \right) \quad (3.22)$$

where, f_{n+1}^i is the internal force vector estimated using the equation 3.17 and f_{n+1}^e are the external force vector.

3.5 Contact interfaces

3.5.1 Introduction:

Contact interface modelling is an obligatory requirement in the nonlinear soil-structure interaction analysis. The interfaces appear between the foundation and the soil and between different soil layers or soil layer and underneath bedrock. The interfaces between the structural foundation and soil played a major role in transferring wave propagation energy through both kinematic interaction and inertial interaction. Research presented various techniques to model the interfaces, such as Zero Thickness element (Goodman et al., 1968), Thin-layer interface element (Desai et al., 1984) and Contact-Friction elements (Katona, 1983; Carpenter et al., 1991) etc. There are various methodologies available for the node-to-node contact-friction elements:

- Lagrange Multiplier Method,
- Augmented Lagrange Multiplier Method
- Penalty Method etc.

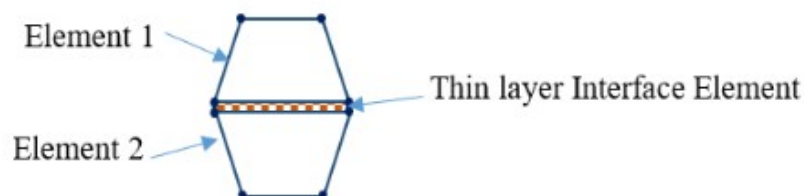


Figure 3.3. Thin interface elements (Desai, 1984)

Katona (1983) developed the node-to-node contact friction (Fig. 3.4) element by using Lagrange Multipliers in conjunction with the principle of virtual work, which makes it easy to implement in standard finite element formulations for implicit or static analysis. This method gives accurate results for contact penetration problems. However, this methodology creates additional degrees of freedom for the contacts. If the number of contact nodes is higher, the resulting stiffness matrix will bloat and may not be suitable for large contact analysis problems.

Carpenter et al. (1991) introduced a modification of the Lagrange Multiplier method called the Forward Increment Lagrange Multiplier method (FILM), which is compatible with explicit time integration and does not affect the stability of integration. The idea of the method is to refer to the kinematic contact constraints one time-step ahead of the equations of motion and the Lagrange multipliers.

Oden and Pires (1984), Hallquist et al. (1985), and Simo et al. (1985) have studied the penalty method to solve the contact friction problems. In the penalty-based approach, contacts are replaced with nonlinear springs. This method does not create an additional degree of freedom. The results from the contact analysis may have slight penetration, but in most cases, this is acceptable. In this research, Penalty-based node-to-node contact friction elements were employed since they are simple and easy to implement.

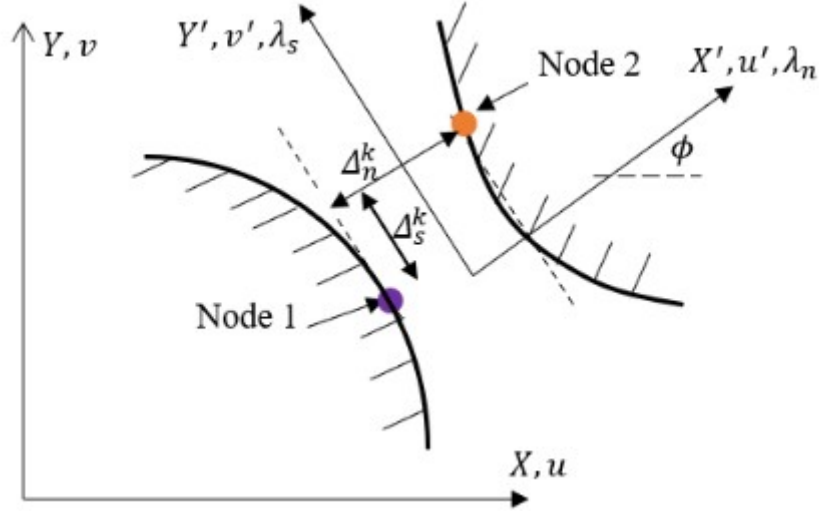


Figure 3.4. Node-to-node interface element (Katona, 1983)

3.5.2 Penalty based node to node contact element

In a penalty-based node-to-node friction contact element, three-direction translational springs comprised of one axial and two lateral directions are provided. In the axial direction, the spring works as compression-only elements and in translational directions, they work as elastic-plastic elements. The plastic limit is based on the Coulomb friction law. Force-displacement equilibrium is defined as

$$f_x = k_x u_x; \quad k_x = 0; \text{ if } u_x > 0 \text{ i.e., in tension} \quad (3.23a)$$

$$f_y = k_y u_y; \quad |f_y| \leq \mu |f_x| \quad (3.23b)$$

$$f_z = k_z u_z; \quad |f_z| \leq \mu |f_x| \quad (3.23c)$$

$$f_y = \frac{(f_y * \mu |f_x|)}{\sqrt{f_y^2 + f_z^2}}; f_z = \frac{(f_z * \mu |f_x|)}{\sqrt{f_y^2 + f_z^2}} \quad \text{if } \sqrt{f_y^2 + f_z^2} > \mu |f_x| \quad (3.24d)$$

where, f_x , f_y and f_z are the internal resistance forces in spring element local directions x , y and z respectively. μ is coulomb friction. k_x , k_y and k_z are the stiffness in spring element local axis directions x , y and z respectively.

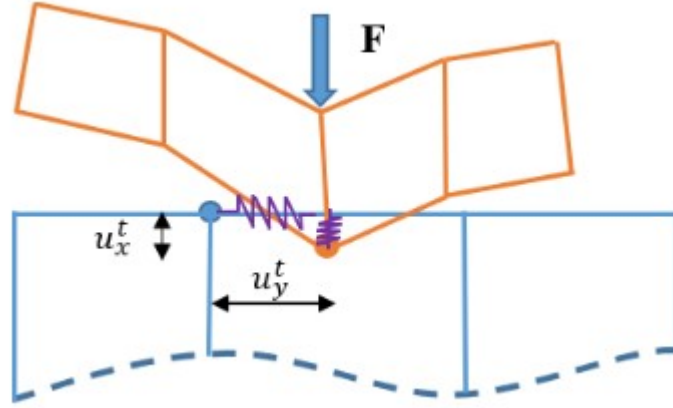


Figure 3.5. Contact friction idealization using springs in the Penalty Method

The idealization of the contact springs is shown in Fig. 3.5. These springs come with a penalty due to penetration and the violation of the contact condition. Therefore, this method adds additional internal virtual work. The total internal virtual work for including n contact springs becomes

$$W \int_{\Omega} = \sum_{m=1}^M \int_{\Omega} \bar{\epsilon}^{mT} \sigma \, dv + \sum_1^n (k_x u_x \bar{u}_x) + (f_y \bar{u}_y) + (f_z \bar{u}_z) \quad (3.24)$$

The penalty due to friction elements largely depends on the choice of stiffness. The greater the stiffness, the smaller the penetrations, and therefore, the lesser the penalty. However, very high stiffness causes instabilities and convergence issues. It is customary to provide 10 times the stiffness of the softer material around the contacts.

3.5.3 Algorithm for nonlinear static analysis

In this section, a detailed algorithm is presented for the nonlinear static analysis discussed in Section 3.4.1, including contact interfaces and incremental loading conditions. Geometric nonlinear effects can be included using co-rotational formulations.

STEP 1: Assume all the interface conditions are fixed. Set the loading iteration counter to zero, $l = 0$ and the iteration counter to zero $k = 0$. Compute the global stiffness matrix K . Initialize the maximum number of iterations k_{max} , number of load steps l_n and initialize the displacements corresponding to the initial displacements.

$$\begin{aligned} k &= 0; l = 0; \\ u_l^k &= u_0; \\ \text{Compute } K \end{aligned}$$

STEP 2: Compute the K^{-1} and set up the external load vector $f_{l=0}^e$. Compute internal resistance force vector $f_{l=0}^i$

Compute K^{-1}
 Compute $f_{l=0}^e; f_{l=0}^i$

STEP 3: Compute the Residual force

$$\Delta f = f_{l=0}^e - f_{l=0}^i$$

STEP 4: Compute the incremental displacements

$$\Delta u = K^{-1} * \Delta f$$

STEP 5: Update the displacements, element local axis, and strain-displacement matrix. Compute the internal forces from elements as well as from contact elements

$$u_l^k = u_l^{k-1} + \Delta u$$

Update strain-displacement matrix, B using updated nodal positions.

Compute strains using $\varepsilon = B u_l^k$

Compute stresses σ for strains ε using material model

$$\text{Compute } f_l^i = \sum_{m=1}^M \int_{\square} B^T \sigma dv$$

STEP 6: Update the internal forces to include the contact forces

Compute contact forces f_x, f_y and f_z as defined in the section 3.5.2

Compute $f_l^i = f_l^i + \sum_1^n (f_x, f_y, f_z)$ for n number of contact spring elements.

STEP 7: Check for convergence at every degree of freedom of the system.

$$\text{If } \frac{(f_l^e - f_l^i)}{f_l^e} \leq \text{TOL}; \text{ Go to STEP 9.}$$

STEP 8: If the convergence criteria are not met, check for a maximum number of iterations, update the iteration counter and compute the imbalance force.

If $k > k_{max}$:

Not converged in a maximum number of iterations. **Solver TERMINATE**

Else:

$$\Delta f = f_l^e - f_l^i$$

$$k = k + 1$$

Go to STEP 4.

STEP 9: If the number of load steps is not completed, update the external force vector and initialize the displacement for the next load step. Also, update the load step counter and set the iterator counter to zero.

If $l < l_n - 1$:

$u_{l+1}^0 = u_l^k$
 Compute f_{l+1}^e
 Compute $\Delta f = f_l^e - f_{l+1}^i$
 $l = l + 1$; $k = 0$;
Go to STEP 4.

Else:

SOLUTION COMPLETE.

3.5.4 Algorithm for nonlinear dynamic analysis

In this section, a detailed algorithm for the nonlinear dynamic analysis, including contact interfaces, is presented. In central difference explicit schemes, the time step is an important criterion. The mass proportional part of Rayleigh damping is only used in this research to avoid the complications due to instabilities in time step computations when stiffness proportional damping is applied. Geometric nonlinear effects can be included using co-rotational formulations.

STEP 1: Initialize all the interface conditions, i.e., fixed, friction, or free, based on initial conditions. Set the time equal to zero i.e., $t=0$. Compute the time step Δt from all elements including contact interfaces.

$t=0$;
 Initialize interface conditions i.e., Fix or Friction or Free
 Compute Δt

STEP 2: Generate mass m and damping c vectors for all degrees of freedom. Initialise the velocities $\dot{u}_{t-\frac{\Delta t}{2}}$, displacements u_t at the beginning of the analysis i.e., at $t=0$.

Initialize velocities $\dot{u}_{t-\frac{\Delta t}{2}}$, displacements u_t ; $t=0$
 Compute Mass and Damping vectors; m and c

STEP 3: Estimate the external force vector and internal force vectors at time t

Estimate f_t^e
 Compute $f_t^i = \sum_{m=1}^M \int_{\Omega} B^T \sigma dv$
 Compute contact forces f_x, f_y and f_z as defined in the section 3.5.2
 Compute $f_t^i = f_t^i + \sum_1^n (f_x, f_y, f_z)$

STEP 4: compute accelerations at time t , velocities at $t - \frac{\Delta t}{2}$ and displacement at $t - \Delta t$ for all individual degrees of freedom

$$\dot{u}_t = \frac{\left(f_t^e - f_t^i - c \dot{u}_{t-\frac{\Delta t}{2}} \right)}{m}$$

$$\dot{u}_{t+\frac{\Delta t}{2}} = \dot{u}_{t-\frac{\Delta t}{2}} + \dot{u}_t \Delta t$$

$$u_{t+\Delta t} = u_t + \dot{u}_{t+\frac{\Delta t}{2}} \Delta t$$

STEP 5: Update the time and check for maximum time

$$t = t + \Delta t$$

If $t > t_{max}$

Else

SOLUTION COMPLETE

Go to STEP 3

3.6 Material Modelling

In this section, the stress integration algorithm is presented for the linear elastic material model as well as for the elastic-plastic materials. Structural elements such as rafts, piles, columns, and beams can be modelled using linear materials unless any of these elements fall into the range of nonlinearity during the analysis. However, soil modelling for wave propagation depends on several factors, such as the initial stress state, stress path, elastoplastic behaviour, creep, relaxation, strain rate, and hardening or softening behaviour. The complexity in the behaviour of soils has led to the development of several models based on the classical theories of elasticity, plasticity, viscoelasticity, viscoelastic plastic, and critical state theories.

3.6.1 Linear elastic material:

The stiffness behaviour of linear elastic materials is defined by two parameters: Young's modulus (E) and Poisson's ratio (ν). The stress-strain relationship can be defined as

$$\sigma = D \varepsilon \quad (3.25)$$

Where,

σ , is stress vector

ε , is strain vector

D , is symmetric (6x6) material matrix for three dimensional analysis is given by

$$D = \frac{E}{(1+\nu)(1-2\nu)} \begin{bmatrix} 1-\nu & \nu & \nu & 0 & 0 & 0 \\ \nu & 1-\nu & \nu & 0 & 0 & 0 \\ \nu & \nu & 1-\nu & 0 & 0 & 0 \\ 0 & 0 & 0 & 0.5-\nu & 0 & 0 \\ 0 & 0 & 0 & 0 & 0.5-\nu & 0 \\ 0 & 0 & 0 & 0 & 0 & 0.5-\nu \end{bmatrix} \quad (3.26)$$

Similarly, the material matrix D for Plane Strain problems can defined as

$$D = \frac{E}{(1+\nu)(1-2\nu)} \begin{bmatrix} 1-\nu & \nu & 0 \\ \nu & 1-\nu & 0 \\ 0 & 0 & 0.5-\nu \end{bmatrix}$$

for Plane Stress problems the material matrix D can defined as

$$D = \frac{E}{(1-\nu^2)} \begin{bmatrix} 1 & \nu & 0 \\ \nu & 1 & 0 \\ 0 & 0 & \frac{1-\nu}{2} \end{bmatrix}$$

3.6.2 Elastic-Plastic Materials

Pressure-dependent material models are the most common type of material used for soil modelling, such as Drucker-Prager, Mohr-Coulomb material models, etc. Drucker-Prager material model is the generalization of the Mohr-Coulomb material model with a smooth cone as shown in Fig. 3.6. The most common types of generalization are either outer edge coincident or inner edge coincident.

Drucker-Prager Yield Criterion:

The yield criteria of the Drucker-Prager can be defined using cohesion c and friction angle θ .

$$F_{(\sigma)} = \eta p_{(\sigma)} + \sqrt{J_{2D}} - kc; F_{(\sigma)} \leq 0 \quad (3.27)$$

where,

$p_{(\sigma)}$ is the hydrostatic pressure,

$J_{2D} = \frac{1}{2} s:s$, s is the second invariant of the deviatoric stress.

$s = \sigma - p_{(\sigma)}I$, I is identity matrix.

η and k are material constants and can be defined for outer and inner edge approximations using equations 3.27a and 3.27b respectively.

$$\eta = \frac{6 \sin \theta}{\sqrt{3}(3 - \sin \theta)}; k = \frac{6 \cos \theta}{\sqrt{3}(3 - \sin \theta)} \quad (3.28a)$$

$$\eta = \frac{6 \sin \theta}{\sqrt{3}(3 + \sin \theta)}; k = \frac{6 \cos \theta}{\sqrt{3}(3 + \sin \theta)} \quad (3.28b)$$

Plastic flow direction is an important property of the soils. The corresponding flow potential can be defined as.

$$G_{(\sigma)} = \dot{\eta} p_{(\sigma)} + \sqrt{J_{2D}}; \quad (3.29)$$

Where, $\dot{\eta}$ is calculated using the same expression as η defined in equation 3.28 using dilatancy angle φ instead of friction angle θ .

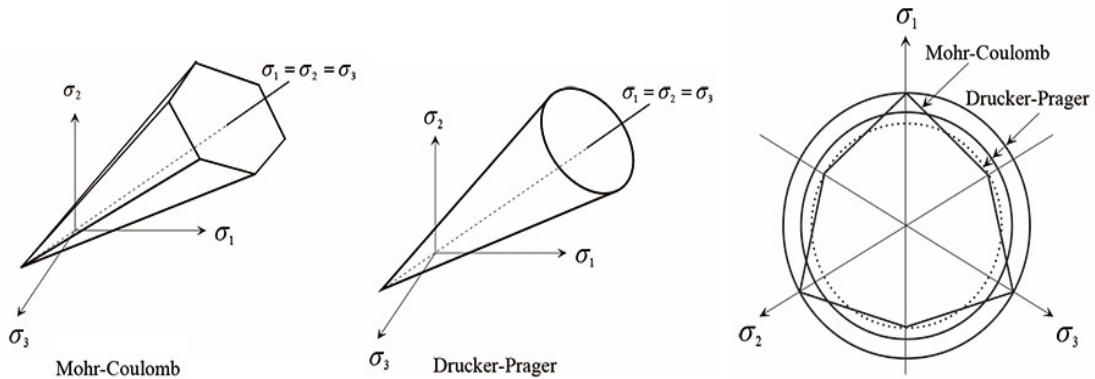


Figure 3.6. Mohr-Coulomb and Drucker-Prager failure surfaces

Material Hardening:

Apart from the yield criteria and plastic flow rule, material hardening type is also a major impacting factor for a stress-strain relationship when the material is undergoing plasticity. There are two types of hardening, namely:

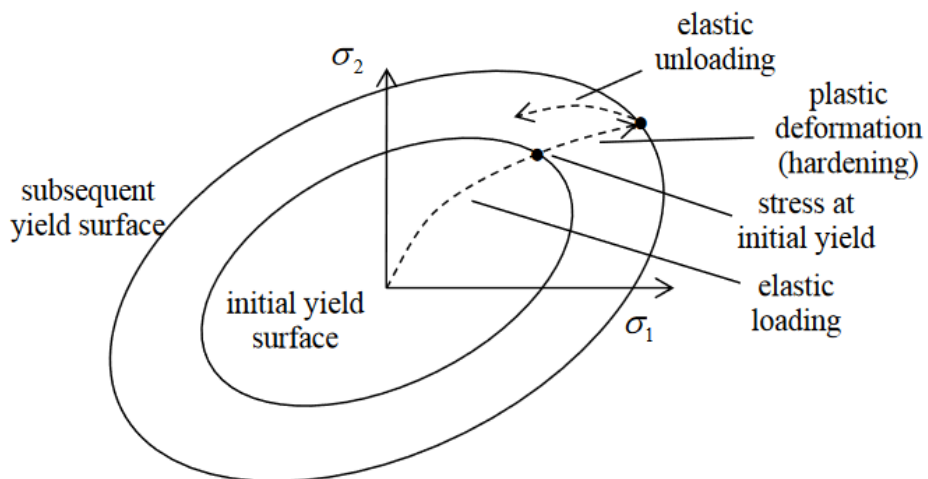


Figure 3.7. Isotropic hardening

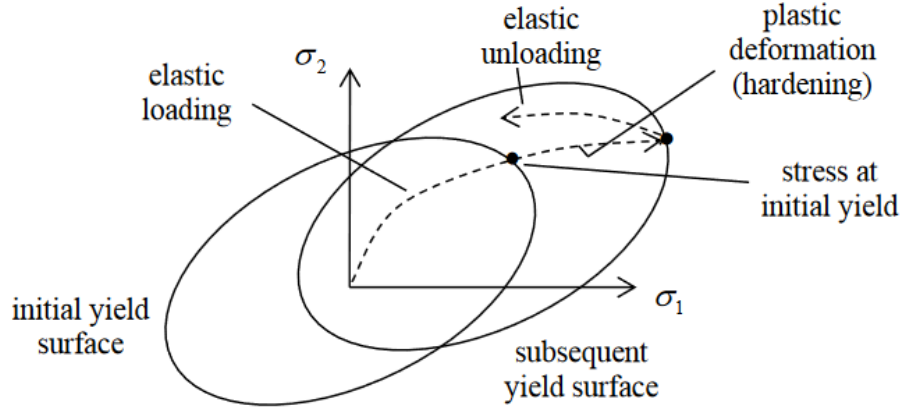


Figure 3.8. Kinematic hardening

1. Isotropic Hardening
2. Kinematic Hardening

In Isotropic hardening, the yield surface is expanding uniformly because of strain hardening, but the centre of the yield surface remains unchanged. However, this is contrary to the Bauschinger effect, wherein if the material is hardened on the tension side, it gets softened on the compression side. In Kinematic hardening, the yield surface size and shape remain unchanged, but the centre of the yield surface is changed, as shown in Fig. 3.8. The Bauschinger effect can be included using Kinematic hardening. Almost all soil materials exhibit both Isotropic and Kinematic hardening when subjected to dynamic loading. However, these parameters for both hardenings require extensive study of the material under dynamic loading conditions. The complexity also increases with the type of material model, such as Mohr-Coulomb, Drucker-Prager, etc. Therefore, in most practical cases, the isotropic hardening material model is used, and hence the study is limited to isotropic hardening. When hardening is included in the yield criteria, the yield criteria can be defined as

$$F_{(\sigma)} = \eta p_{(\sigma)} + \sqrt{J_{2D}} - k c_{(\epsilon_p)}; F_{(\sigma)} \leq 0 \quad (3.30)$$

Where, $c_{(\epsilon_p)}$ is cohesion as a function of plastic strain.

Stress update algorithm:

The stress update algorithm for Drucker-Prager material is used for both static and dynamic nonlinear analysis. The stress update algorithm can be divided into two steps: the predictor step and the corrector step (return mapping). In predictor steps, the incremental strains $d\epsilon$ are assumed to be elastic and in corrector step, plastic strains $d\epsilon^p$ are estimated. Radial return mapping is used in this research to obtain a closed form solution and thereby avoid numerical convergence issues.

Predictor Step:

Assuming the incremental strain as elastic, incremental stresses are computed using

$$d\sigma = D * d\epsilon \quad (3.31)$$

Estimate the total trial stresses as

$$\sigma_{tr} = \sigma_n + d\sigma \quad (3.32)$$

where, σ_n is the correct stress vector from previous step n and σ_{tr} is trial stresses in current step $n+1$.

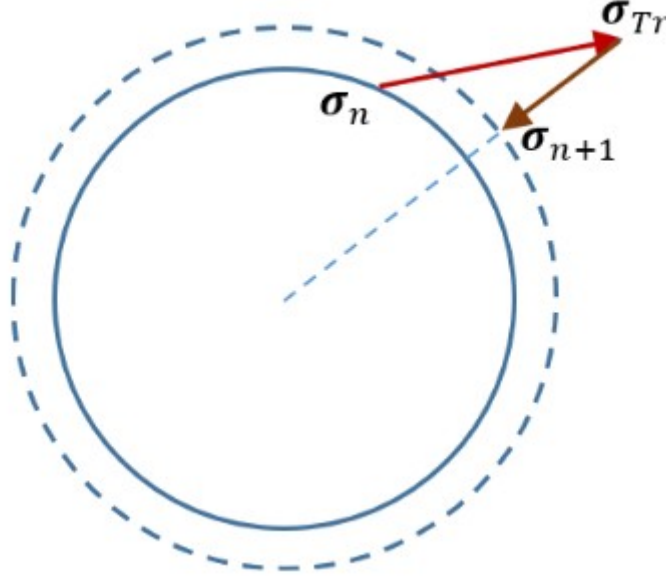


Figure 3.9. Schematic representation of Radial return mapping

Corrector Step:

The correct stress at $n+1$ is

$$\sigma_{n+1} = \sigma_{tr} - D * d\varepsilon^p \quad (3.33)$$

The plastic flow rule starts with splitting the incremental plastic strain into two components viz., magnitude $d\lambda$ and direction of plastic flow $N_{n+1} = \frac{dG_{|\sigma|}}{d\sigma}$.

$$d\varepsilon^p = d\lambda \frac{dG_{|\sigma|}}{d\sigma} = d\lambda N_{n+1} \quad (3.34)$$

Substituting equation 3.28 equation 3.33

$$d\varepsilon^p = d\lambda \left[\frac{1}{2\sqrt{J_{2D}}} s_{n+1} + \frac{\dot{\eta}}{3} I \right] \quad (3.35)$$

Substituting equation 3.34 into equation 3.32 and by splitting the D into volumetric and deviatoric parts

$$\sigma_{n+1} = \sigma_{tr} - d\lambda \left[\frac{2G}{2\sqrt{J_{2D}}} s_{n+1} + \frac{K\dot{\eta}}{3} I \right] \quad (3.36)$$

where K and G are the bulk modulus and shear modulus respectively.

In equation 3.35 the ratio of $\frac{s_{n+1}}{\sqrt{J_{2D,n+1}}}$ can be replaced with $\frac{s_{tr}}{\sqrt{J_{2D,tr}}}$ using radial return approximation

$$\sigma_{n+1} = \sigma_{tr} - d \lambda \left[\frac{2G}{2\sqrt{J_{2D,tr}}} s_{tr} + \frac{K \dot{\eta}}{3} I \right] \quad (3.37)$$

Splitting the above equation into hydrostatic and deviatoric parts

$$s_{n+1} = s_{tr} - d \lambda \left[\frac{G}{\sqrt{J_{2D,tr}}} s_{tr} \right] \quad (3.38a)$$

$$p_{n+1} = p_{tr} - d \lambda K \dot{\eta} \quad (3.38b)$$

Substituting equation 3.37 into equation 3.29 and assuming linear hardening in cohesion. Let, H be the hardening modulus corresponding to the plastic strain $d \lambda$.

$$F = \eta (p_{tr} - d \lambda K \dot{\eta}) + \sqrt{J_{2D,tr}} - d \lambda G - k [c(\varepsilon_p + H d \lambda)] = 0 \quad (3.39)$$

Rearranging the above terms yields and replacing

$$d \lambda (G + \eta K \dot{\eta} + k H d \lambda) = \eta p_{tr} + \sqrt{J_{2D,tr}} + k c(\varepsilon_p) = F_{tr} \quad (3.40)$$

$$d \lambda = \frac{F_{tr}}{(G + \eta K \dot{\eta} + k H d \lambda)} \quad (3.41)$$

Equation 3.40 represents the closed-form solution for estimating the incremental plastic strain.

3.6.3 Viscoelastic Materials:

The effect of time on the loading process is a salient feature of soils, especially clayey soils. Further, the models discussed above do not consider the time dependency. In general, there are two types of time-dependent behaviour observed in clayey soils. These are a) the interaction of free pore water and the soil skeleton, i.e., consolidation of soils with low permeability, and b) the inherent viscous characteristics of the soil skeleton. Oka (1999) discussed the constitutive modelling of time-dependent behaviour due to the viscous nature of materials, i.e., creep, relaxation, rate sensitivity, and secondary compression, as a part of the viscoelastic theory.

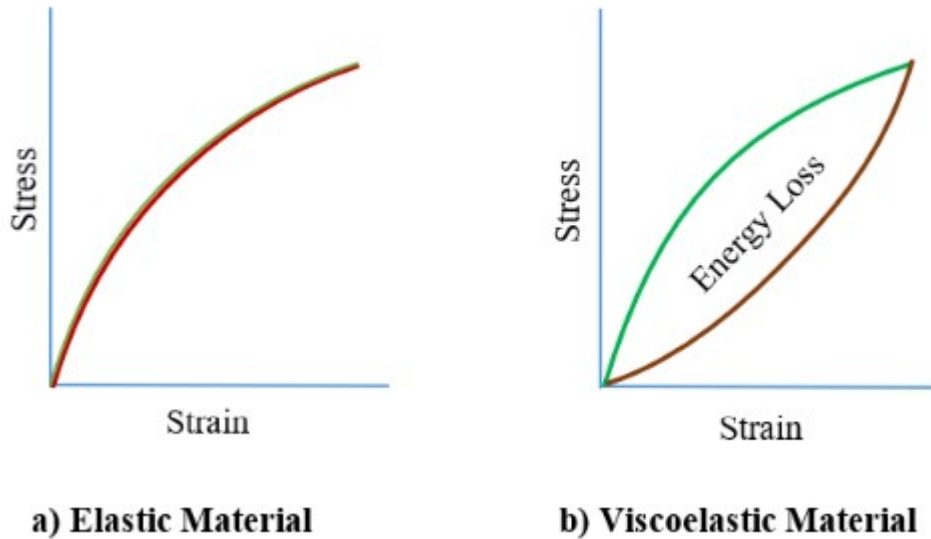


Figure 3.10. Hysteresis of stress-strain curve for Elastic and Viscoelastic deformations

Viscoelasticity consists of an elastic component and a viscous component, where viscosity is a strain rate dependent on time. Generally, it has characteristics like hysteresis, stress relaxation, and creep. In these models, hysteresis has been observed in the stress-strain curve, with the area of the loop being equal to the energy lost during the loading cycle, as shown in Fig. 3.9. The most popular method of modelling the time-dependent models are the viscoelastic models, such as Maxwell elements, Kelvin elements, standard linear equations, etc., wherein viscous dash-pots and springs are connected in sequence as shown in Fig. 3.10.

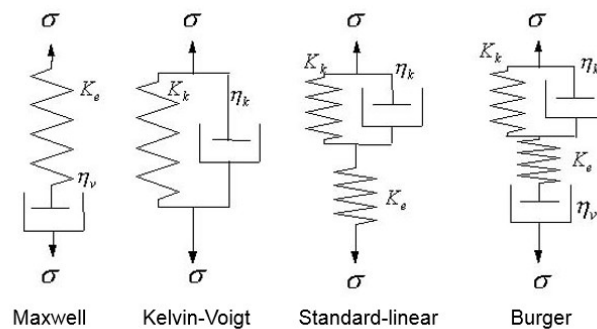


Figure 3.11. Mechanical models of viscoelastic materials

Though various material models are available to model the soil, it is very important to consider time-rate behaviours such as creep, relaxation, and damping for dynamic SSI problems. From the above discussions, it can be observed that the time-dependent behaviour is considered either directly or indirectly by including damping along with material models to simulate the nonlinear soil behaviour subjected to dynamic loading conditions.

3.7. Summary

The chapter discussed the details of displacement-based finite element formulations for the dynamic equilibrium equations of the spatial domain. The detailed step-by-step procedure for the implementation of implicit static and explicit dynamic nonlinear analysis is explained. This chapter also provided the details for the implementation of linear, elastic-plastic, and visco-elastic material models and contact interface modelling. In the next chapter, the detailed formulations for newly developed absorbing boundary conditions for wave propagation in viscoelastic materials (VABC) will be discussed.

4. Absorbing Boundary Conditions for wave propagation in Viscoelastic materials (VBAC)

4.1. Introduction

The effects of soil-structure interaction (SSI) on the behaviour of civil engineering structures have been studied for decades. To solve the wave propagation problems using finite element analysis (FEA), the model must be terminated at some finite location. This truncation of the model at the finite boundary will cause the reflection of radiating elastic waves. The reflected waves from the boundary will affect the solution and may lead to instabilities in the numerical analysis. Therefore, it is necessary to provide an artificial boundary condition that will transmit the outwardly propagating waves with minimal or negligible reflections. To address this problem, various kinds of analytical formulations have been developed, but they have their own limitations in avoiding reflections.

It is a well-known fact that almost all physical domains like soils exhibit viscoelastic-plastic behaviour when the waves travel through these domains. Absorbing Boundary Conditions (ABC) are derived based on elastic wave propagation and produce reflections when applied to viscoelastic-plastic material even when the wave impinges in a normal direction to the boundary. Nonlocal absorbing boundary conditions such as Perfectly Matched Layers (PML), the Caughey Absorbing Layer Method (CALM), Absorbing Layers by Increase in Damping (ALID), etc., can be applied for wave propagation problems with nonlinear materials. Although these methods effectively absorb the outwardly propagating wave energy, the number of degrees of freedom increases tremendously for 3D wave propagation problems (Petit et al., 2014).

To provide efficient boundary conditions for viscoelastic plastic materials, two different new absorbing boundary conditions are developed for viscoelastic materials (VABC) and nonlinear materials (NLABC). Finally, a method is proposed to combine boundary conditions for viscoelastic materials (VABC) with Artificial Layers by Increase in Damping (ALID) to provide efficient boundary conditions for viscoelastic plastic materials.

4.2. Theory and Formulation of the method

The Absorbing Boundary Conditions correspond to a situation where the boundary is supported on infinitesimal dashpots oriented normal and tangential to the boundary. The corresponding stress components are given by

$$\sigma = a \rho V_p \dot{u} \tag{4.1}$$

$$\tau = b \rho V_s \dot{v} \tag{4.2}$$

Where σ and τ are the normal and shear stresses, \dot{u} and \dot{v} are the normal and tangential velocities respectively; ρ is the mass density; V_s and V_p are the velocities of S-waves and P-waves respectively; a and b are dimensionless parameters.

The equation of motion of the system under dynamic equilibrium for viscoelastic material is defined as

$$M\dot{u} + C\dot{u} + Ku = f^e \quad (4.3)$$

Where M , C , and K are the global mass, damping and stiffness matrices respectively. \ddot{u} , \dot{u} , u and f^e are the acceleration, velocity, displacement, and external force vectors respectively. Damping matrix can be defined using Rayleigh damping coefficients as

$$C = \alpha M + \beta K \quad (4.4)$$

Where α and β are mass and stiffness proportional damping coefficients. The equation of motion defined in equation 4.3 has a harmonic solution. When the damping part of equation 4.3 is excluded, the displacements, velocities, and accelerations for each eigen frequency can be expressed as

$$\begin{aligned} u_{(x,t)} &= \varphi e^{i(kx - \omega t)} \\ \dot{u}_{(x,t)} &= -i\omega \varphi e^{i(kx - \omega t)} \\ \ddot{u}_{(x,t)} &= -\omega^2 \varphi e^{i(kx - \omega t)} \end{aligned} \quad (4.5)$$

where φ is amplitude, ω is angular frequency, x is a displacement vector $\{x, y, \text{ and } z \text{ directions}\}$, and k is wave number i.e., $k = \frac{\omega}{V_p}$. From equations 4.3, 4.4, and 4.5, the equation of motion including Rayleigh damping can be written in the frequency domain as

$$\dot{M}\dot{u} + \dot{K}u = f^e \quad (4.6)$$

where, $\dot{M} = M \left(1 - \frac{\alpha}{i\omega}\right)$ and $\dot{K} = K(1 - i\omega\beta)$ are complex mass and stiffness matrices respectively.

For linear materials, mass and elastic stiffness terms are proportional to the density and Young's modulus, respectively. Therefore, the complex mass and the complex Young's modulus can be calculated using

$$\begin{aligned} \dot{\rho} &= \rho \left(1 - \frac{\alpha}{i\omega}\right) \\ \dot{E} &= E(1 - i\omega\beta) \end{aligned} \quad (4.7)$$

Replacing Young's modulus and density in equation 4.1 with complex Young's modulus and complex density respectively

$$\sigma = a \rho V_p \sqrt{\left(1 - \frac{\alpha}{i\omega}\right)(1 - i\omega\beta)} \dot{u} \quad (4.8)$$

Expanding square root terms using Taylor series and ignoring higher-order terms in the above equation

$$\sigma = a \rho V_p \left(1 - \frac{\alpha}{2i\omega} - \frac{i\omega\beta}{2} + \frac{\alpha\beta}{2} \right) \dot{u} \quad (4.9)$$

Back substituting equation 4.5 into the equation 4.9 yields

$$\sigma = a \rho V_p [0.5\beta \dot{u} + (1 + 0.5\alpha\beta)\dot{u} + 0.5\alpha u] \quad (4.10)$$

Similarly, equation 4.2 can be modified by replacing Young's modulus and density with the complex Young's modulus and complex density and by following the steps from equation 4.8 to equation 4.10.

$$\tau = b \rho V_s [0.5\beta \dot{v} + (1 + 0.5\alpha\beta)\dot{v} + 0.5\alpha v] \quad (4.11)$$

Equations 4.10 and 4.11 are the improved absorbing boundary conditions, which include the effect of the Rayleigh damping in the equation of motion. From equations 4.8 and 4.9, it can be observed that stiffness proportional damping terms are not converging at higher frequencies, these equations are mainly limited to mass proportional damping cases.

If mass proportional only damping is applied, then the equations 4.10 and 4.11 can be rewritten as

$$\sigma = a \rho V_p \dot{u} + 0.5 a \rho V_p \alpha u \quad (4.12)$$

$$\tau = b \rho V_s \dot{v} + 0.5 b \rho V_s \alpha v \quad (4.13)$$

Absorbing forces in normal and tangential directions at the VABC can be calculated using $F_n = \sigma A$ and $F_t = \tau A$, where A is the associated area corresponding to respective dashpots. It can be observed from the equations 4.12 and 4.13 that the absorbing forces at the boundary include a dashpot with coefficient $a \rho V_p A$ and a spring with coefficient $0.5 a \rho V_p \alpha A$.

The damping and spring coefficients are calculated only once at the beginning of the solver and do not need to be updated during the analysis. Also, most of the existing Finite Element software packages allow defining dampers and springs. Therefore, these boundary conditions can be easily modelled without any additional implementation, and the additional computation cost is negligible.

4.3. Effect of higher-order terms

The equations for VABC have been obtained by using Taylor expansion of square root terms in equation 4.8 as given below.

$$\sqrt{\left(1 - \frac{\alpha}{i\omega}\right)(1 - i\omega\beta)} \dot{u} = i \left\{ 1 - \frac{1}{2} \left(\frac{\alpha}{i\omega} + i\omega\beta - \alpha\beta \right) - \frac{1}{8} \left(\frac{\alpha}{i\omega} + i\omega\beta - \alpha\beta \right)^2 - \dots \right\} \dot{u} \quad (4.14)$$

The above equation is in the frequency domain, and hence it requires an inverse Fourier transform to convert into the time domain. Using equation 4.5, the first-order terms of frequency content can be converted to the time domain as

$$\frac{\alpha}{i\omega} \dot{u} = -\alpha u$$

$$i\omega\beta \dot{u} = -\beta \dot{u} \quad (4.15)$$

Similarly, second-order terms can be converted into the time domain using

$$\left(\frac{\alpha}{i\omega}\right)^2 \dot{u} = \alpha^2 \int_0^t u$$

$$(i\omega\beta)^2 \dot{u} = \beta \ddot{u} \quad (4.16)$$

From equation 4.15, it can be noted that the first-order terms of VABC are displacements and accelerations. As the displacements and accelerations are readily available with the FE solver at any time step during the analysis, the first-order terms of VABC can be easily incorporated.

Equation 4.16 shows that the second-order terms of VABC require "time integration of displacements" and "rate of change of accelerations." In general, these values are not considered in the FE solver to carry out a dynamic analysis. Also, the calculation of these values requires additional implementation costs, computational costs, and storage for memory variables. Therefore, this study is limited to first-order terms. Several validation tests have been conducted to verify the performance of the VABC.

4.4. Convergence analysis

The square root term in the equation 4.8 is in the form of $\sqrt{1-x}$. Therefore, the convergence of the equation is first studied, then the effect of damping parameters and frequency content are studied in the next section. The function is invalid when the x value is greater than or equal to 1.

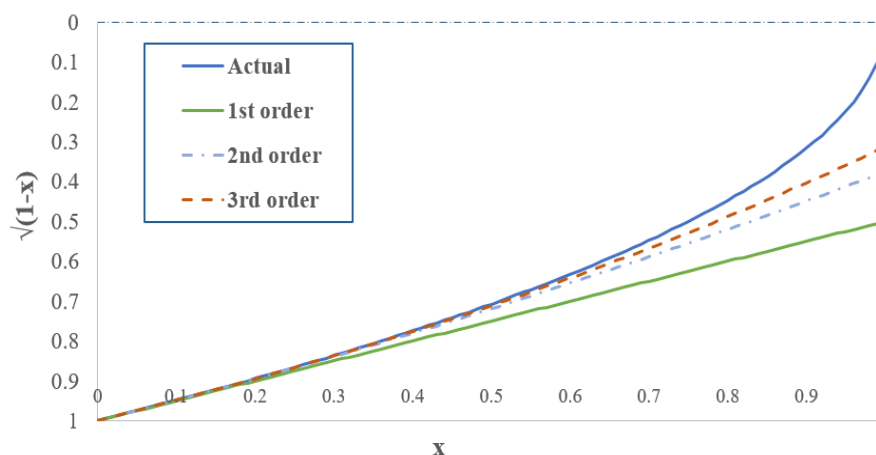


Figure 4.1. The convergence of Taylor Series for $\sqrt{1-x}$ for the different degree of polynomials

Fig. 4.1 shows the convergence of the Taylor series for the different degrees of polynomials. It is noted that, for lower values of x , i.e., less than 0.2, the Taylor series is converging with a first-order polynomial with an accuracy of 99.3%. Therefore, higher-order terms can be safely ignored when the value of x is less than 0.2.

4.4.1. Effect of Rayleigh damping parameters and frequency content on the convergence

In general, Rayleigh damping coefficients (α and β) are determined by selecting two predominant design frequencies. When the damping coefficients are applied to the domain, the modes outside the selected frequencies are heavily damped, and the modes between these frequencies are lightly damped.

The square root term in equation 4.8 is in the form of $\sqrt{1-x}$.

$$\sqrt{1-x} = \sqrt{1 - \left(\frac{\alpha}{i\omega} + i\omega\beta - \alpha\beta \right)} \quad (4.17)$$

As discussed in the previous section, if the value of x is small, the Taylor series for $\sqrt{1-x}$ will converge with fewer terms. From equation 4.17, it can be noted that the term $i\omega\beta$ increases with an increase in frequency. This term may create convergence issues for higher frequencies. Hence, mass-proportional damping is only considered in the subsequent section and equation 4.17 and can be rewritten as.

$$\sqrt{1-x} = \sqrt{1 - \frac{\alpha}{i\omega}} \quad (4.18)$$

As the above equation is dropping out the stiffness proportional damping terms, the equation 4.18 does not include the stiffness proportional damping. Therefore, if stiffness proportional damping is only applied to the domain, there is no performance improvement over the standard absorbing boundary conditions.

The mass proportional damping coefficient α is calculated for the design frequency ω_d and damping ratio ζ as

$$\alpha = 2\omega_d\zeta \quad (4.19)$$

Substituting equation 4.19 in equation 4.18 gives

$$\sqrt{1-x} = \sqrt{1 - \frac{2\omega_d\zeta}{i\omega}} \quad (4.20)$$

From the above equation, it can be noted that the convergence of the equation is dependent on the ratio $\frac{2\omega_d\zeta}{i\omega}$. This concludes that, if the equation is converging for the lowest frequency, then it automatically converges for all higher modes. If the design frequency is

chosen as a fundamental frequency, then convergence only depends on the damping ratio ζ . In the later sections, verification has been carried out for different damping ratios.

4.4.2 Rheological interpretation of mass proportional damping

Considering the relationship between viscosity and frequency for Rayleigh damping, it is possible to build an equivalent rheological model for mass proportional damping. The equation of motion can be written for mass proportional damping by dropping stiffness proportional damping from equation 4.6

$$\dot{M}\dot{u} + Ku = f_e \quad (4.21)$$

Considering the wave velocities and complex density, complex dynamic modulus can be calculated as

$$\dot{E} = \frac{1}{\left(\frac{1}{E} - \frac{\alpha}{i\omega}\right)} \quad (4.22)$$

Which is equivalent to Maxwell material model dynamic modulus

$$\dot{E} = \frac{1}{\left(\frac{1}{E} - \frac{1}{\omega}\right)} \quad (4.23)$$

$$n = \frac{1}{\alpha} \quad (4.24)$$

where n is the coefficient of viscosity. The quality factor is defined as

$$Q^{-1} = 2\zeta = \frac{\alpha}{\omega} \quad (4.25)$$

4.5 Numerical examples

The objective of this section is to demonstrate the efficiency of proposed boundary conditions through various numerical examples, and the results are validated with standard solutions. Numerical examples include the 1D and 2D wave propagation problems, which are carried out using finite element analysis with explicit integration.

4.5.1. 1D p-wave propagation

A one-dimensional wave propagation model is developed, as shown in Fig. 4.2, to verify the efficiency of the proposed solution. The viscoelastic bar is idealized using a two-node element of length 1.0 m, and the cross-sectional area is taken as 0.1 m². The length of the element has arrived such that the displacements are consistent with smaller-sized elements. The material is viscoelastic; Young's modulus and density are taken as 45x10⁵ N/m² and



1800 kg/m³, respectively. The primary wave velocity, $V_p = \sqrt{E/\rho}$ is estimated as 50 m/sec under the elastic loading. Viscous effects are added by including mass proportional damping.

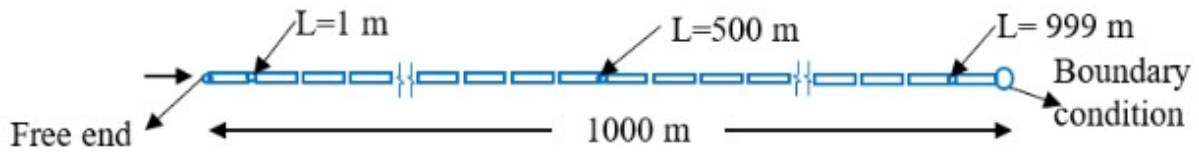


Figure 4.2. Configuration for one-dimensional wave propagation model

The load is applied at the free end of the member, and boundary conditions are applied at the right end of the member. The total length of the member is 1000 m, and the wave travel time from the free end to the right boundary is approximately 20 seconds under viscoelastic wave propagation. The analysis has been carried out for 100 seconds to study the effects of reflection of the wave and to study the displacements in the member for longer durations. The load applied at the free end includes force and displacement separately, and the results are verified for both cases.

Table 4.1. Mass proportional damping for different damping ratios

Damping ratios (%)	5	10	15	20
Damping coefficient (α)	0.00785	0.0157	0.0235	0.0314

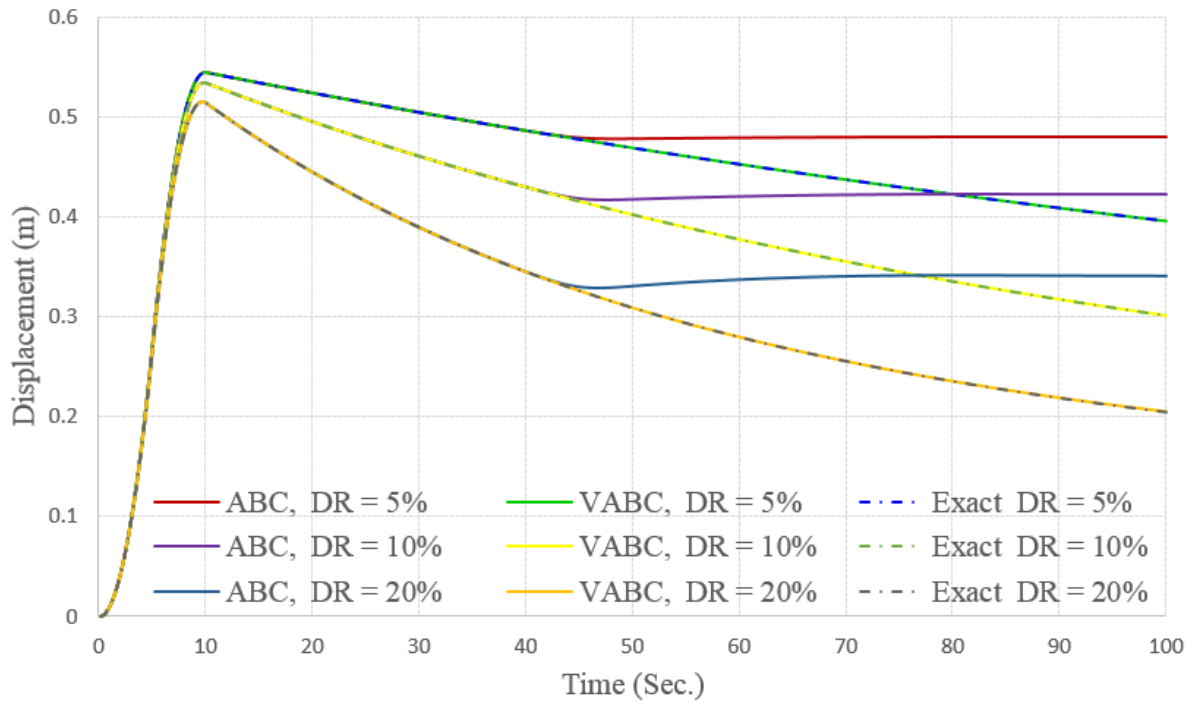
Eigenvalue analysis has been carried out to estimate the natural frequencies of the model using a structural analysis software, Oasys GSA. The lowest frequency of the model is estimated 0.0125 Hz and the corresponding mass participation factor is 81.05. Table 4.1 shows the mass proportional damping coefficients for different damping ratios.

1D p-wave propagation with load control

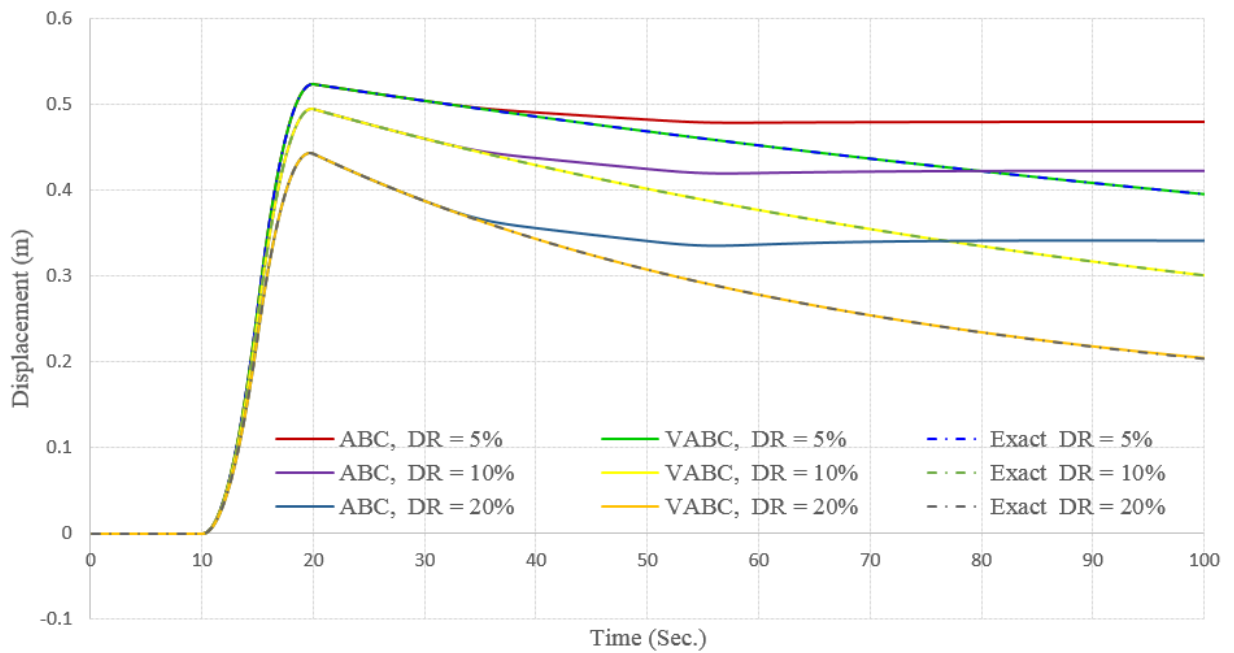
The efficiency of VABC is studied for different damping ratios of 5%, 10%, and 20% by applying a concentrated force at the left end

$$F(t) = \begin{cases} 200t & \text{for } 0 \leq t \leq 5 \\ 1000 - 200(t - 5) & \text{for } 5 \leq t < 10 \\ 0 & \text{for } t \geq 10 \end{cases} \quad (4.26)$$

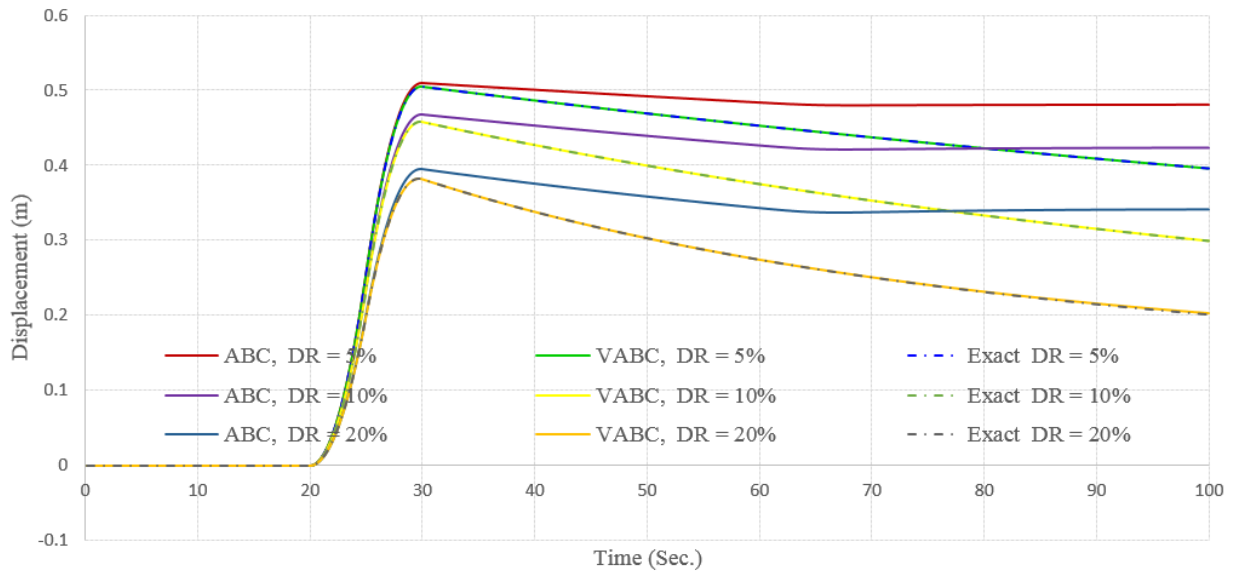
Where, $F(t)$ is the force in Newton and t is the time in seconds.



a. Displacements at L=10m



b. Displacements at L=500m



c. Displacements at L=990m

Figure 4.3. Displacements at different locations for 5%, 10% and 20% damping ratios

The results are compared with the extended mesh model, where the length of the member is 5000 m. The length of the extended model is selected such that during the analysis time, the wave will not reflect from the boundary.

Fig. 4.3 shows the calculated displacements along the length of the member for different damping ratios. From the figure, it is studied that the displacements with ABC do not converge with the exact solution, while the displacements with VABC converge with the exact solution. It is also observed that there are permanent deformations along the length of the member with ABC of around 0.48 m, 0.42 m, and 0.34 m for damping ratios of 5%, 10%, and 20%, respectively. This shows that the VABC accounts for the damping in the material beyond the boundary into consideration.

To compare the degree of accuracy, reflections of ABC and VABC are calculated with reference to the exact solution, i.e., with an extended mesh model as shown in Fig. 4.4. Table 4.2 summarizes the maximum reflections produced for absorbing boundary (ABC) and Viscous Absorbing boundary VABC. It is observed that reflections are almost negligible in the case of VABC.

Table 4.2. Maximum reflections for different damping ratios

Damping Ratio	Reflection forces for ABC (N)	Reflection forces for VABC (N)
5%	8.93	0.16

10%	16.19	0.14
20%	26.84	1.20

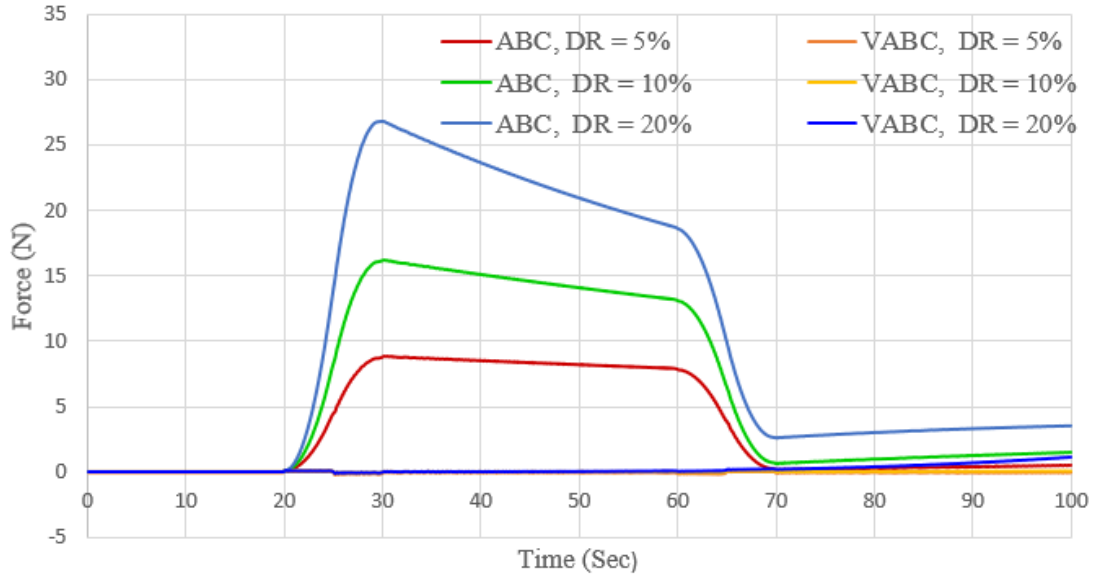


Figure 4.4. Reflections near the boundary ($L=990m$)

1D p-wave propagation with displacement control

In this section, the performance of the VABC is analysed under displacement control at the left end by applying axial displacement with the Gaussian source is given by

$$U(0, t) = e^{-\pi^2 f_p^2 (t - t_s)^2} \quad (4.27)$$

Where f_p is maximum frequency and t_s is time shift and they have taken as 0.2 Hz and 5.0 sec respectively. The results are compared with the extended mesh model like the previous section. Fig. 4.5 shows the calculated displacements near the absorbing boundaries. The results show that the responses obtained using VABC are better than the responses obtained using ABC.

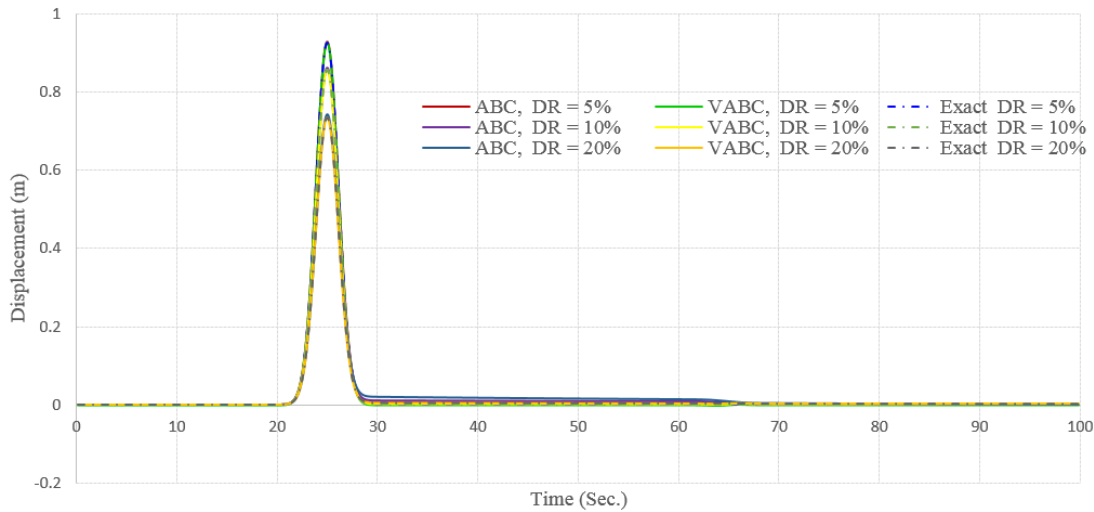


Figure 4.5. Displacements at $L=990m$ for 5%, 10% and 20% damping ratios

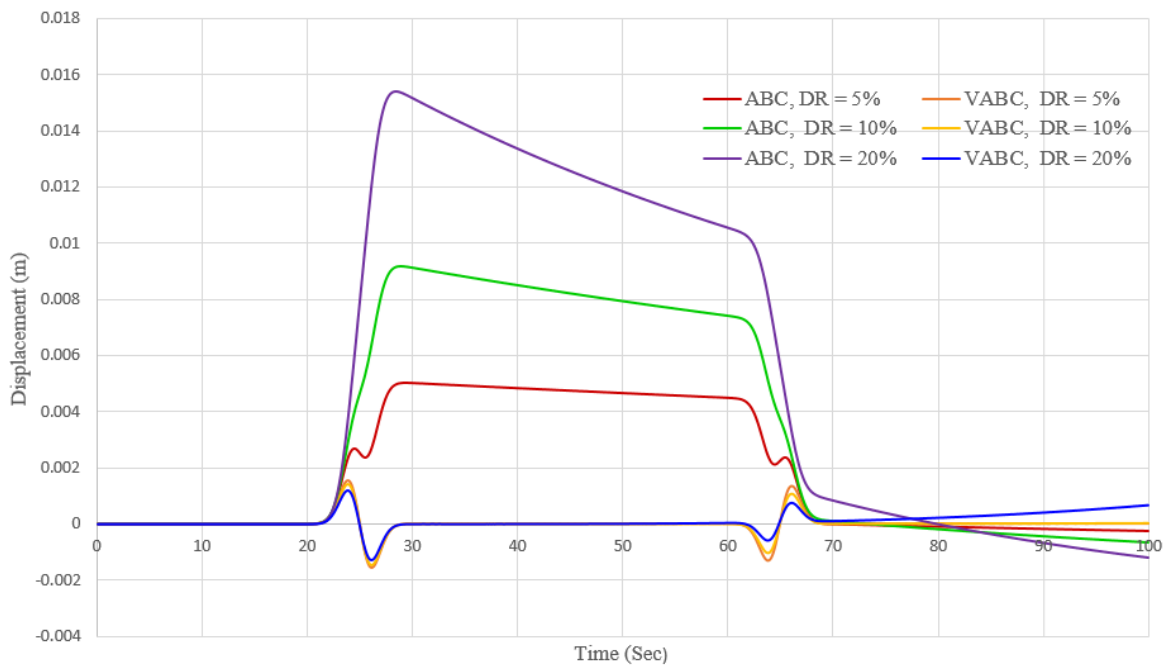


Figure 4.6. Reflections near the boundary ($L=990m$)

To compare the degree of accuracy, reflections of ABC and VABC in terms of displacements are calculated with reference to the exact solution, i.e., with an extended mesh model as shown in Fig. 4.6. It is observed that reflections are almost constant and negligible in the case of VABC. It is also observed that VABC performance decreases with an increase in damping. This behaviour is due to ignoring higher-order terms when expanding equation 4.8. It is also noted that with VABC the reflections are increasing constantly from 70 seconds due to the accumulation of error in the approximation. Therefore, for higher damping ratios, i.e., 10% or above, these boundary conditions can only be used for transient wave propagations.

4.5.2. 2D scalar P-wave propagation

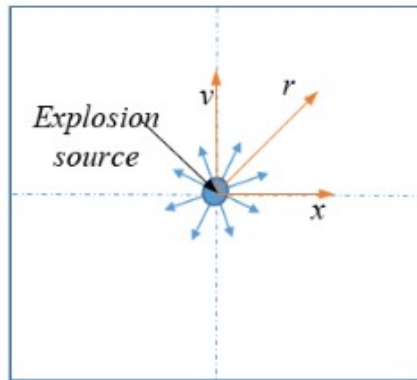


Figure 4.7 (a): Pure P-wave propagation due to explosion

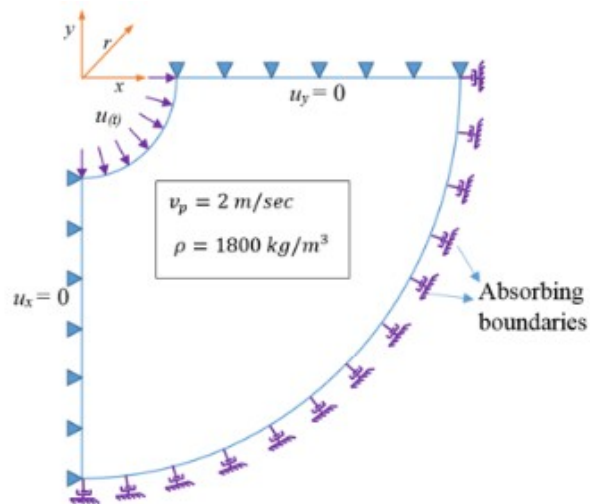


Figure 4.7 (b): One-fourth of numerical model for pure P-wave propagation

Fig

Figure 4.7. 2D Plane strain model for the pure P-Wave propagation

In this section, the efficiency of the VABC is verified using two-dimensional pure P-wave propagation resulting from the explosive source in the infinite medium under plane strain condition as described in Fig. 4.7. The time variation of the displacement at the explosion source is considered using a Ricker wavelet specified in equation 4.28.

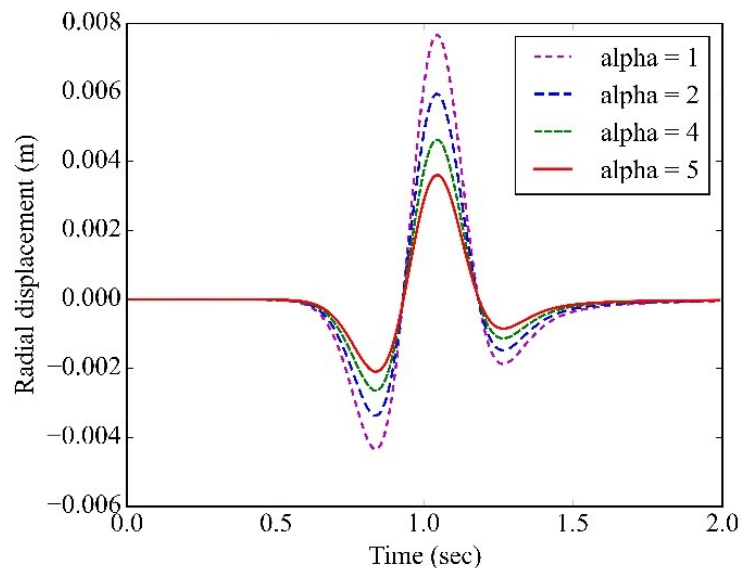


Figure 4.8. Source field displacement for the finite element model

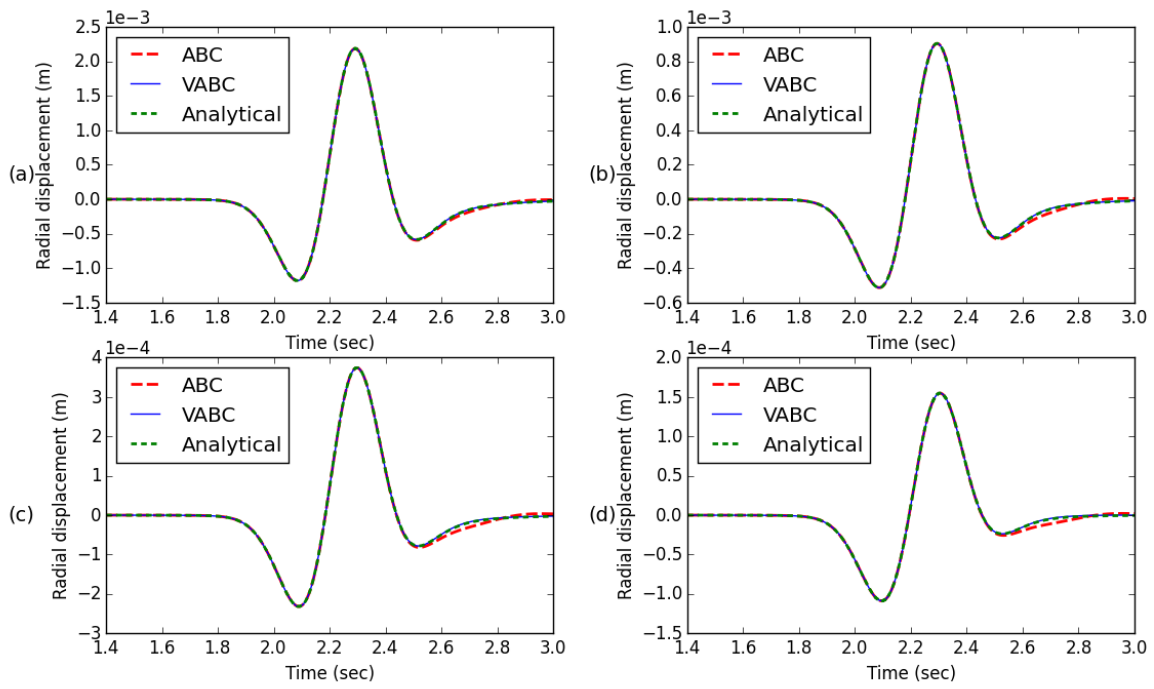


Figure 4.9. Displacements at 3.50 m radius: (a) $\alpha = 1$, (b) $\alpha = 2$, (c) $\alpha = 4$ and (d) $\alpha = 5$

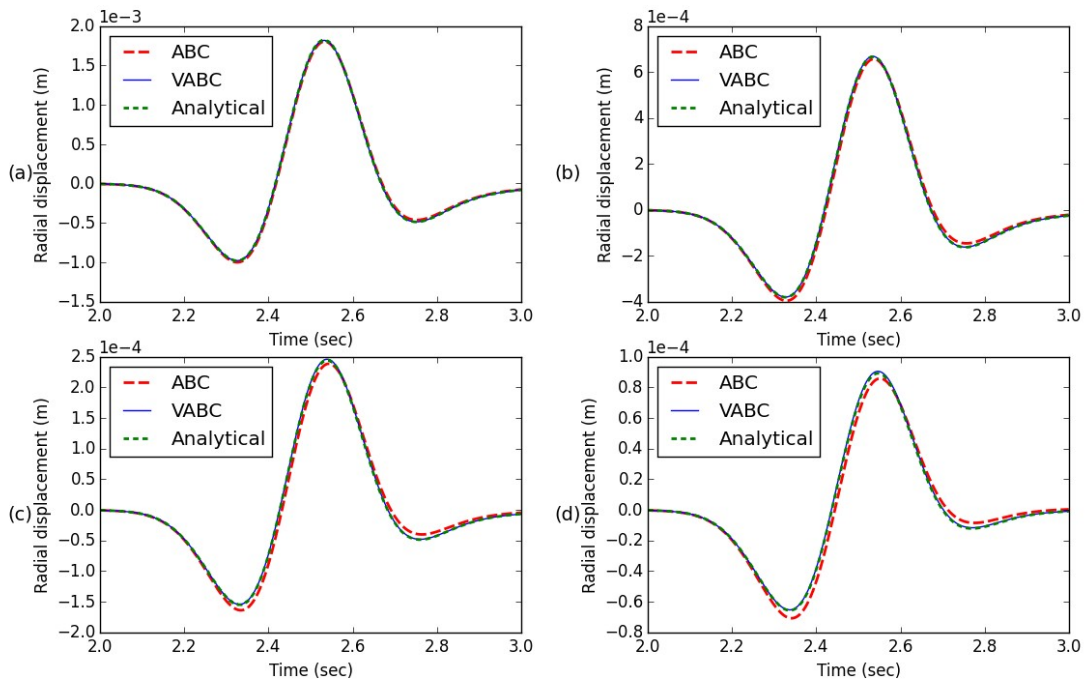


Figure 4.10. Displacements at 4.0 m radius (a) $\alpha = 1$, (b) $\alpha = 2$, (c) $\alpha = 4$ and (d) $\alpha = 5$

$$U(0, t) = A_f \left[1 - 2\pi^2 f_p^2 (t - t_s)^2 \right] e^{-\pi^2 f_p^2 (t - t_s)^2} \quad (4.28)$$

Where $U(0, t)$ is the time variation of the displacement at the explosion of the domain A_f is the amplitude, f_p is the peak frequency and t_s is time shift and the parameters used in this problem are $A_f = 10$ mm, $f_p = 2$ Hz and $t_s = 0.5$ sec.

A 1.0 m radius cavity is created around the source to apply the pressure wave and to avoid numerical instabilities due to meshing near the origin. To obtain the appropriate source field for use in the numerical method, analytical simulation to the infinite media is carried out using specified in equation 4.29

$$u(r, t) = \frac{1}{2\pi} \int_{-\infty}^{\infty} \left[-i\pi H_0^{(2)}(k * r) F_{\omega} \right] e^{+i\omega t} d\omega \quad (4.29)$$

Where r is the radial distance from the source, F_{ω} is the Fourier transform of Ricker wavelet (4.29), ω is the angular frequency, $k = \frac{\omega}{V_p}$ is the wave number. Viscosity effects are considered using the correspondence principle i.e., by replacing the elastic wave velocities with viscoelastic velocities in (4.28). The Inverse Fourier transform in equation 4.29 is performed numerically. The source field time response for different mass proportional damping coefficients, α is shown in Fig 4.8.

Due to the symmetry of the domain, only one-fourth of the domain is considered in the modelling. Horizontal displacements are fixed to zero at left end ($u_x=0$) and vertical displacements are fixed to zero at top end ($u_y=0$). The domain is truncated with 4.0 m radius and absorbing boundary conditions are applied normal to the boundary as shown in Fig. 4.7. The medium has elastic P-wave velocity $V_p = 2$ m/sec and density $\rho = 1800$ kg/m³. The wave travelling time from the source field to the boundary is approximately 1.5 sec and the simulation duration is 4 sec. The model fundamental time-period has approximately arrived using different numerical model sizes ranging from 1m radius to 8m radius and then using a nonlinear curve fitting method. The fundamental time-period of the model is estimated as 0.06 Hz.

Fig. 4.9 and Fig. 4.10 shows the displacements along the radial direction obtained using ABC and VABC boundary conditions. The results are compared with the analytical solution using equation 4.29 with viscoelastic wave properties. From the displacements, it is observed that ABC produces reflections, whereas VABC converges to the analytical solution.

Fig. 4.11, Fig. 4.12 and Fig.4.13 show the pressure contours due to p-wave propagation for different damping coefficients. The results are compared with a model where it is assumed to be infinitely extended. Since the analysis is carried out for 4 secs and p-wave velocity is 2 m/sec, the model size is selected as 7m radius so that the reflected waves will not reach the domain under consideration within the analysis time. From the contour plots, it is verified that the pressure contours with VABC are closely matching with the infinitely extended models for all the damping coefficients during the analysis.

In all the configurations including extended meshed model, stresses are present within the domain even after the waves have passed the region, this is due to gradual variation in

element size. The reflections due to gradual variation are becoming small at the source point as the damping increases, this is because reflections are absorbed as wave propagate through the domain.

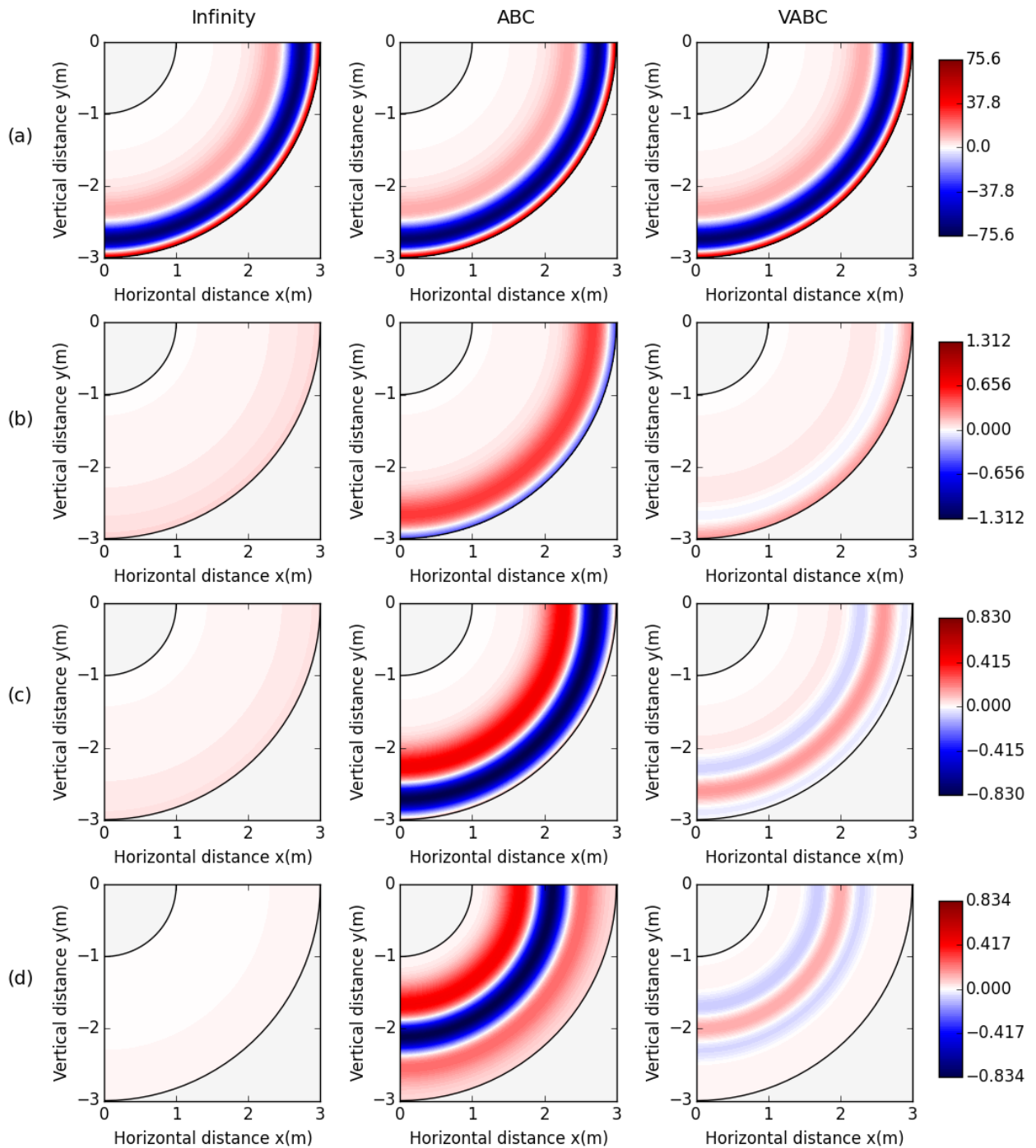


Figure 4.11. Snapshot of Pressure distribution (N/m^2) when damping coefficient, $\alpha = 1$: (a) time $t=2sec$, (b) time $t=3sec$ (c) time $t=3.2sec$ and (d) time $t=3.5sec$

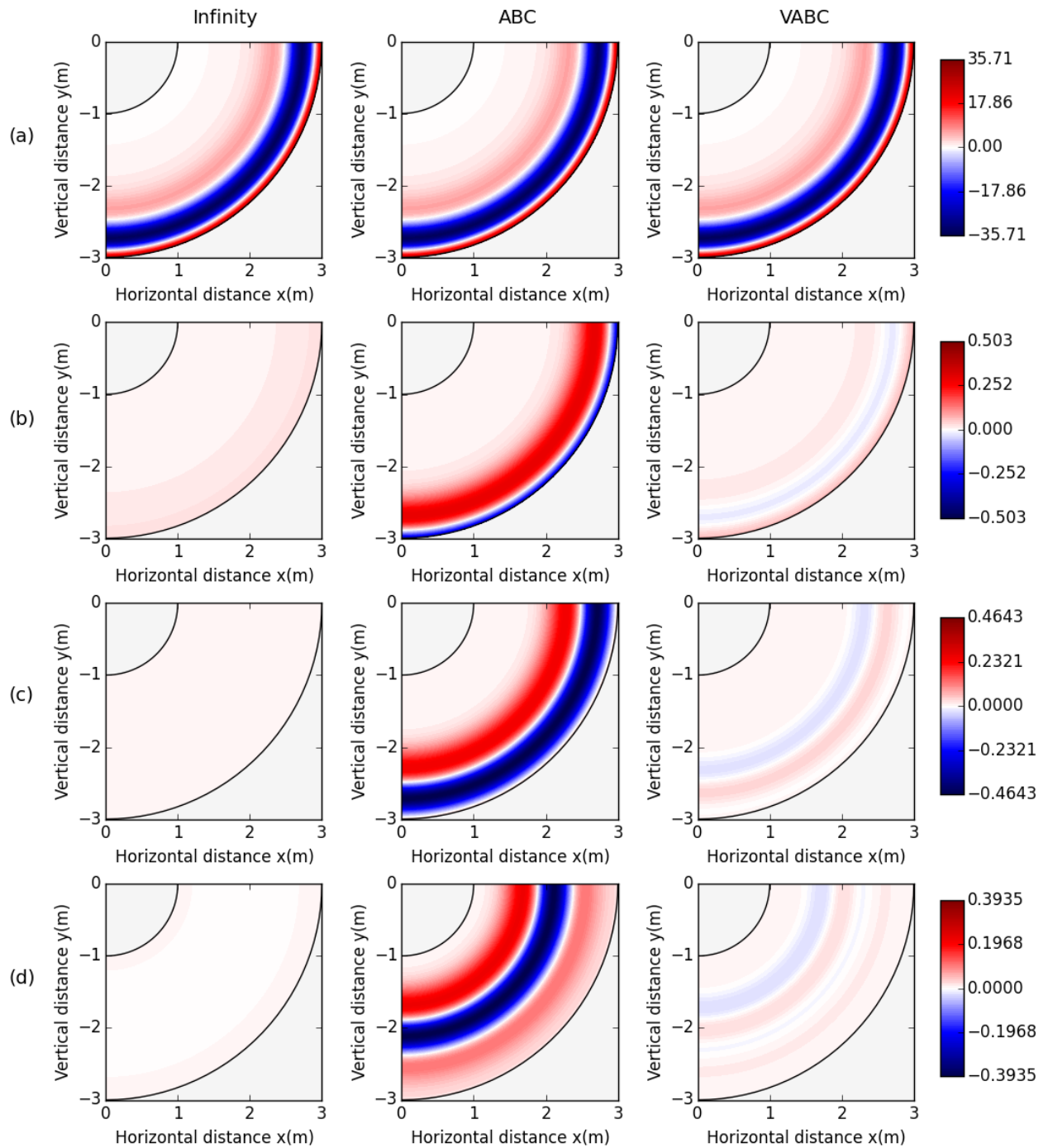


Figure 4.12. Snapshot of Pressure distribution (N/m^2) when damping coefficient, $\alpha = 2$: (a) time $t=2sec$, (b) time $t=3sec$ (c) time $t=3.2sec$ and (d) time $t=3.5sec$

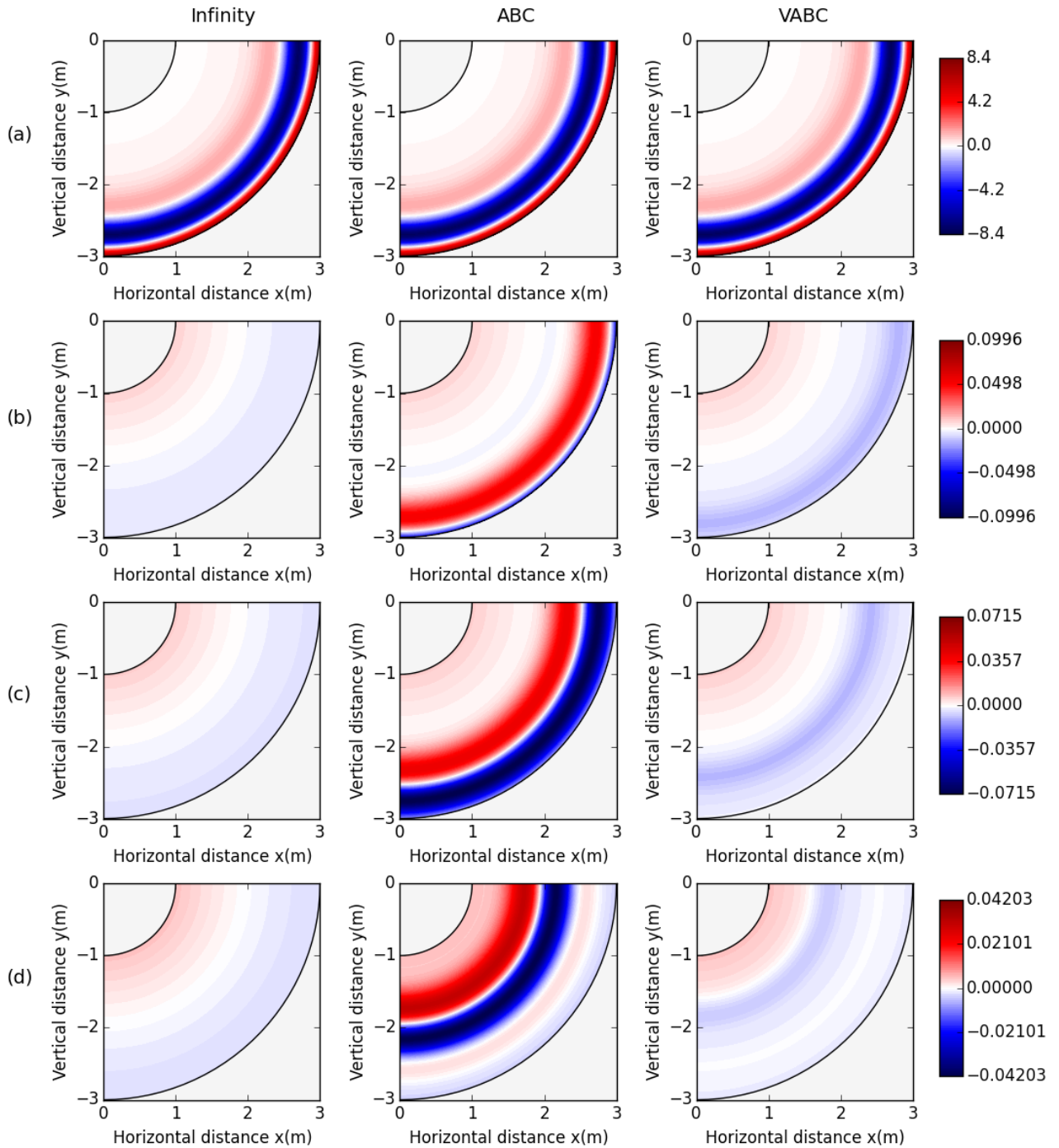


Figure 4.13. Snapshot of Pressure distribution (N/m^2) when damping coefficient, $\alpha = 4$: (a) time $t=2sec$, (b) time $t=3sec$ (c) time $t=3.2sec$ and (d) time $t=3.5sec$

4.5.3. 2D viscoelastic wave propagation

In this section, the viscoelastic wave propagation problem is verified within an infinite domain for plane strain condition as shown in Fig. 4.14. Due to the symmetry of the domain about the y-axis, right half of the domain is considered in the modelling. The domain is subjected to a vertical Ricker wavelet line load at the origin (O) as specified in equation 4.30,

$$U(0,t) = A_f \left[1 - 2\pi^2 f_p^2 (t - t_s)^2 \right] e^{-\pi^2 f_p^2 (t - t_s)^2} \quad (4.30)$$

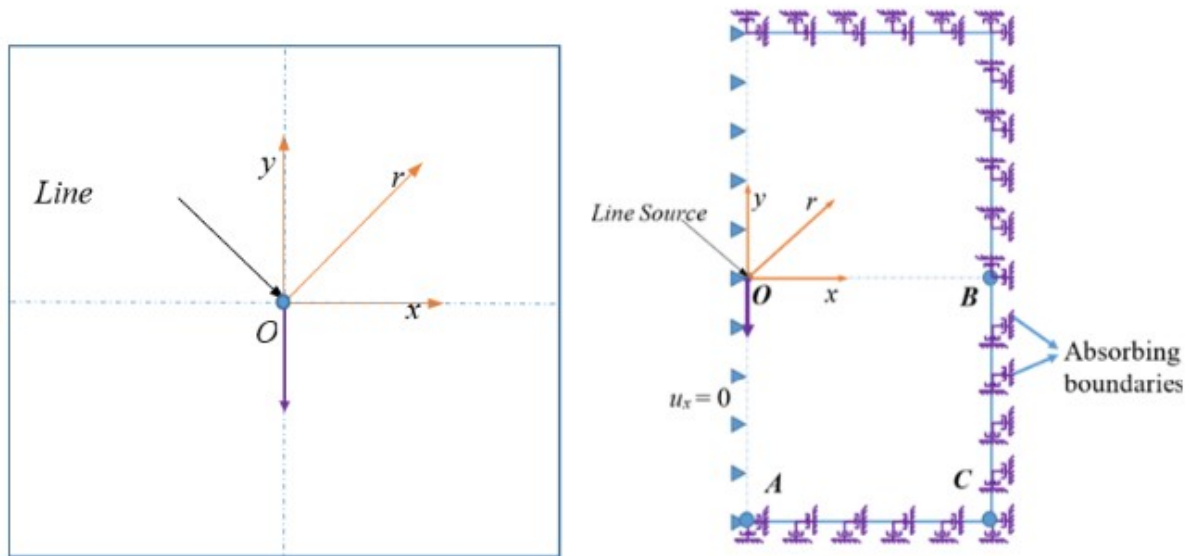


Figure 4.14. 2D Plane strain model for wave propagation

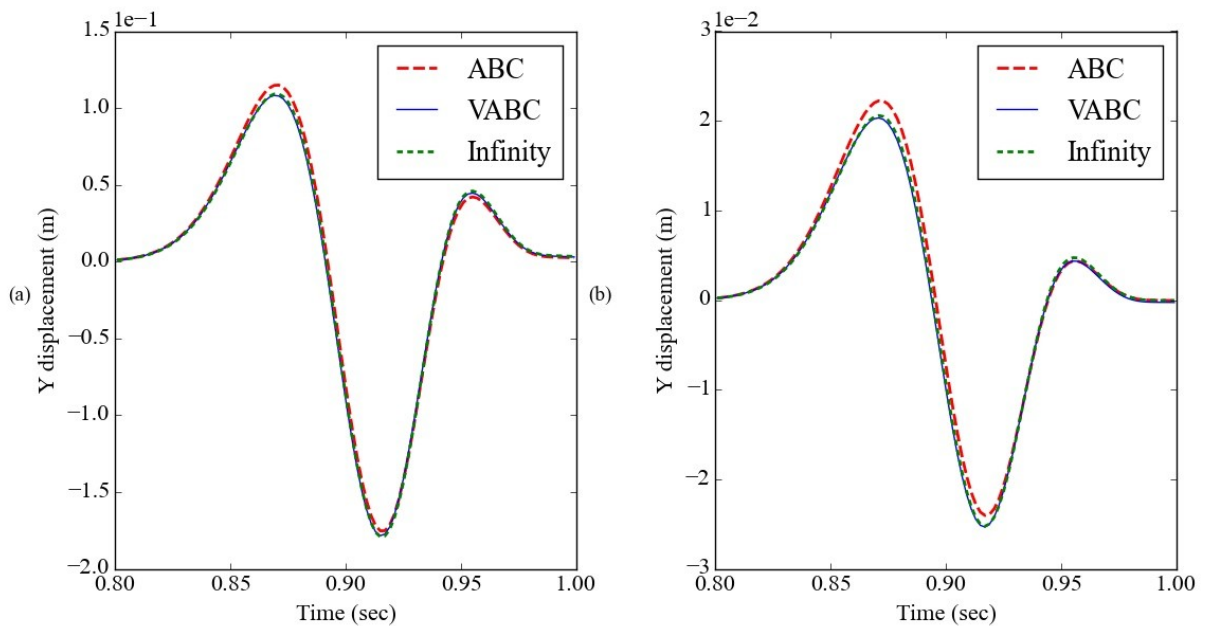


Figure 4.15. Displacements in Y direction at A: (a) damping coefficient, $\alpha = 10$, (b) $\alpha = 15$

with $A_f = 1e3$ N, $f_p = 10$ Hz and $t_s = 0.15$ sec. The medium has the material properties, mass density $\rho = 1800$ kg/m³, the P-wave velocity $V_p = 2.0$ m/s and the S-wave velocity $V_s = 1.0$ m/s. Modal dimensions are chosen as 1.5m x 3.0m. Equations 4.1 and 4.2 are used as absorbing boundaries to absorb normal and tangential energies for ABC boundary condition. Similarly, Equations 4.12 and 4.13 are used for VABC boundary condition. The time required for the wave to travel from source field to nearest point on the boundary is approximately 0.75 sec and 1.5 sec for P-wave and S-wave respectively and the simulation duration considered is 3.0 sec.

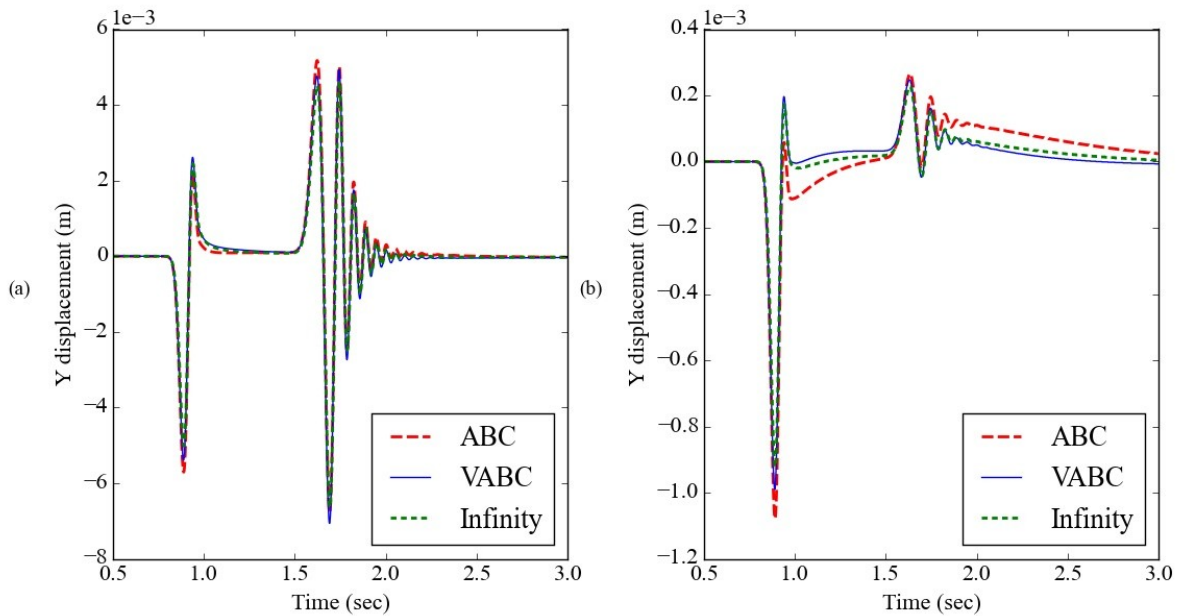


Figure 4.16. Displacements in Y direction at B: (a) damping coefficient, $\alpha = 10$, (b) $\alpha = 15$

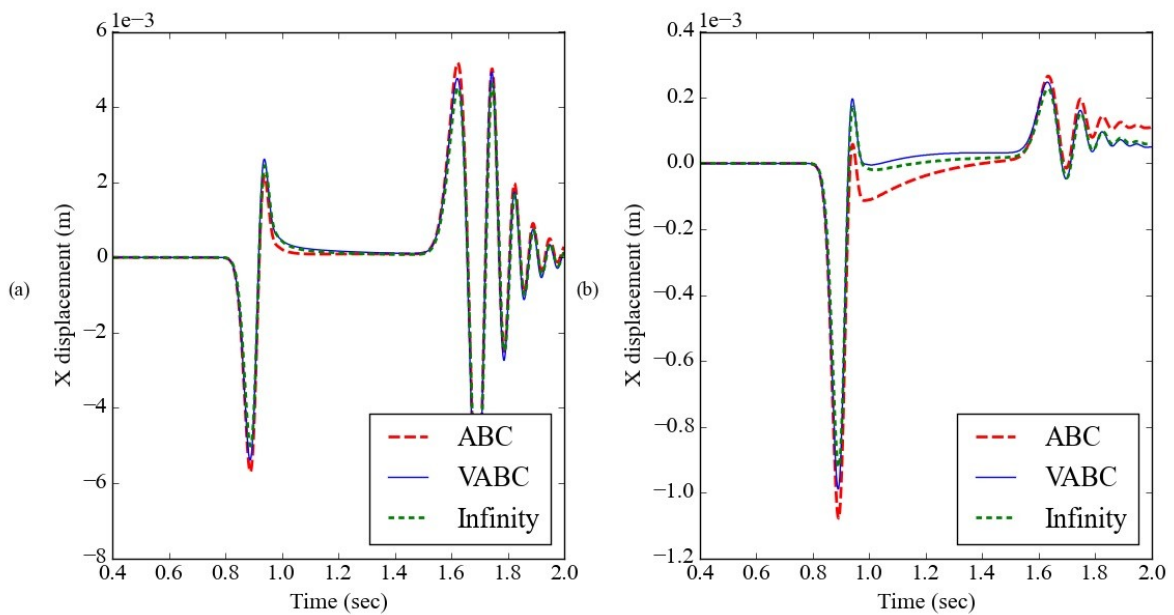


Figure 4.17. Displacements in X direction at C: (a) damping coefficient, $\alpha = 10$, (b) $\alpha = 15$

The results from ABC and VABC models are compared with an extended model (referred to as Infinity model in results) created as explained earlier for pure P-wave propagation problem. Since the analysis is carried out for 3 secs and p-wave velocity is 2 m/sec, the model size is selected so that the reflected waves will not reach the domain under consideration within the analysis time.

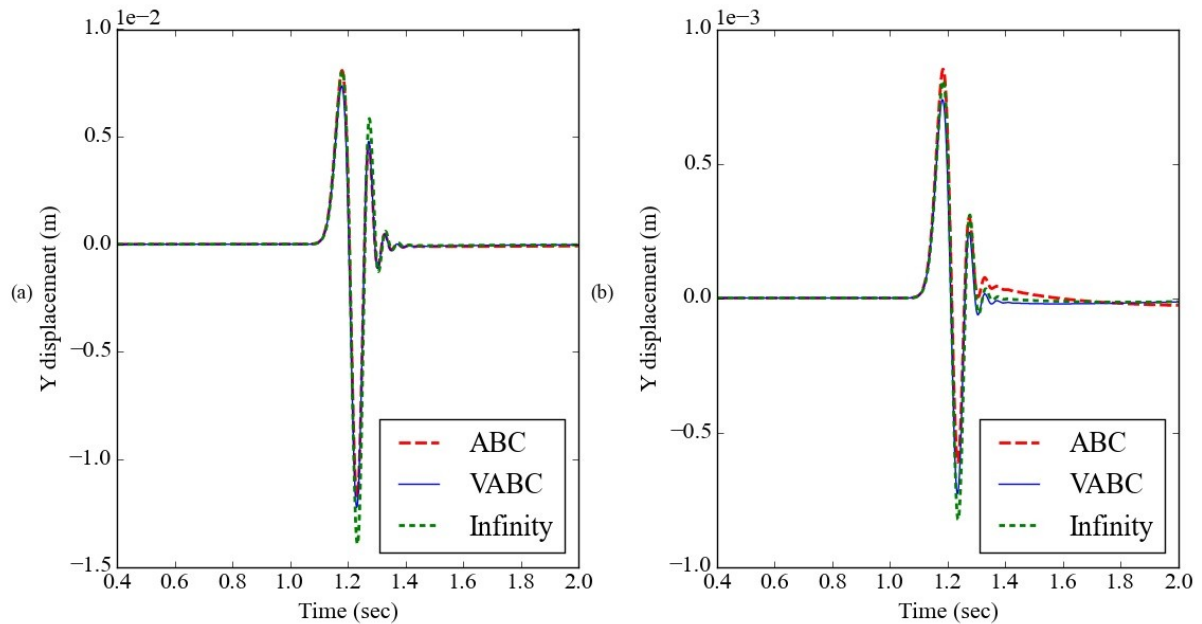
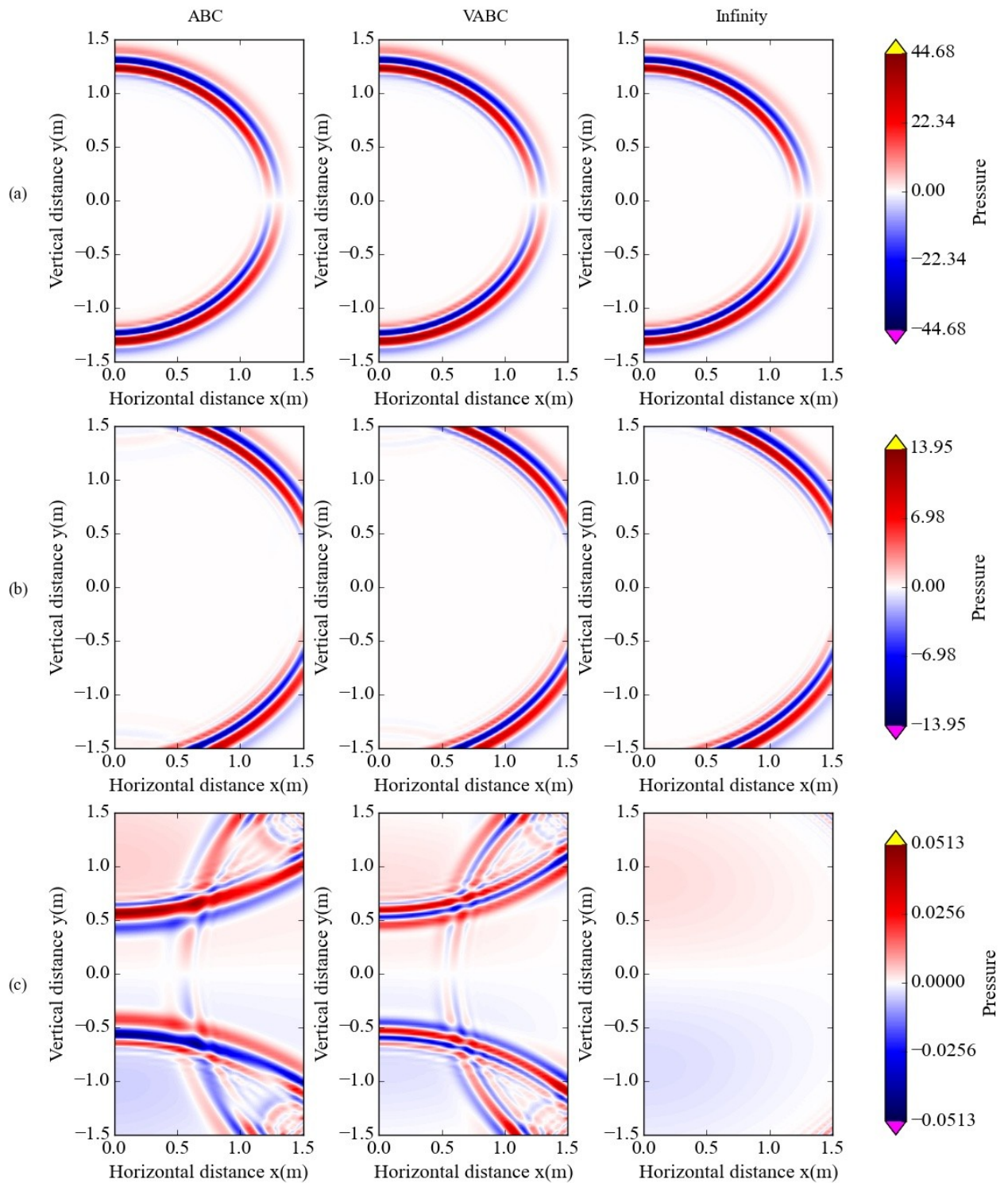


Figure 4.18. Displacements in Y direction at C: (a) damping coefficient, $\alpha = 10$, (b) $\alpha = 15$

Results are studied at three different points, 1). Point A ($x=0m$, $y=-1.5m$) at the boundary along the y-axis, 2). Point B ($x = 1.5$, $y=0$) at boundary along the x-axis and 3). Point C ($x=1.5$, $y=-1.5$) at the corner of the model. Fig. 4.15 and Fig. 4.16 shows the displacements in the Y direction at point A and point B. It is observed that the displacements with VABC converge towards the extended meshed model solution. Fig. 4.17 and Fig. 4.18 shows the displacements in X and Y directions at point C. It is also noted that displacements with ABC are slowly converging to the extended model after the wave passes the boundary due to radial damping.

Fig 4.19 and Fig. 4.20 shows the pressure and shear distribution in the model at different time intervals. This image is clear evidence that there exist reflections when the waves are reaching the boundary in an inclined direction. These reflections are dominating the viscous effects in the model. However, from Fig 4.17 (b) and Fig 4.18 (b), it is observed that the displacements with ABC have deviated from the extended model in comparison with VABC. This shows that the VABC includes the effects of the viscosity in material beyond the boundary conditions.



**Figure 4.19. Snapshot of pressure distribution (N/m^2) when damping coefficient, $\alpha = 10$:
 (a) time $t=0.8$ sec, (b) time $t=1.0$ sec and (c) time $t=1.1$ sec**

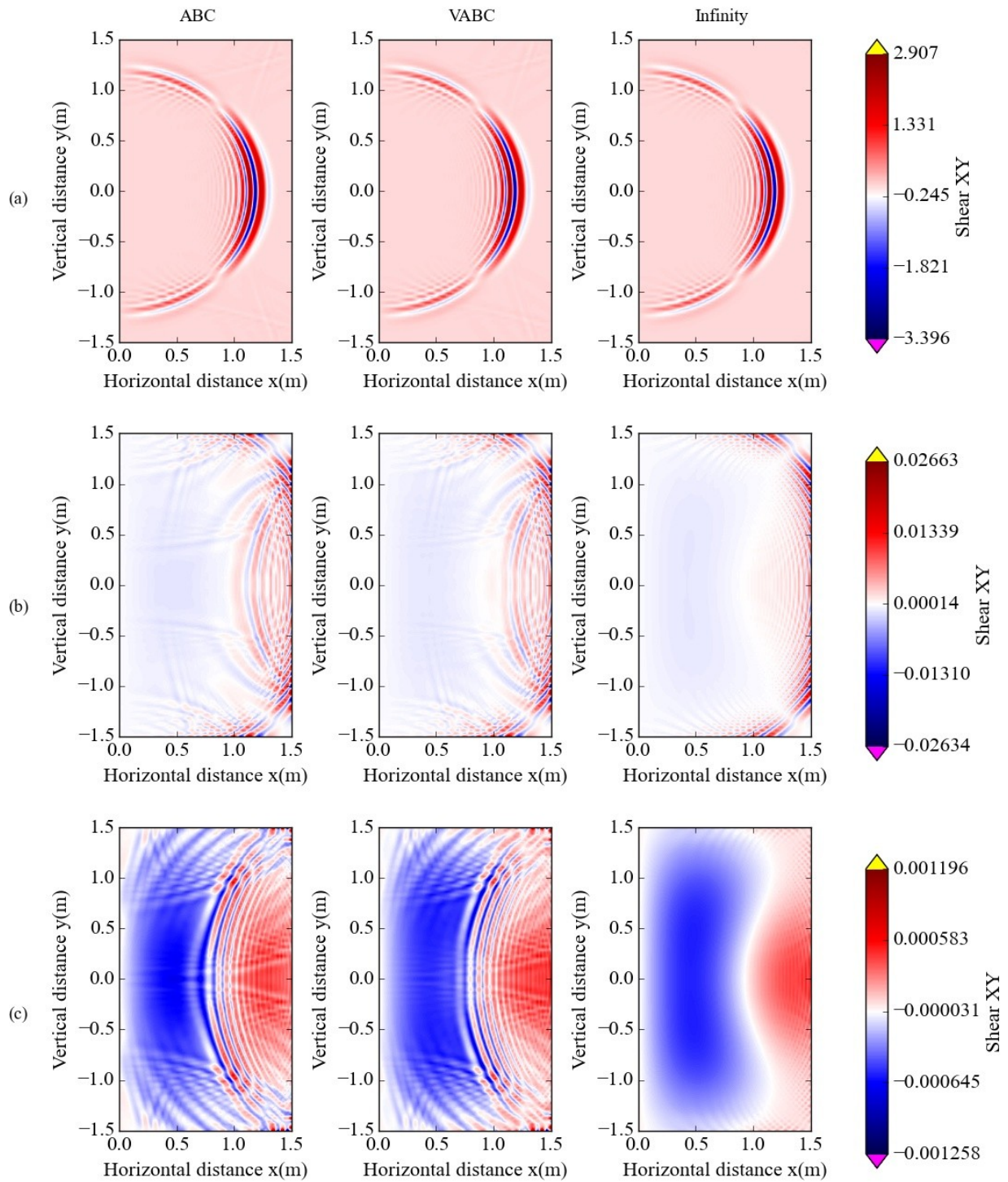


Figure 4.20. Snapshot of shear stress distribution (N/m²) when damping coefficient, $\alpha = 10$: (a) time $t=1.4$ sec, (b) time $t=2.1$ sec and (c) time $t=2.5$ sec

4.6. Conclusions

The equations for absorbing boundary conditions under Maxwell-type viscoelastic wave propagation were developed. Mass-proportional Rayleigh damping is applied for numerical modelling, and the following conclusions were drawn from the study:

1. Standard Absorbing Boundary Conditions are yielding reflections when material damping is included, and the reflections are increasing as the damping increases. The proposed method produces very less or negligible reflections under viscoelastic wave propagation when the waves impinge on the boundary in the normal direction.
2. when using standard ABC in presence of material damping factious permanent deformations are developed in the numerical model. With the proposed approach, the deformations are in very good agreement with the extended mesh model.
3. When the wave impinges the boundary other than normal direction, both ABC and VABC produce reflections. But the displacements in case of VABC are better converging towards the extended mesh model.
4. For higher damping ratios i.e., above 10%, the performance of the proposed boundary conditions is degrading. It is also concluded that reflections aggregating at higher damping ratios increase with the analysis time. This suggests that the VABC convergence needs to be improved for higher damping ratios.
5. The procedure applied in the method does not converge when stiffness-proportional damping is present. Therefore, the stiffness proportional damping terms are dropped in the final equations. If stiffness proportional damping is present in the domain, there is no advantage in using this method

5. Absorbing Layers combined with VABC (ALID+VABC)

5.1 Introduction

The major goal of this section is to present a method to combine the absorbing layers and absorbing boundary conditions to provide efficient boundary conditions. Israeli and Orszag (1981) tried to combine both ABC and absorbing layers to achieve optimum efficiency, in which the absorbing layer properties are modified such that the damping coefficient is zero at the boundary. The damping properties are gradually increased from zero at the beginning to a maximum in the middle of the layers and then reduced to zero at the end of the absorbing region. This method needs twice the number of layers compared with that required for ALID.

In this study, a method is proposed to avoid the damping mismatch by adjusting the damping characteristics of VABC. The VABC viscous damping parameters are matched with the last absorbing layer (ALID) near the boundary. In the subsequent sections, the methodology and numerical validation examples to evaluate the efficiency of the proposed approach are presented.

5.2. Theory

First, the ALID and VABC boundary conditions are reviewed, and later, the procedure to combine both the boundary conditions and the proposal for new boundary conditions are explained.

5.2.1 Absorbing Layers by Increasing Damping (ALID)

The ALID method uses a material with gradually increasing Rayleigh damping in successive layers such that they absorb incident wave energy and the reflections due to impedance mismatch in successive layers is minimum. At the beginning of the absorbing region, the damping is kept equal to the damping in Area of Study (AoS), zero in most cases and maximum at the end of the absorbing region. Thus, the wave entering the absorbing region is gradually dampened in the absorbing layers.

To define an effective absorbing region, it is necessary to optimize the variables such as Rayleigh damping coefficients, absorbing region length, and number of elements in ALID. It is noted that introducing damping into the model can decrease the value of the stable time increment within explicit schemes, thereby reducing computational efficiency. However, a high value of causes only a small decrease in the stable increment as compared to that of. It is therefore avoided in the absorbing region to eliminate the time stepping issue and allow efficient computation since the mass matrix in explicit schemes is usually diagonal. Rajagopal et al. (2012) and Pettit et al. (2014) provided the underlying theory to define the optimal values for the absorbing region. This summarises to

- The total thickness of the absorbing layer, $L = 1.5$ times the incident wavelength
- The maximum damping coefficient $\alpha_M = \omega$, where, ω is the incident wave frequency

- The damping coefficient, $\alpha = \alpha_M \left(\frac{x}{L} \right)^p$, where, attenuation factor, $p = 3$ and x is the distance from AoS. $x=0$ at the beginning of the ALID and $x=L$ at the end of ALID.
- The mesh density i.e., a minimum number of elements should be 20 per wavelength.

5.2.2 Combining ALID and VABC

The local absorbing boundaries (ABC and VABC) are excellent at absorbing the waves impinging in normal direction but produces the reflections when impinge other than normal direction. Therefore, the absorbing layers will be added before VABC to reduce spurious reflections when the wave is propagating in an inclined direction. The increase in mass proportional damping in successive layers not only attenuate the wave energy but also increase the imaginary part of complex density. The increase in complex density causes a reduction in wave propagation velocity and thus a change in the direction of wave propagation in accordance with Snell's law, which describes the relationship between incidence, reflection, and refraction angles (Rajagopal et al., 2012).

For low incident angles, the change in the angle in successive layers is small and hence 45° and above incident angle are considered. The change in the wave propagation angle when propagating through absorbing layers is shown in Fig. 5.1, wherein 30 absorbing layers are provided with cubic variation in damping properties.

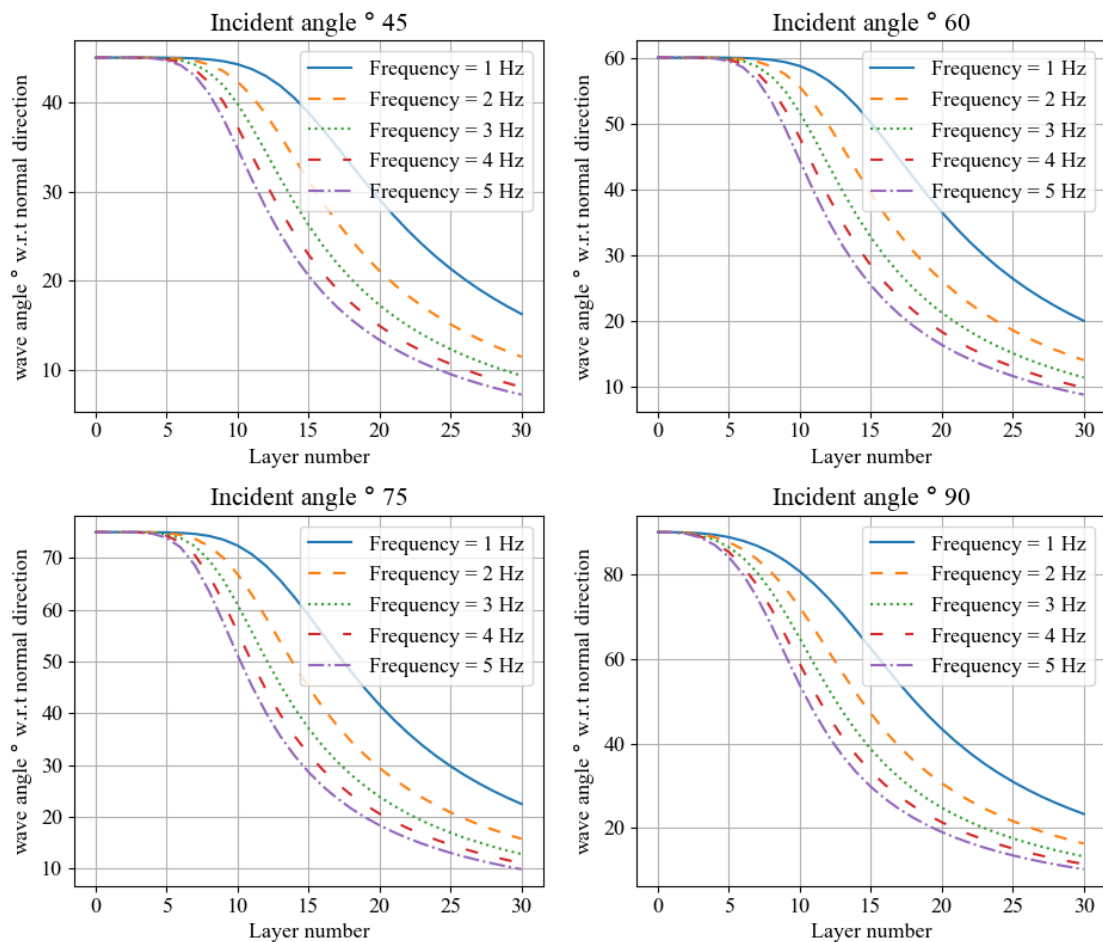


Figure 5.1: Wave propagation angle change when propagating through absorbing layers

The incident angle of the wave is reduced with respect to its normal direction while propagating through absorbing layers. This property of the absorbing layers allows the VABC to absorb the wave propagation energy efficiently. It is noted that high-frequency waves induce more damping and, hence, the wave angle reduces more compared with low-frequency waves.

To achieve optimum performance when combining the ALID and the VABC, it is necessary to avoid the impedance mismatch between the last absorbing layer and VABC. Replacing α and β with the maximum damping coefficients α_M and β_M respectively in equation 4.12 and 4.13

$$\sigma = a \rho V_p \dot{u} + 0.5 a \rho V_p \alpha_M u \quad (5.1)$$

$$\tau = b \rho V_s \dot{v} + 0.5 b \rho V_s \alpha_M v \quad (5.2)$$

From the above equations, it can be observed that to combine VABC with ALID, it requires modelling a dashpot with a coefficient $a \rho A V_p$ and a spring with coefficient $0.5 \alpha_M a \rho A V_p$. The spring constant $0.5 \alpha_M a \rho A V_p$ is added in addition to the standard ABC to match the impedance between the ABC and the last absorbing layer. It is also noted that the spring computations and dashpot computations are simple and require a one-time computation at the beginning of the analysis. Therefore, the additional computational cost to combine VABC with ALID is negligible.

5.3. Numerical examples

The efficiency of proposed boundary conditions is verified through various numerical examples, and the results are validated with standard solutions. Numerical examples include the verification of reflection when the waves impinge the boundary other than the normal direction in normal 1D, 2D scalar wave propagation problem and 2D elastic wave propagation using the finite element analysis with explicit time integration scheme.

5.3.1. 1D p-wave propagation

In this section, the efficiency and performance of the proposed boundary conditions are validated for 1D wave propagation models. Two test cases were analyzed: a first test case to study the performance and a second test case to study the efficiency of the method. In the later test case, the efficiency is estimated based on the number of additional degrees of freedom required to model the boundary conditions. Sensitivity analysis is also carried out in the later subsections to study the applicability of the method for different loading frequencies.

5.3.1.1. Performance case study:

A one-dimensional model is created to model the elastic wave propagation, as shown in Fig. 5.2. The model is idealised using two node bar elements. The material is elastic, Young's modulus and density are taken as 7200 N/m^2 and 1800 kg/m^3 , respectively. The model is assumed to be subjected to a predominant wave frequency (f) of 1 Hz. The primary wave velocity (V_p) and wavelength (λ) are calculated as 2 m/sec and 2 m for the incident wave. The length of the model (Area of Study, AoS) is considered to be 5λ i.e., 10m. The length of each bar element is taken as 2 mm, and the cross-sectional area is taken as 0.1 m^2 . The length of

the element is arrived such that the change in displacements and stresses in the element is negligible with further reduction in element size.

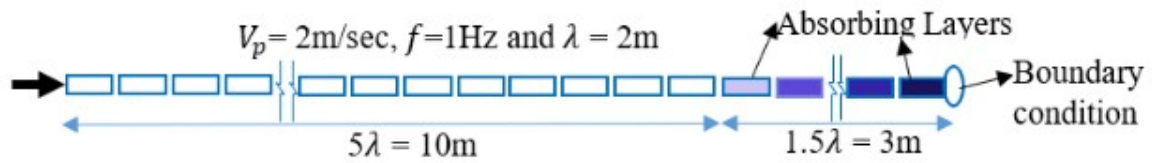


Figure 5.2. Configuration for one-dimensional wave propagation model

Three different configurations for radiating boundaries are used: 1. ALID, 2. ALID+ABC, and 3. ALID+VABC. The same absorbing layer properties are applied for all three configurations. The length of the absorbing region is taken as 1.5λ , and the element length is the same as in the area of study (AoS) region, i.e., 2 mm. The damping properties are varying along absorbing layers using cubic profile, $\alpha = \alpha_M \left(\frac{x}{L}\right)^3$. The damping coefficient (α) is considered as 0 and (α_M) at the beginning and end of the absorbing region, respectively and $\alpha_M = \omega = 2\pi f$. Results from all three models are compared with the infinitely extended model, where the model length is such that the reflection from the boundary will not reach the AoS during the analysis.

The load is applied at the left end of the member, and the wave travel time to reach absorbing layers is 5 sec. The analysis has been carried out for 20 seconds to study the effects of the wave's reflections. Ricker wavelet load given in equation 5.3 is chosen to apply as the predominant frequency

$$U(0, t) = A_f \left[1 - 2\pi^2 f_p^2 (t - t_s)^2 \right] e^{-\pi^2 f_p^2 (t - t_s)^2} \quad (5.3)$$

Where A_f is the amplitude, f_p is the peak frequency and t_s is time shift and the parameters used in this problem are $A_f = 1$ N, $t_s = 4$ sec. Peak frequency, f_p is the designed load frequency 1Hz.

The wave propagation forces in the middle of the AoS region are shown in Fig. 5.3. It is noted from the figure that the reflections due to ALID alone give about 10%, and when it is combined with ABC and VABC, the reflections are reduced to 2% and 1.5%, respectively. It is also observed that the initial reflections follow the same pattern for all three configurations, and then all of them diverge. This indicates that the reflections due to the gradual variation of the damping properties in the successive layers in the case of ALID+VABC are predominant. ALID with ABC produces more reflections when compared to ALID with VABC as the boundary impedance is not matched with absorbing layers. However, the last two configurations are performing better than ALID alone.

Fig. 5.4 shows the displacements due to wave propagation in the middle of the AoS region. From the figure, it is shown that the reflections due to ALID alone are about 15%, and when it is combined with ABC and VABC, the reflections are reduced to 8% and 5%, respectively. It is also observed that the initial reflections follow the same pattern for all three

a

b



configurations, and then all of them have various trends. The reason for having different patterns is due to the damping of the waves in absorbing layers as well as near the boundary. The energy absorbed in absorbing layers does not allow to resemble the wave propagation when the wave really passes the boundary location. This indicates that the displacements due to wave propagation in the infinite medium cannot be obtained exactly with an absorbing layer, though these layers are efficient at absorbing the wave energy.

Figure 5.3. Forces at 5m: a) full-time record and b) zoomed response

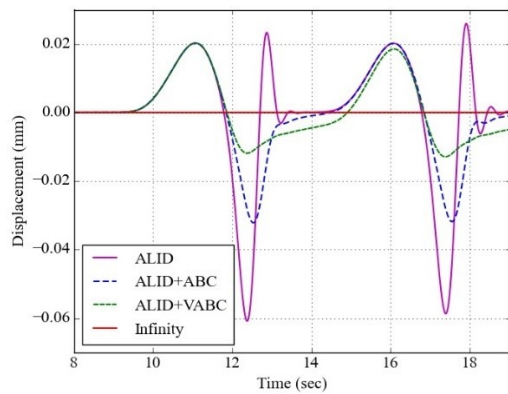
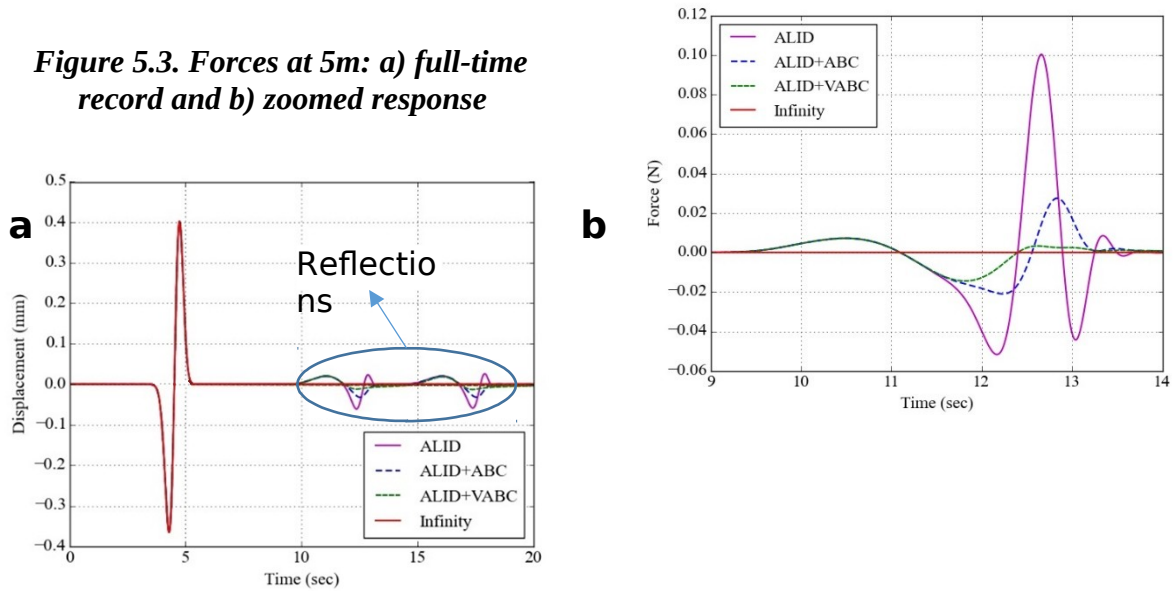


Figure 5.4. Displacement at 5m: a) full-time record b) zoomed response

5.3.1.2. Efficiency case study:

In this section, the efficiency and performance of the proposed boundary conditions are evaluated by choosing different absorbing region lengths. First, the efficiency of the method is analyzed for the effect of element size in the AoS. Later, the efficiency is verified by changing the number of elements while keeping the element length constant. Three different configurations for radiating boundaries are used: 1. ALID, 2. ALID+VABC, and 3. SRM.

Varying element length:

A one-dimensional model is created that is similar to the model created in Section 5.3.1.1. Young's modulus and density are taken as $18.0 \times 10^6 \text{ N/m}^2$ and 1800 kg/m^3 , respectively. The model is assumed to be subjected to a predominant wave frequency (f) of 1 Hz. The primary wave velocity (V_p) and wavelength (λ) are calculated as 100 m/sec and 100.0 m for the incident wave. Results are analyzed to study the effect of element size and the number of elements in the absorbing region.

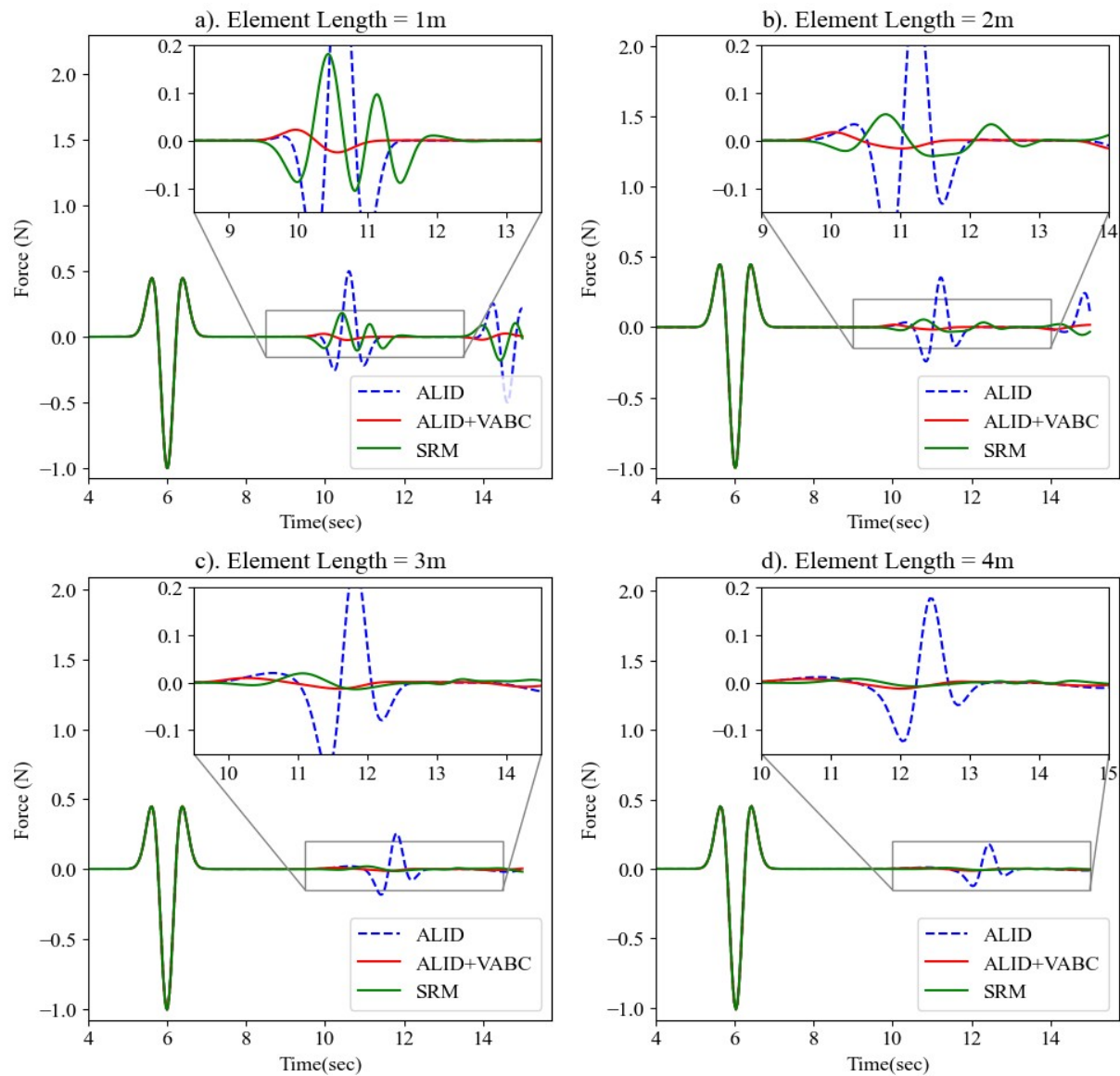


Figure 5.5: Forces at middle of AoS i.e., at 200 m

Fig. 5.5 shows the time history of the forces in the middle of the AoS region when 30 elements are provided in the absorbing region. It is observed that all the methods give less reflection as the size of the element increases from 1 m to 4 m. This indicates that all the methods perform better as the absorbing region length increases. Numerical results show that the ALID+VABC approach produces negligible reflections, i.e., in the range of 0.0245 N to 0.0155 N, i.e., 2.44% to 1.55%, as element size increases from 1 m to 4 m, which proves to be promising for large range mesh sizes. Whereas, in the case of ALID, this reflection varies

from 0.5 to 0.2 N, i.e., 50% to 20% when element size increases from 1 m to 4 m, respectively. This indicates that ALID is poorly performing as the absorbing boundary when the absorbing region is smaller than 1.5 times the wavelength. SRM also shows negligible reflections for 3 and 4 mm, i.e., for coarse mesh. But, not found to be promising for element size 1m and 2m i.e., for fine mesh where the absorbing region length is less than wavelength.

Fig. 5.6 shows the maximum percentage of reflections for different element lengths along with a varying number of elements. The results show that SRM performed better than ALID+VABC in two cases. 1) when larger element size used in the absorbing region, 2) a greater number of elements provided so that the absorbing region length is equal to wavelength or more. The first case, i.e., the element length, shall be determined by the model accuracy in terms of the FE solution but not the absorbing boundary design, and the second case causes a larger model size in 3D. This was found to be a limitation in both ALID and SRM but not in the ALID+VABC boundary condition. Also, the reflections in the SRM and ALID+VABC methods are already negligible in both cases.

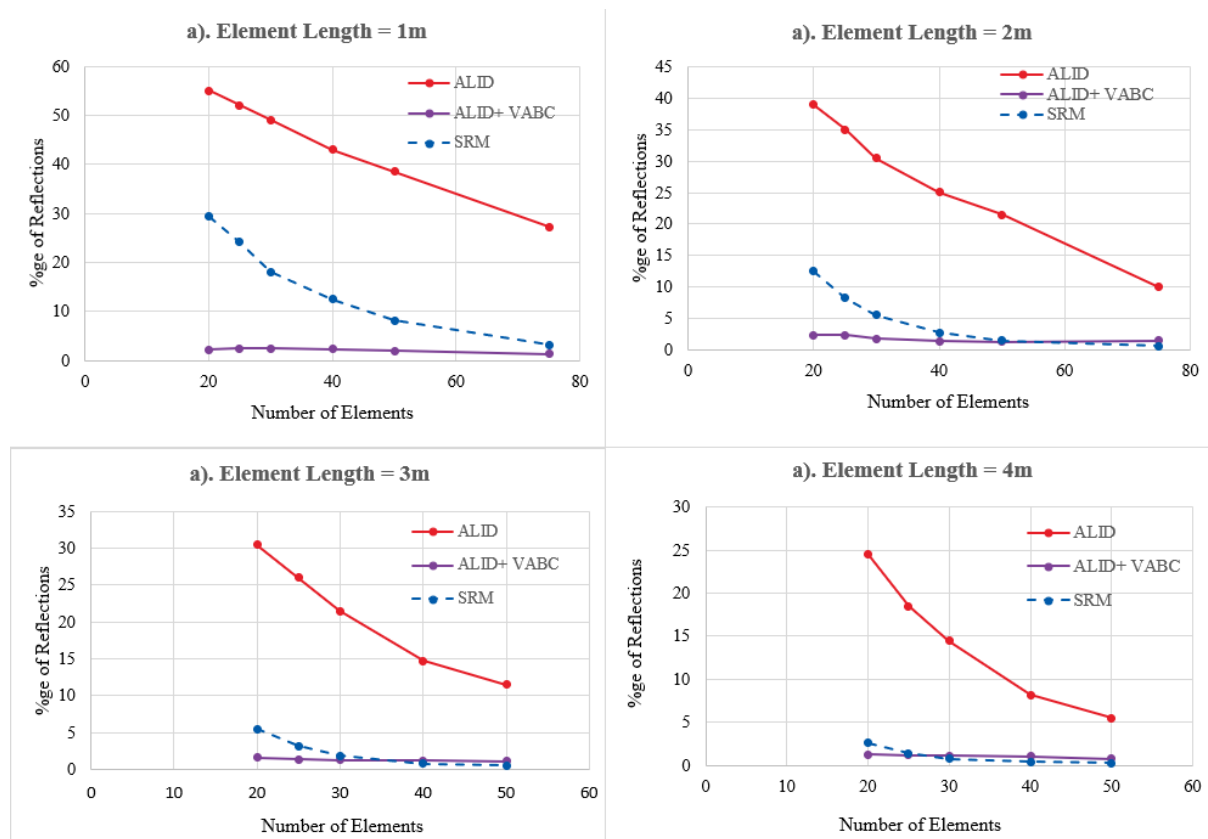


Figure 5.6: Maximum percentage of reflections

Constant element length:

In this section, the efficiency and performance of the proposed boundary conditions are evaluated by choosing different absorbing region lengths. The one-dimensional model created in the previous section (as shown in Fig. 5.2) is used. The material properties and loading content are unchanged. The element length is arrived at by providing 20 elements per wavelength, i.e. $2m/20 = 0.1m$. The model is analysed for two different configurations using the absorbing region lengths as λ and 1.5λ , where λ is the wavelength. In the first case, 20

elements are provided in the absorbing region, and in the latter case, 30 elements are provided.

Fig. 5.7 shows the wave propagation forces in the middle of the AoS region. From the figure, it is observed that the reflections due to ALID alone yield about 20% and 10% when absorbing region equal to λ and 1.5λ , respectively. The reflections in the ALID+VABC configuration are reduced to 3% and 1.5% for the absorbing region lengths equal to λ and 1.5λ , respectively. This shows that even when the length of the absorbing region in ALID+VABC configuration is taken as λ , it performs better than ALID with absorbing region length as 1.5λ .

Fig. 5.8 shows the displacements due to wave propagation in the middle of the AoS region. From the figure, the reflections due to ALID alone give about 25% and 15% when absorbing region lengths equal to λ and 1.5λ respectively. The reflections are reduced to 8% and 5% for absorbing region lengths equal to λ and 1.5λ respectively. It is also noted that the displacements are almost the same in both configurations after the wave passes in the case of ALID+VABC. This indicates that most of the reflection occurs due to an impedance mismatch between the elements.

This study concludes that, for a design load frequency, the length of the absorbing region can be reduced to λ when using ALID+VABC, against to 1.5λ when using ALID. The reduction in absorbing layers in 3D wave propagation impact heavily in terms of total number degrees of freedom.

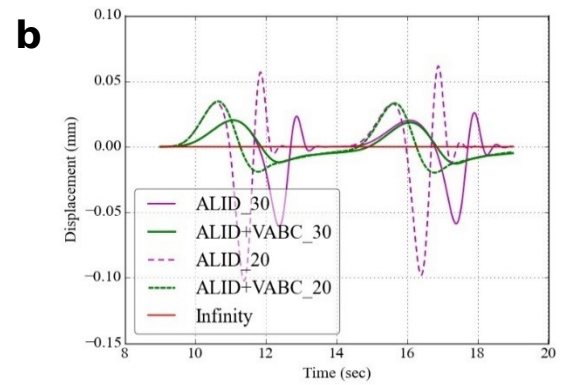
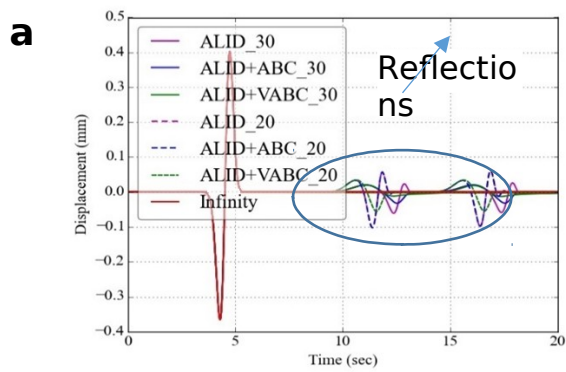
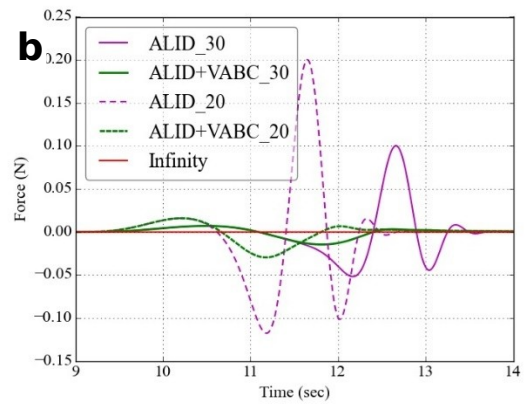
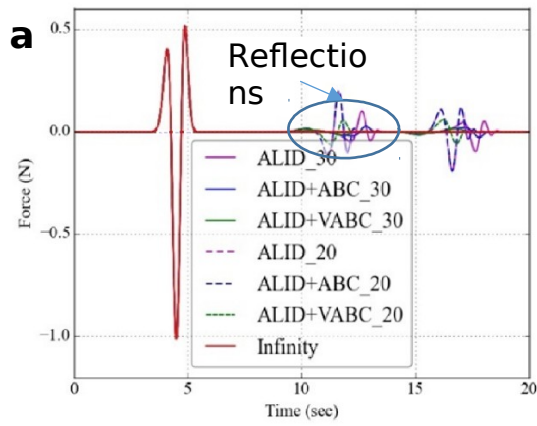


Figure 5.7. Forces at 5m for 1.5λ and λ : a) full time record, and b) zoomed response

Figure 5.8. Displacements at 5m for 1.5λ and λ : a) time history, and b) zoomed response

5.3.1.3 Sensitivity Analysis:

The optimal parameters of ALID are dependent on the loading frequency, and the damping of the waves is dependent on the system's natural frequencies in absorbing layers (Rayleigh damping). It is not always possible to clearly estimate the loading frequencies, or it may happen that a wide range of frequencies is relevant. Therefore, two types of sensitivity analysis have been carried out to check the validity of the method. The first validation test is to verify the performance of the method at different design load frequencies, and the second test is to verify the performance at different loading frequencies against the designed load frequency.

The effectiveness of the proposed method can be evaluated by measuring the absolute maximum error introduced in the solution due to the reflections. The error is calculated in AoS as a difference in results between the configuration model and the infinitely extended model (i.e., the reflection from the boundary will not reach AoS during the analysis time).

5.3.1.3.1 Validation for design loading frequencies:

In this example, error analysis is carried out for different loading frequencies. A one-dimensional model like Fig. 5.2 with all three different configurations is created for each of the loading frequencies. The model parameters, such as length of the element, length of the absorbing region, etc., are explained in Table 5.1. Material properties are considered the same as in the previous section, i.e., Young's modulus and density are taken as 7200 N/m^2 and 1800 kg/m^3 , respectively and the primary wave velocity, V_p is 2 m/sec .

Table 5.1. One dimensional model parameters:

Design Frequency	α_M	Time Step	Length Of AoS	Element Length	Number of ALID Nodes	λ (m)	Length of ALID (m)	Total Number of Nodes	Total length (m)
0.5	π	0.002	10	0.01	600	4.0	6.0	1601	16.0
1	2π	0.002	10	0.01	300	2.0	3.0	1301	13.0
2	4π	0.002	10	0.01	150	1.0	1.5	1151	11.5
5	10π	0.002	10	0.01	60	0.4	0.6	1061	10.6
10	20π	0.0005	10	0.002	150	0.2	0.3	5151	10.3
20	40π	0.00012	10	0.005	300	0.1	0.15	20301	10.15

		5							
--	--	---	--	--	--	--	--	--	--

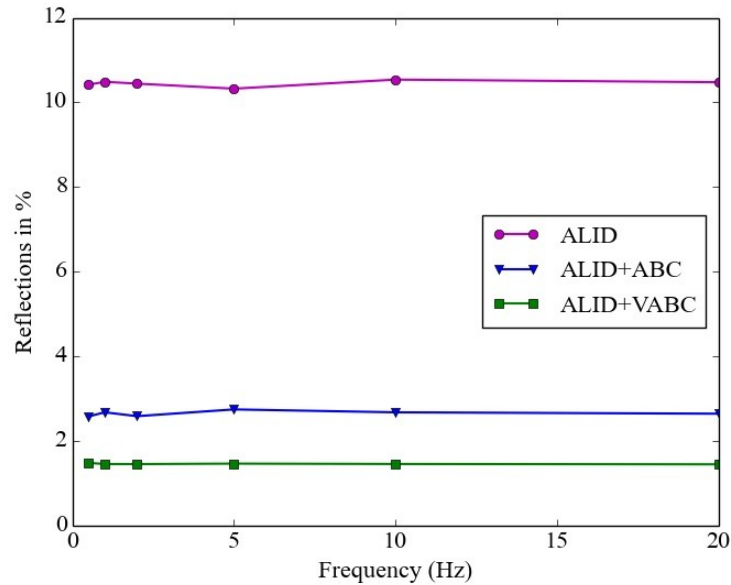


Figure 5.9. Percentage of reflection vs load frequency for 1D wave propagation

Absorbing region length is considered to be 1.5λ . Ricker wavelet variation force as defined in equation 4.63 is applied at the left end of the model. The wavelet parameters used in this section are $A_f = 1$ N, $t_s = 4$ sec. Peak frequency, f_p is the designed frequency as shown in Table 5.1.

Fig. 5.9 shows the absolute maximum percentage of reflections in forces for different design loading frequencies. These results show that the effect of the natural frequencies of the model is negligible on the performance for all different loading frequencies when the absorbing layers and boundary conditions are correctly defined for the designed load frequency.

5.3.1.3.2 Validation for loading frequencies against design frequency:

In this example, the proposed methodology is verified for performance when the model is subjected to different loading frequencies other than the designed load frequency. The one-dimensional model is created with 2 Hz as a design loading frequency. The material parameters are taken from Section 5.3.1.3.1, and the model parameters as well as boundary conditions are defined in Table 5.1 for a loading frequency of 2 Hz. The model is subjected to Ricker wavelet loading as defined in equation 5.3 with different peak loading frequencies. The frequency range varies from 0.5 Hz to 20 Hz.

Fig. 5.10 shows the results for the absolute maximum percentage of reflections in forces for all three configurations. Fig. 5.10 (a) shows that at lower frequencies all the methods ALID, ALID+ABC, and ALID+VABC are producing more reflections than design frequencies. For higher frequencies, there is no significant change in case of ALID, but ALID+VABC performed very well. The results are plotted on a logarithmic scale in Fig. 5.10 (b) to magnify the results for the proposed method at higher frequencies, where the reflections are much

reduced. The performance is slowly reducing at very high frequencies for ALID+VABC. This suggests that at very high loading frequencies compared with the designed load frequencies, the performance with the ALID+VABC boundary condition is slowly degrading. The reason for the degradation in performance is due to the fact that the VABC boundary conditions are using a first-order approximation in the Taylor series.

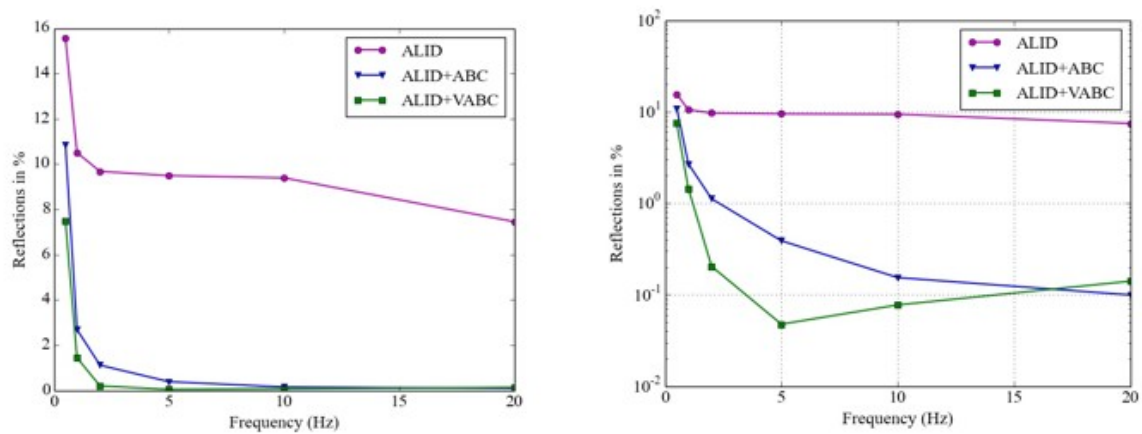


Figure 5.10. Percentage of reflection vs load frequency

5.3.2. 2D scalar P-wave propagation

In this section, the efficiency of the proposed radiating boundary conditions is evaluated in terms of two-dimensional scalar wave propagation. In this model setup, the waves impinge on the boundary in the normal direction, but radiation damping is present in the model as the waves move away from the boundary. Therefore, the major goal of this section is to present the effect of radiation damping on the boundary condition.

A pure P-wave propagation is applied which is resulting from the explosive source in the infinite medium under plane strain condition as described in Fig. 5.11. The medium has an elastic P-wave velocity $V_p = 2$ m/sec and density $\rho = 1800$ kg/m³. The wave's travel time from the source field to the boundary is approximately 1.5 seconds and the simulation duration is 6 seconds. Due to the symmetry of the domain, only one-fourth of the domain is considered in the modelling, and AoS is 4λ i.e., 4.0 m radius. Analysis has been carried out for three configurations, as discussed in previous sections. Absorbing region length is considered as 1.5λ , and absorbing boundary conditions are applied normal to the boundary as shown in Fig. 5.11. Numerical analysis is carried out using the modified central difference scheme in LsDyna, where the velocities are computed half a timestep behind.

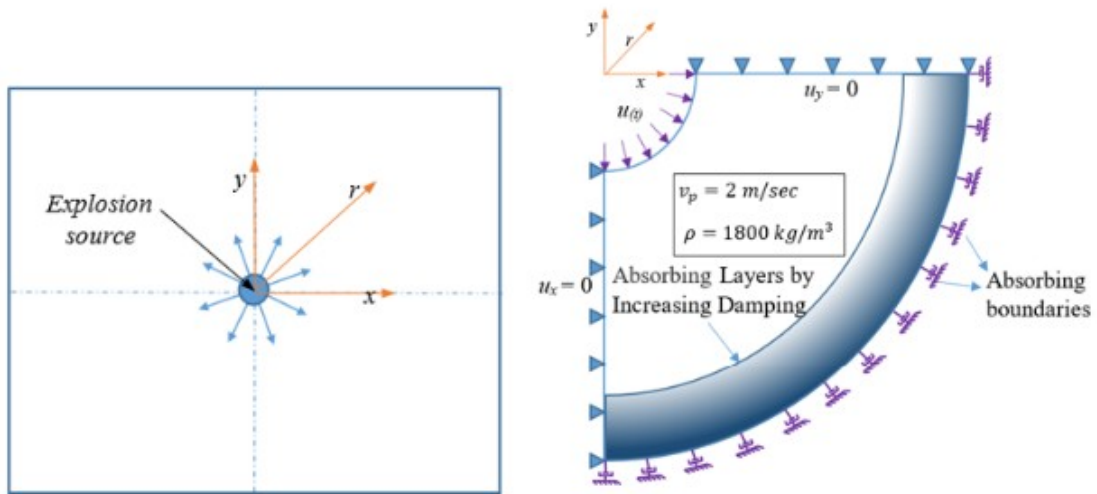


Figure 5.11. 2D Plane strain model for pure P-Wave propagation

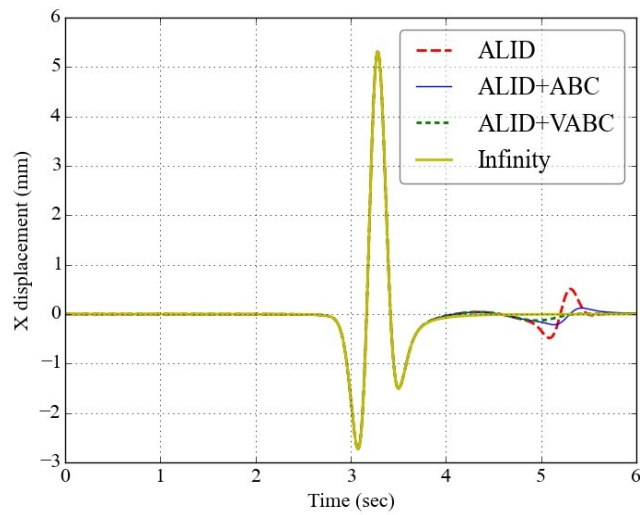


Figure 5.12. Displacements at 3.50 m radius

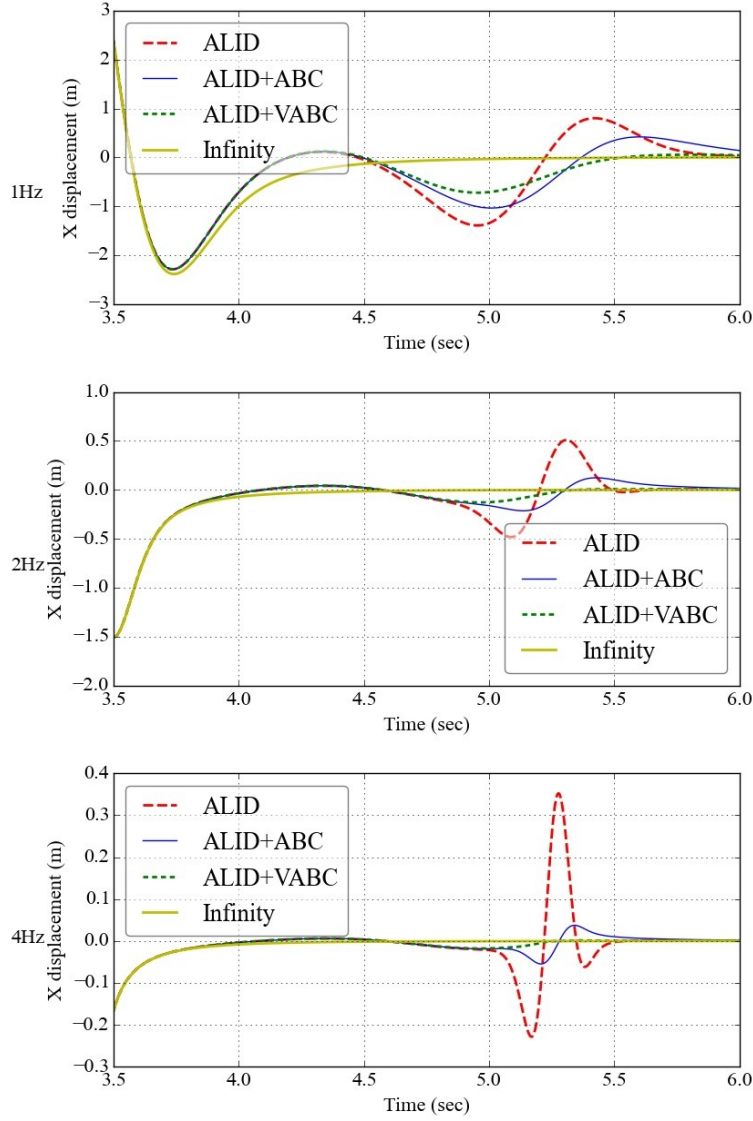


Figure 5.13. Displacements vs load frequency at 3.50m radius

The time variation of the displacement at the explosion source is considered using a Ricker wavelet as defined in equation 5.3. The parameters used in this problem are $A_f = 10$ mm, $f_p = 2$ Hz and $t_s = 1.5$ sec. A 1.0 m radius cavity is created around the source to apply the pressure wave and avoid numerical instabilities due to meshing near the origin. To obtain the appropriate source field for use in the numerical method, analytical simulation of the infinite media is carried out using equation 5.4.

$$u(r, t) = \frac{1}{2\pi} \int_{-\infty}^{\infty} \left[-i\pi H_0^{(2)}(k * r) F_{\omega} \right] e^{+i\omega t} d\omega \quad (5.4)$$

Where, r is the radial distance from the source, F_{ω} is fourier transform of Ricker wavelet defined in equation 5.3, ω is the frequency, $k = \frac{\omega}{V_p}$ is the wave number. The inverse Fourier transform in equation 5.4 is performed numerically.

The displacements in the model at 3.5 m radius are as shown in Fig. 5.12. The percentages of reflections are about 10%, 4%, and 3% for ALID, ALID+ABC, and ALID+VABC cases, respectively. The percentages of reflections presented in Fig. 5.9 for the 1D wave propagation problem are 10%, 3%, and 1.5% for ALID, ALID+ABC, and ALID+VABC, respectively, where the original central difference scheme is used. The percentage of reflections is the same for ALID, but ALID+ABC and ALID+VABC are higher in cases of 2D scalar wave propagation where LsDyna is used. This concludes that the efficiency is slightly compromised when using the commercial software as the software uses velocities computed at the middle of timesteps.

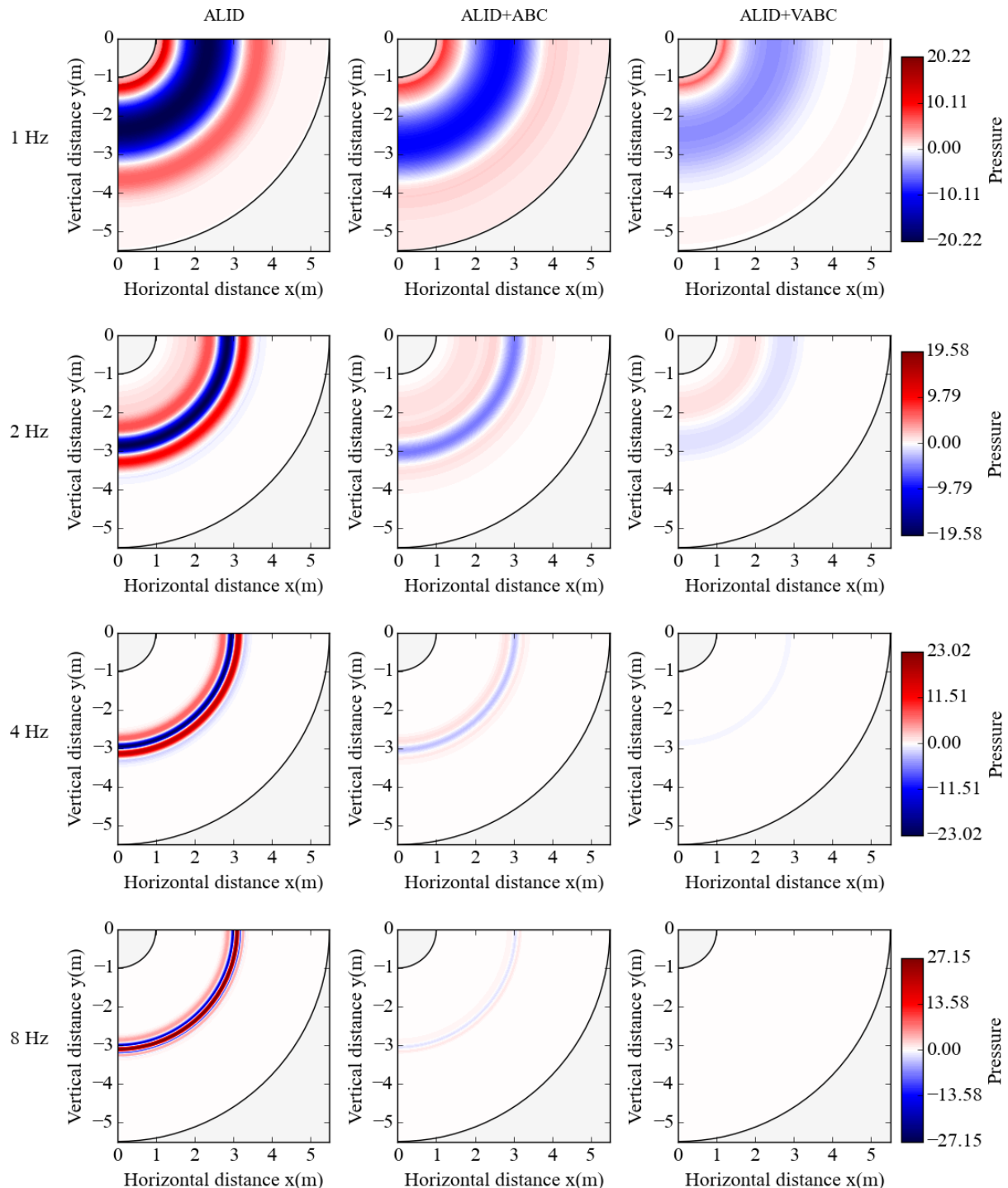


Figure 5.14. Snapshot of pressure distribution (N/m^2) at time $t = 5.5$ sec

A sensitivity analysis was carried out to test the validity of the proposed method for different loading frequencies. Radial displacements due to reflections are shown in Fig. 5.13. The displacements in all configurations increased when the loading frequency decreased, and vice versa. However, the reflections are largely reduced for ALID+ABC and ALID+VABC configurations at higher frequencies. The same observations are noted in one-dimensional wave propagation configurations.

Fig. 5.14 shows the pressure distribution contour plot at 5.5 seconds for three configurations. Again, similar observations are noted. The reflections for ALID+ABC and ALID+VABC configurations are negligible at frequencies higher than the designed frequency, and the reflections are increased at lower frequencies due to the increase in impedance mismatch between the successive layers of elements.

The absolute maximum percentage of error or percentage of reflection is calculated for different loading frequencies. Fig. 5.15 shows the percentage of reflections for loading frequencies ranging from 1 Hz to 10 Hz when the model is created for a 2 Hz designed loading frequency. It is noted again that the reflections in ALID+VABC reduces to less than 0.1% for 7Hz and above frequencies and increase to 10% for 1Hz loading frequency.

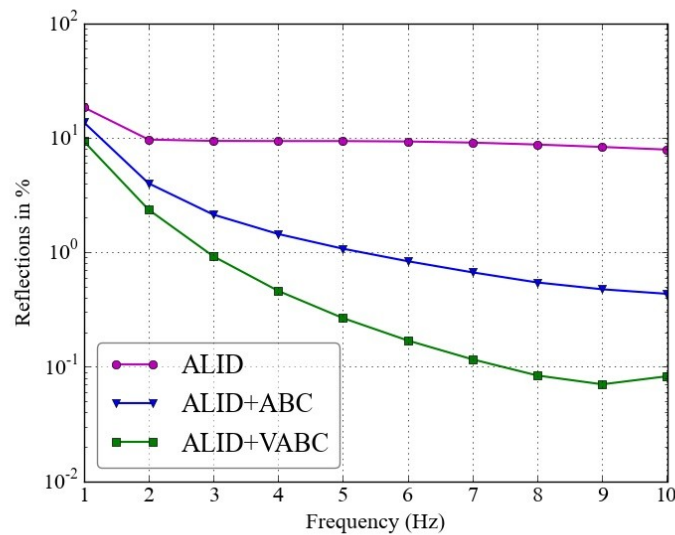


Figure 5.15. Percentage of reflection vs load frequency for 2D scalar wave propagation

5.3.3. 2D wave propagation:

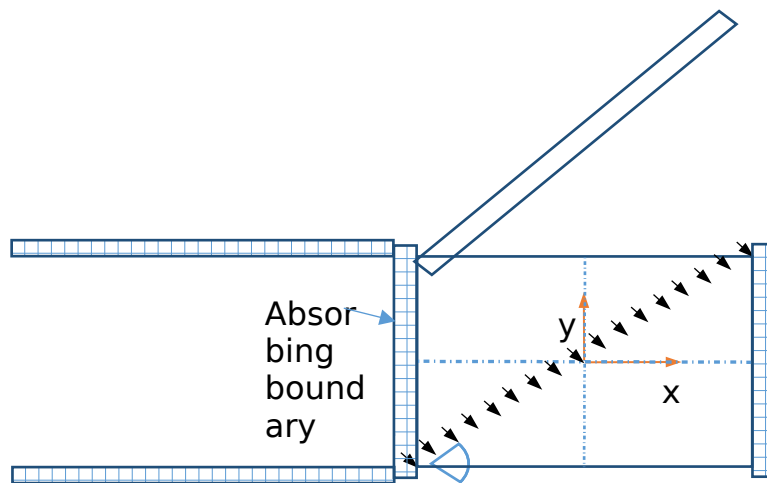


Figure 5.16: 2D plane strain model for wave propagation in an infinite domain

In this section, a two-dimensional elastic wave propagation within an infinite domain in plane strain condition is analysed, as shown in Fig. 5.16. The medium has Young's Modulus of $9.0 \times 10^6 \text{ N/m}^2$, density $\rho = 1800 \text{ kg/m}^3$, P-wave velocity $v_p = 100 \text{ m/sec}$ and S-wave velocity $v_s = 50 \text{ m/sec}$. The model dimension for AoS is chosen as 200 m by 200 m. Analysis was carried out for 5 seconds and included three configurations a). ALID, b). ALID+VABC, and c). SRM method. The absorbing region was designed with 30 elements, and the results analysed for 1 m, 2 m and 3 m element lengths. The domain was subjected to a pressure wave of Ricker wavelets along the loading line, as shown in Fig. 5.16. The wavelet parameters are $A_f = 1 \text{ N}$, $f_p = 1 \text{ Hz}$, and $t_s = 2.0 \text{ sec}$.

Fig. 5.17 shows the pressure distribution at 2.3 seconds. The image shows that there are reflections from the boundary in the case of an SRM configuration when the element length is 1 m. All the configurations look performing well when the element length is 3m but there exist numerical oscillations inside the domain. It is difficult to measure the p-wave and s-wave reflections from the incident p-wave or s-wave from the displacements and contour plot.

To analyse the efficiency of the proposed method at various incident angles, a spatial FFT is carried out. A plane strain model, as shown in Fig. 5.18, is analysed. The medium has Young's Modulus of $9.0 \times 10^6 \text{ N/m}^2$, density $\rho = 1800 \text{ kg/m}^3$, P-wave velocity, $v_p = 100 \text{ m/sec}$ and S-wave velocity, $v_s = 50 \text{ m/sec}$. The model dimension for AoS is chosen was 200 m by 200 m, and the analysis was carried out for 8 seconds. ALID, SRM and ALID+VABC boundary conditions are applied at the bottom side with 30 elements with absorbing region length 1.5λ and Ultra ALID is provided on all other sides with 150 elements. P- and S-waves of frequency 1 Hz are applied along the loading line. The reflection coefficients for variation incident P- and S-waves are shown in Fig. 5.19. The results show that SRM performs slightly better than the proposed method, but both methods outperform ALID for all incident angles.

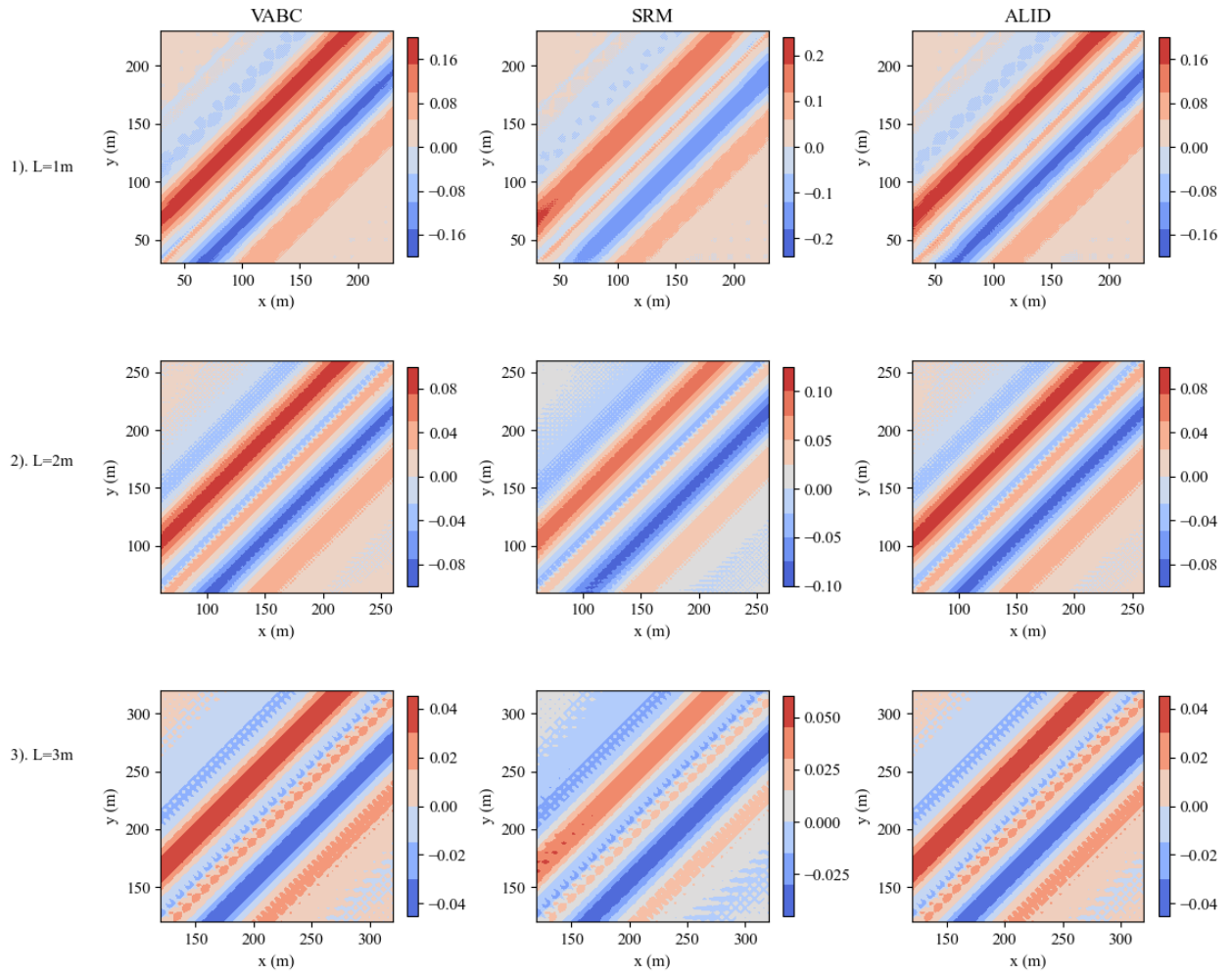


Figure 5.17: Snapshot of Pressure distribution (N/m²) @2.38 sec

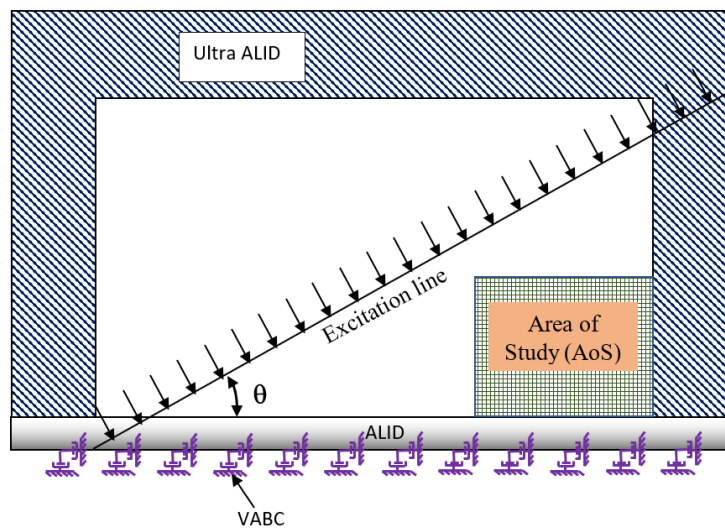


Figure 5.18: 2D plane strain model for wave propagation in an infinite domain

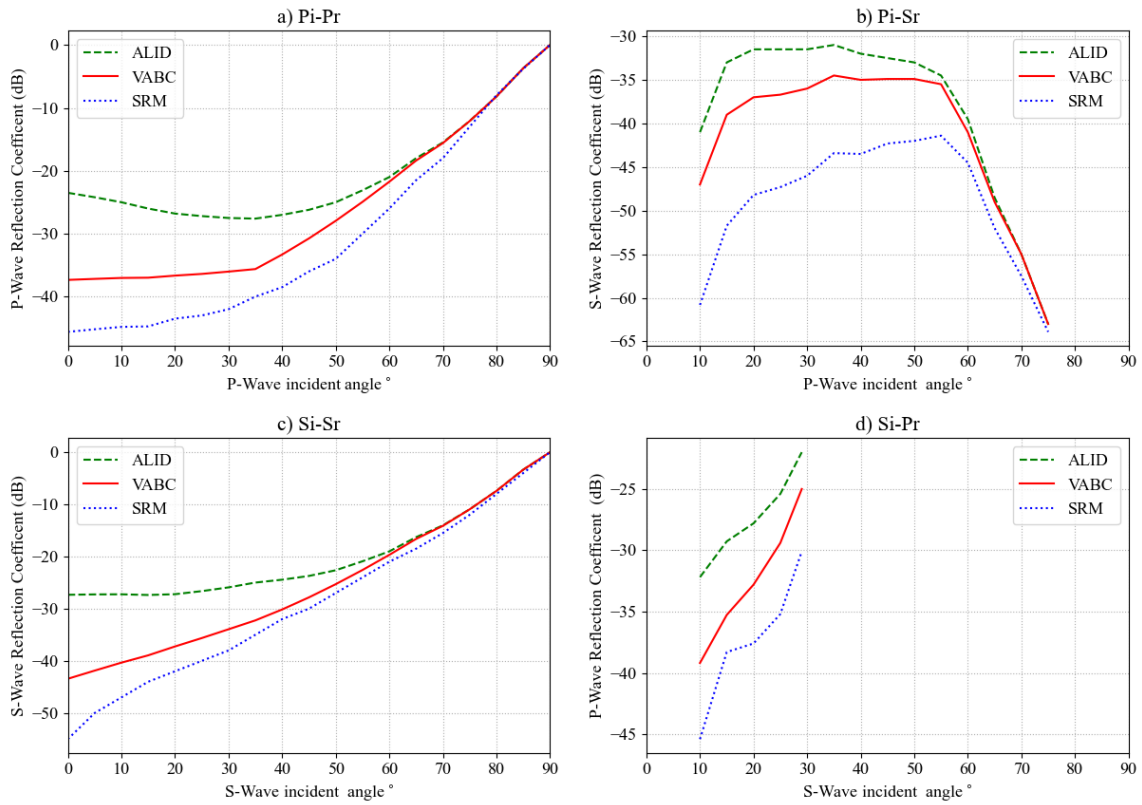


Figure 5.19: Reflection coefficients for ALID, VABC and SRM

5.4. Conclusions:

A method for radiating boundary conditions is presented by combining the absorbing layers and absorbing boundary conditions for viscoelastic wave propagation. The additional cost of adding the local absorbing boundaries to ALID is very little, but the efficiency is improved many folds. The performance of ALID is poor when the absorbing region length is 1.5λ , which produces nearly 5% reflections, and the percentage of reflections increases to more than 50% if the absorbing region length is 0.33λ , even when the wave is propagating in the normal direction to the boundary. SRM approach works best when the absorbing region length is 1.5λ , but performs poor when the absorbing region length is less than λ . These two methods require many layers, especially if the mesh size in the domain is small. The present method overcomes this difficulty and performs well when the absorbing region length is 0.5λ or more.

The performance of all the methods, ALID, SRM, and ALID+VABC, degrades if the numerical model is subjected to a lower frequency than the designed frequency but performs excellently at higher incident frequencies.

The proposed approach uses features that are readily available in many commercial programs, such as LsDyna and Oasys GSA used in this investigation, but the novel feature here is assigning the correct setup and damping properties. The efficiency is slightly compromised when using the commercial software, as the software uses velocities computed at the middle of timesteps.

6. Numerical modelling of Soil-Structure-Interaction for Tall Building

6.1 Introduction

The soil-structure interaction analysis evaluates the collective response of the three linked systems: the structure, the foundation, and the soil media surrounding the foundation. The soil medium needs to extend to a specified distance to get free-field ground motion, i.e., the response in the soil medium should not be affected by structural vibrations or the scattering of waves from the structure and the foundation. The resulting FE model will be huge to model the soil medium and obtain free-field motion at the boundary. An alternative to modelling the soil media to get the free-field motion is to provide a radiating boundary condition where all the radiating waves from the structure and foundation are damped. Therefore, an accurate nonlinear soil-structure interaction of tall buildings using finite element analysis must consider the effects of the radiation damping. Chapter 2 provided a detailed review of various radiating boundary conditions available in the literature. Chapter 5 provides an efficient radiating boundary condition by combining the absorbing layers with local absorbing boundaries (ALID+VABC). In this chapter, the ALID+VABC boundary conditions are verified with a numerical analysis of tall buildings, which includes the nonlinear soil-structure interaction effects.

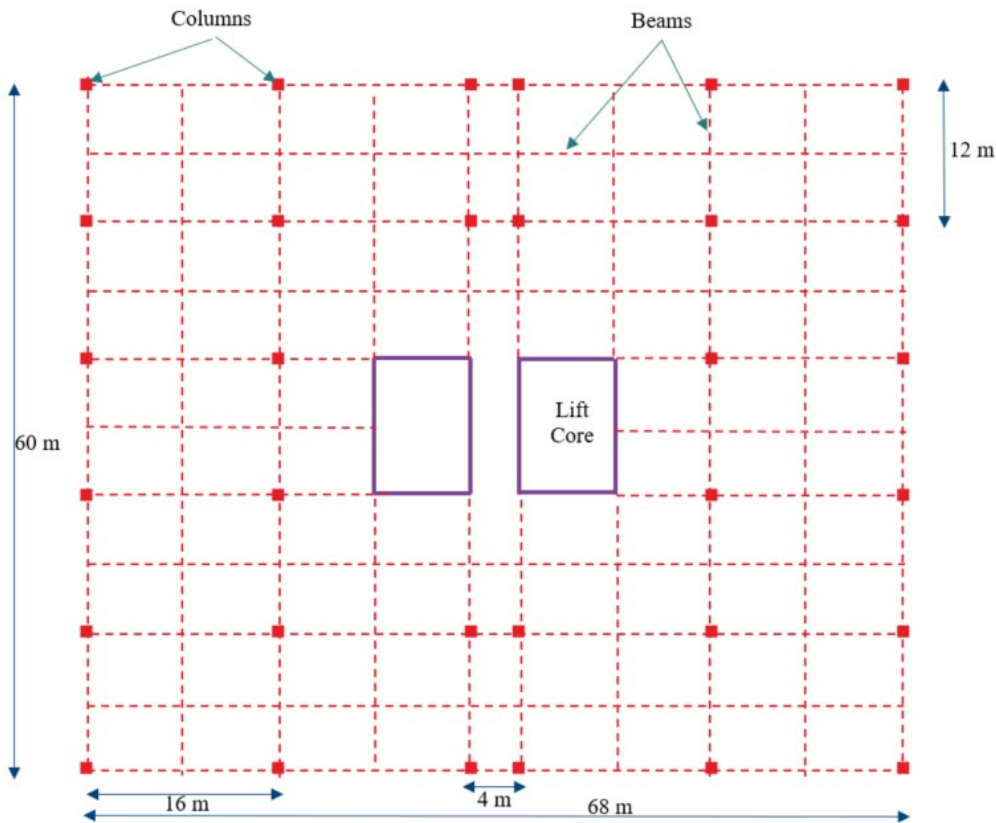


Figure 6.1: Plan view of Finite Element Model Superstructure

6.2 Model details:

A dynamic nonlinear SSI analysis of 3D tall building is carried out. The model chosen is symmetric in both the x and y directions and in the plan view of the superstructure, as shown in Fig. 6.1. The seismic loading is applied along the minor axis, i.e., along the y axis, and hence only half of the model is created for numerical analysis.

Table 6.1: Material Properties

	Concrete Linear Elastic	Soil Mohr-Coulomb
Young's Modulus (E)	3e10 MPa	
Shear Modulus (G)		40.5e6 MPa
Poisson's Ratio (ν)	0.2	0.3
Density (ρ)	2400 Kg/m ³	1800 Kg/m ³
Cohesion (c)		5 MPa
Friction Angle (ϕ) coefficient		0.35
Dilation Angle (φ) coefficient		0.35

The full soil-structure-interaction numerical model, including soil, foundation, substructure, and superstructure (beams and columns), is shown in Fig. 6.2. All structural elements, including beams, columns, shear walls, piles, and raft are modelled as linear elastic elements using M35 grade concrete, and the soil is modelled using Mohr-Coulomb materials. The details of the materials are shown in Table 6.1.

6.2.1 Superstructure:

The superstructure is modelled with G+18 floors, and all superstructural elements were modelled as RCC linear elastic elements. The size of the beams is taken 300mm x 600mm in all floors including in substructure and modelled using 2-node beam elements. The slabs are 150mm thick and modelled using 4-node shell elements. The column sizes are varying, as shown in table 6.2.

Table 6.2: Details of columns

Floor Level	Size (mm)
Basement Level 2 to Floor 6	900 x 900
Floor 7 to 10	800x800
Floor 10 to 14	600x600
Floor 15 to 18	450x450

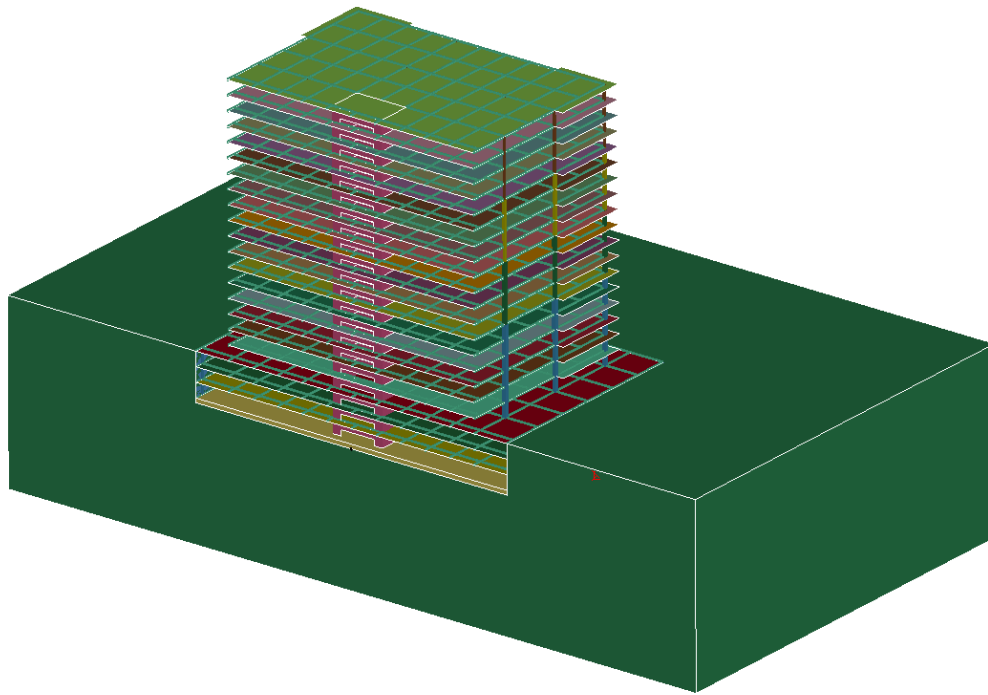


Figure 6.2: Full soil structure interaction model

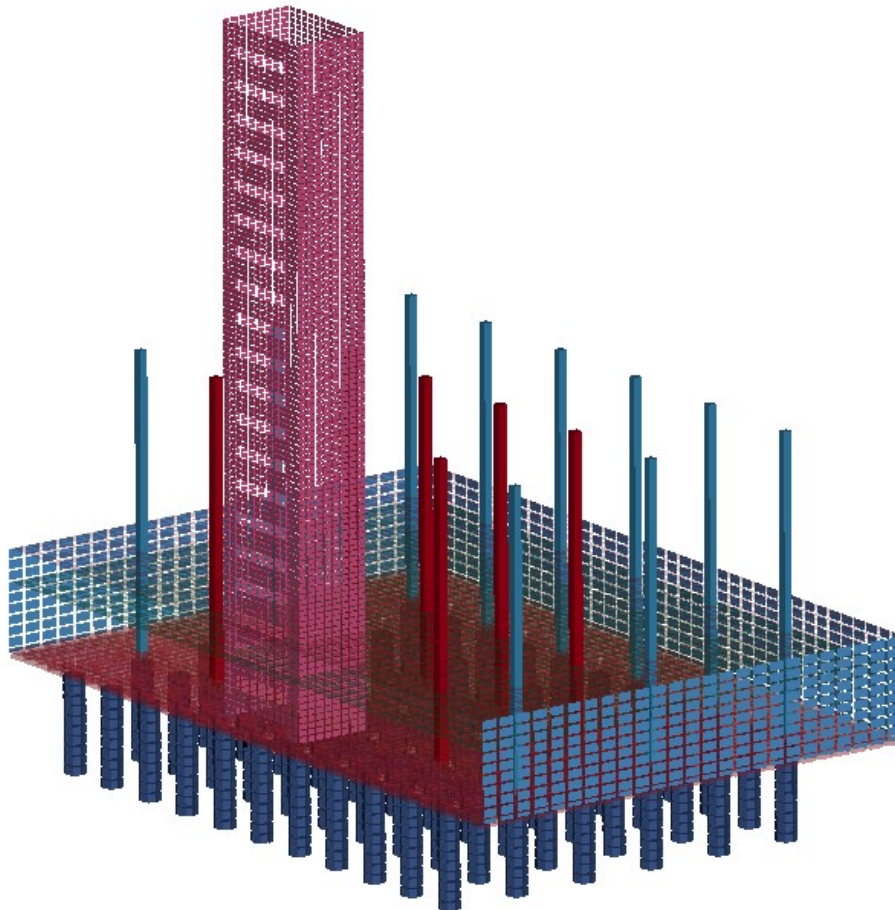


Figure 6.3: Substructure and Foundation system

6.2.2 Substructure and Foundation:

The substructure with the foundation numerical model is shown in Fig. 6.3. The substructure consists of a cellar and two basement floors. The details of the structural element are given in Section 6.2.1. The foundation is built using piles and rafts. Piles are modelled using the 3D 8-node brick elements, and rafts and retaining walls are modelled using shell elements.

6.2.3 Soil Modelling and interface Modelling:

Soil is modelling using 8-Node brick elements as shown in Fig 6.4. Contact interfaces between a). soil and pile, b). soil and raft, and c). soil and retaining wall are modelled using a coulomb-friction contact interface with 0.3 as the internal friction angle coefficient.

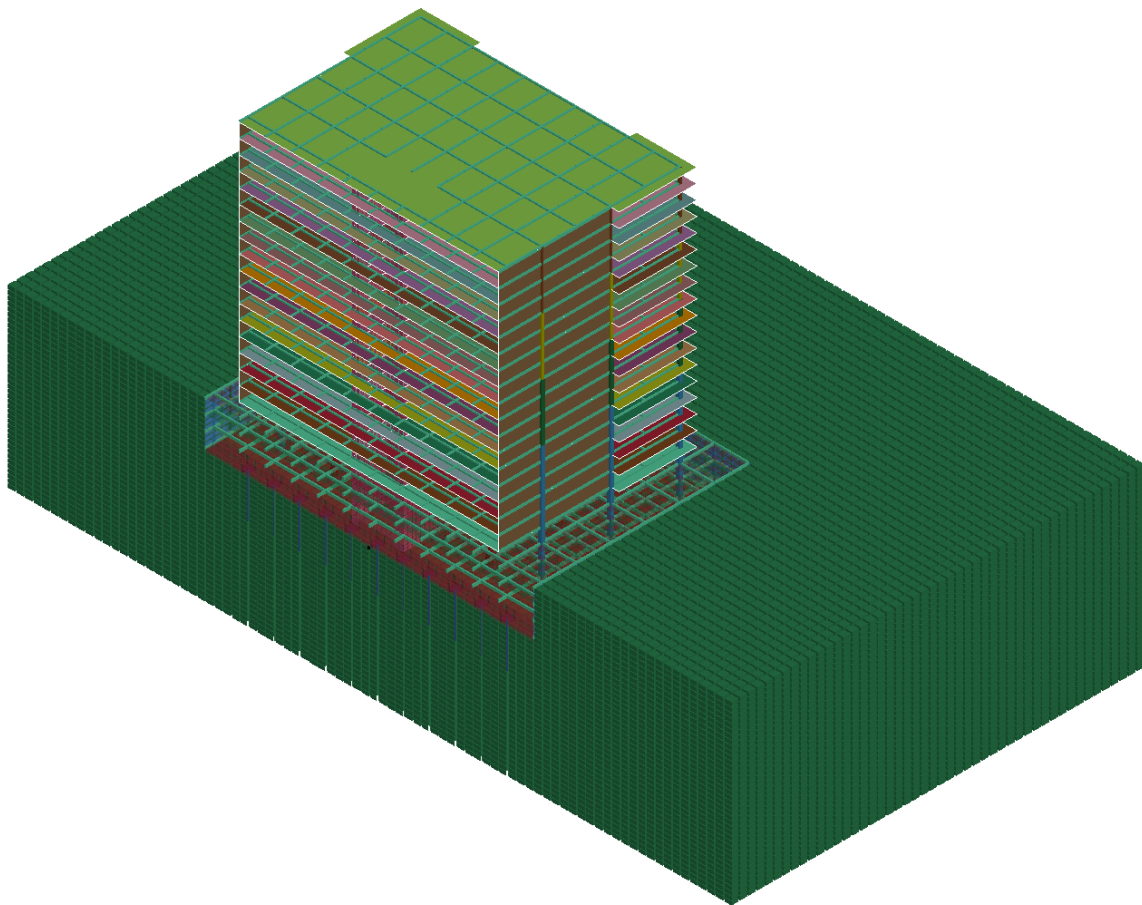


Figure 6.4: 3D Numerical Modelling of Soil

6.3 Numerical analysis:

Numerical analysis is carried out on the models created using three types of radiating boundary conditions: a). ABC, b). ALID, and c). ALID+ABC. SRM has been excluded from the study since the absorbing region length for 30 elements is only 0.33λ and the SRM method needs an absorbing region of length at least equal to the wavelength λ as discussed in

Section 5.3.1.1. The analysis is carried out on the model in two steps. First, a static analysis is carried out on the models, and then a nonlinear dynamic analysis is carried out using the EL Centro earthquake. The maximum amplitude loading frequencies are in the range of 0–2 Hz for the EL Centro earthquake, and 1 Hz is chosen as the predominant loading frequency for designing the absorbing layers. The optimum damping parameters are defined in Chapter 6 for providing the absorbing layers.

The Domain Reduction Method (DRM) is used to apply the earthquake loading to carry out the dynamic analysis. Figure 6.5 shows the interface boundary layer where seismic loading is applied. Appropriate radiating boundary conditions are applied after the interface layer to damp out the reflected waves from the structure. One layer of elements is provided for ABC configuration, and at the end of that layer, dashpots are provided around the last layer of nodes. For ALID and ALID+VABC, 30 layers of elements are provided after the interface layer with an increase in damping as discussed in the previous chapter.

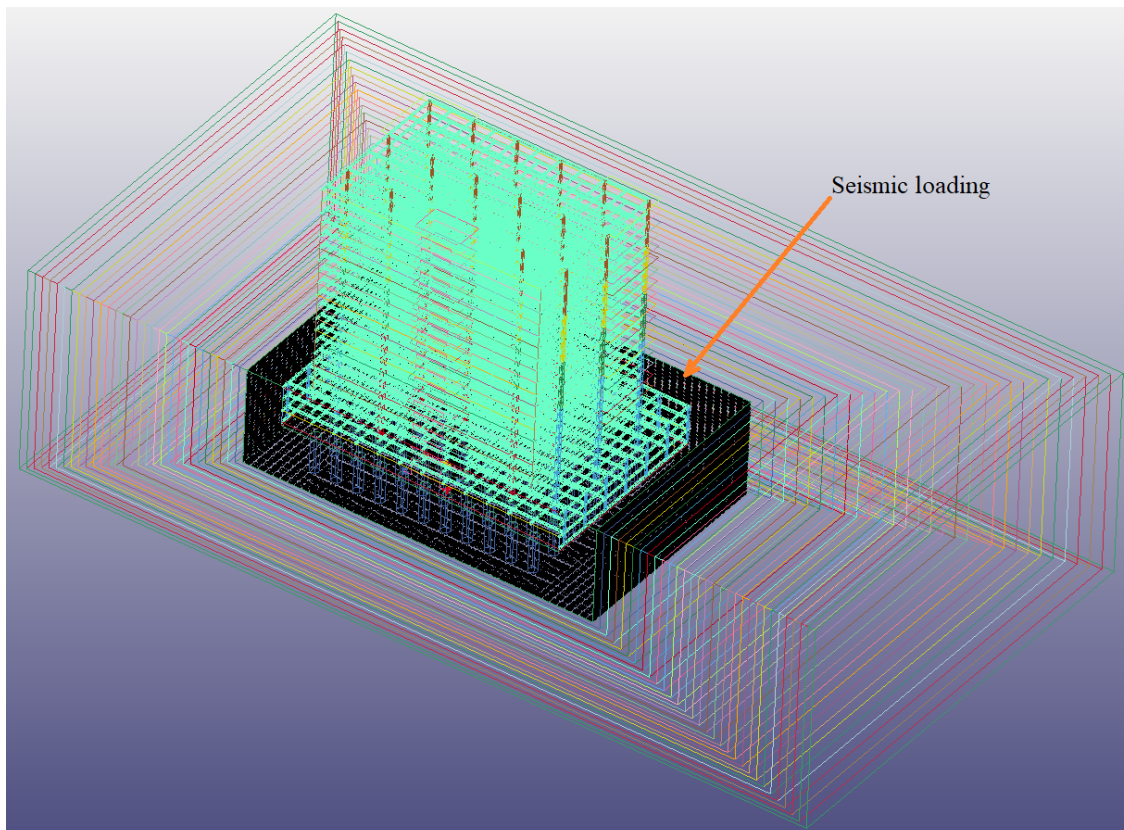


Figure 6.5: Interface boundary layer for seismic loading using DRM approach

First, 1D wave propagation is carried out assuming wave propagation originates from bedrock, which is assumed to be located far away from the ground surface, i.e., 1.5 KM below the ground surface. The forces from the 1D wave propagation at the chosen boundary layer location are captured and applied in 3D wave propagation. Figure 6.6 shows the acceleration time history applied at the boundary layer.

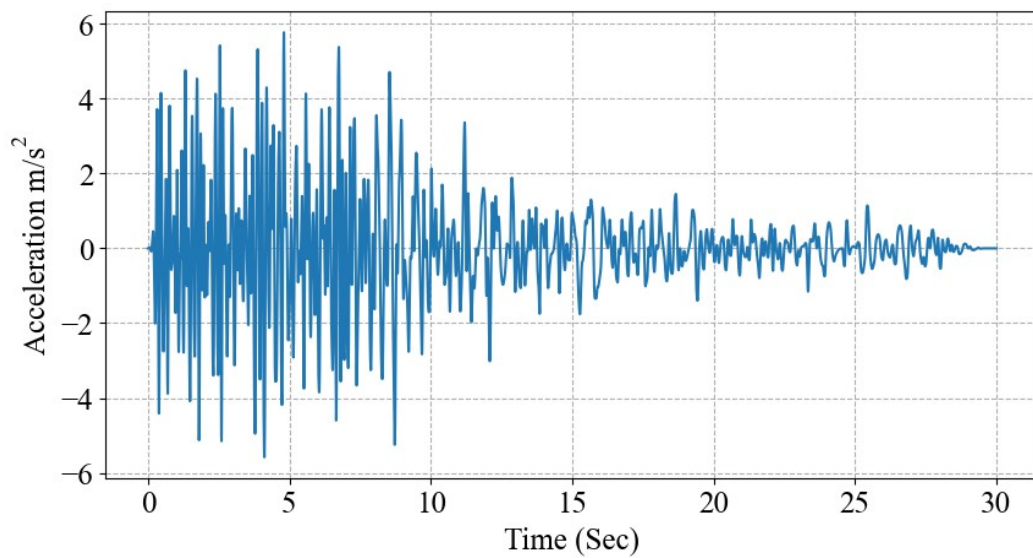
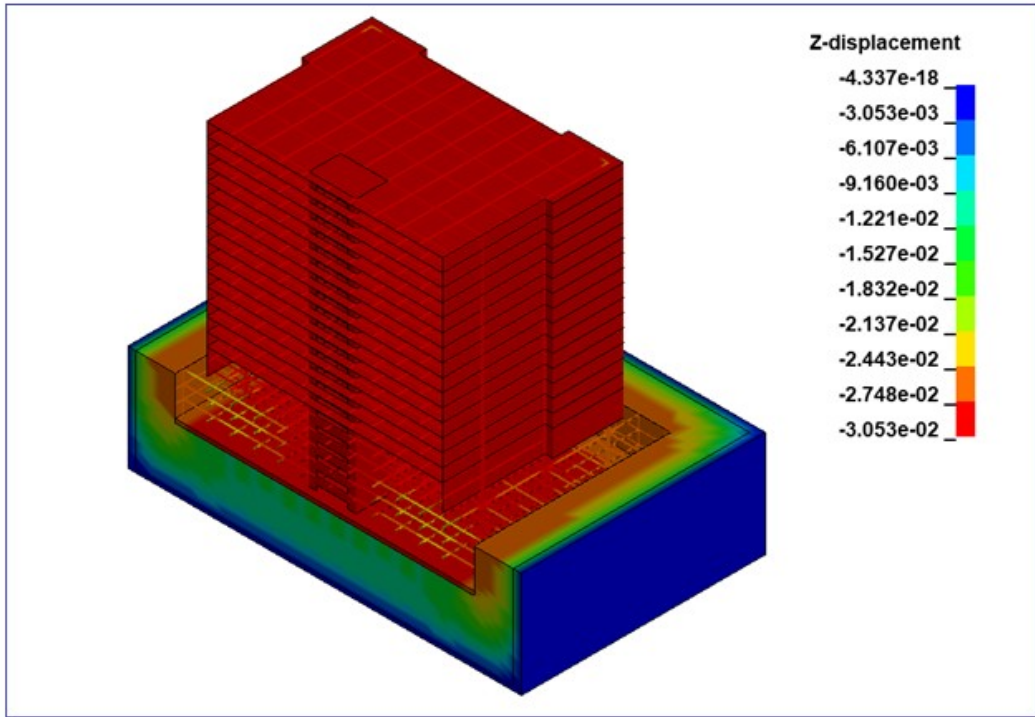


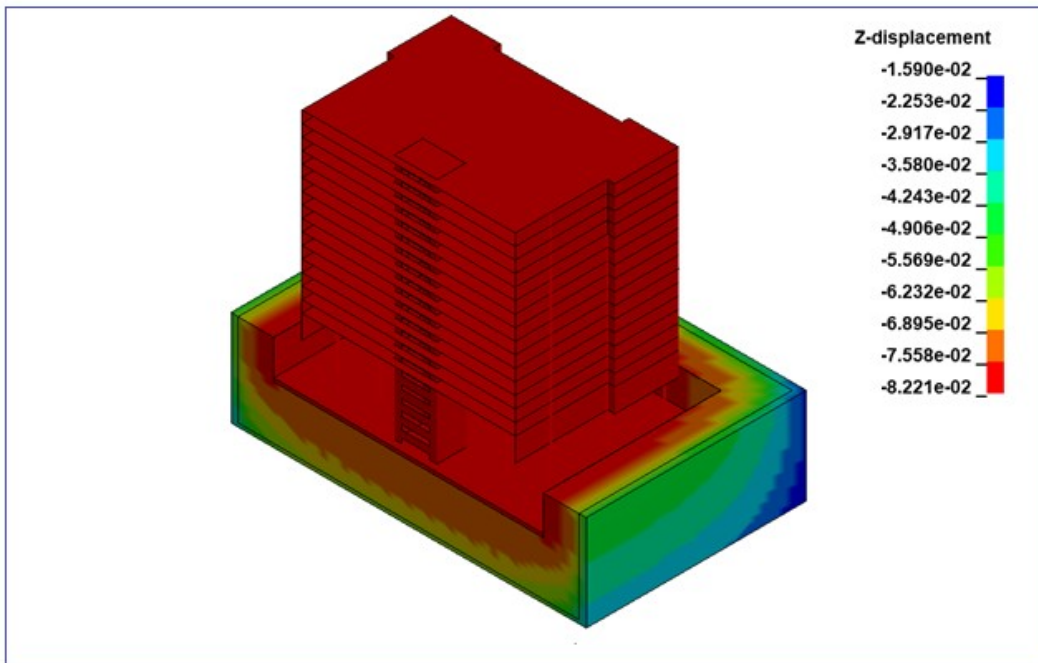
Figure 6.6: Acceleration Time History applied at the interface layer

6.3.1 Static analysis

The static analysis is carried out using gravitational loading. The static analysis is carried out in two stages. Stage 1 consists of self-weight analysis piles and rafts, and stage 2 gravitational loading of the entire model is included. The numerical models in the analysis include the absorbing layers in the 2nd and 3rd configurations, i.e., ALID and ALID+VABC.

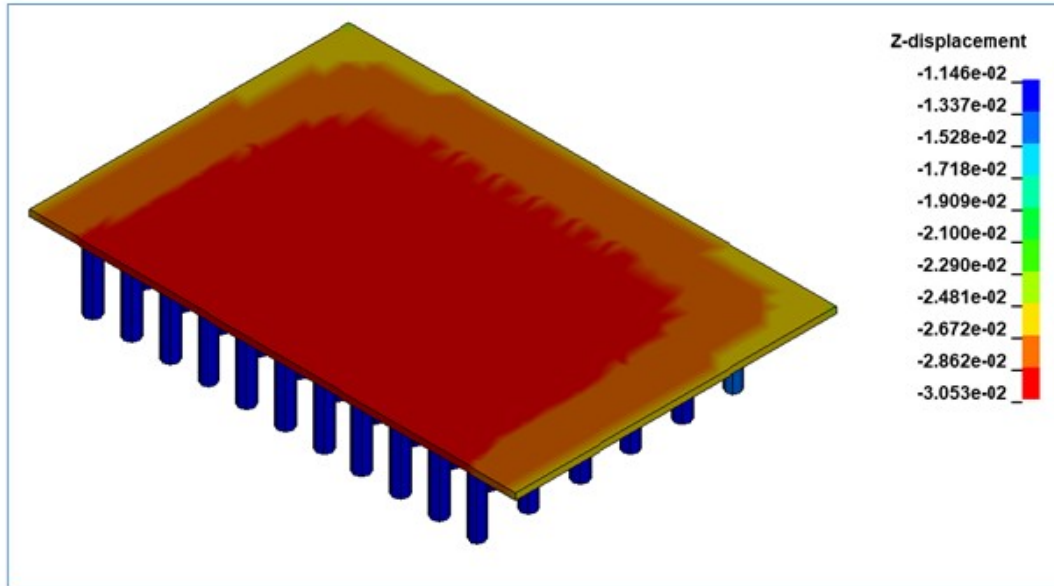


a). Vertical displacement in ABC configuration

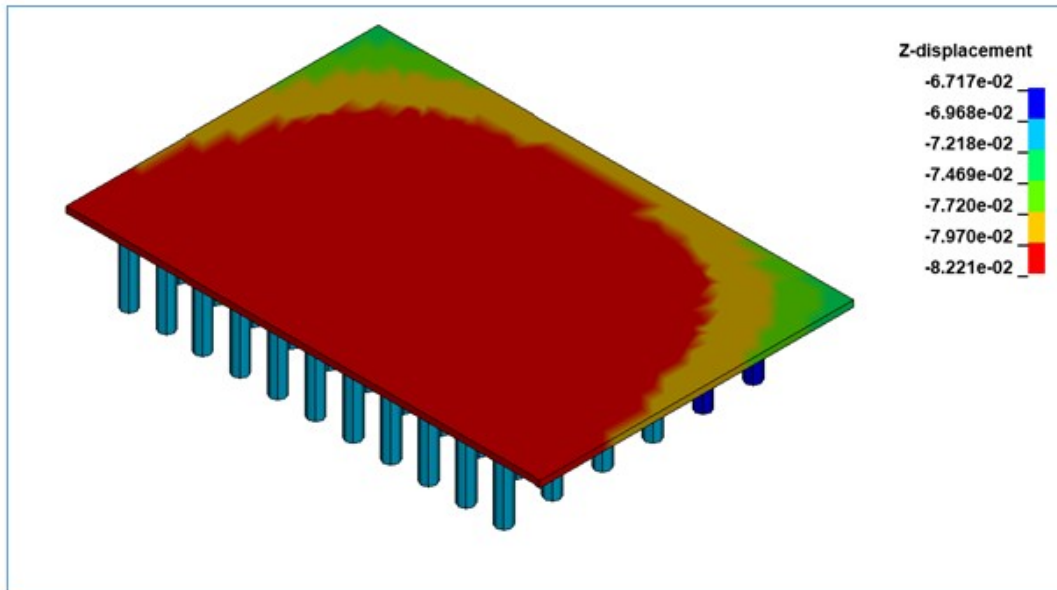


b). Vertical displacement in ALID and ALID+VABC configuration

Figure 6.7: z-displacements (m) under self-weight a). ABC b) ALID and ALID+VABC



a). Vertical displacement in ABC configuration



b). Vertical displacement in ALID and ALID+VABC configuration

Figure 6.8: z-displacements (m) at raft level under self-weight a). ABC b) ALID and ALID+VABC

Vertical displacements in the model from static analysis are shown in Fig. 6.7 for all configurations. Maximum displacements at the top of the structure in cases ABC and ALID+VABC are observed at 30.533mm and 82.214mm, respectively. Fig. 6.8 shows the maximum displacements at raft level, and the same are observed as 30.526 mm and 82.217 mm for ABC and ALID+VABC configurations, respectively. The displacements in the structures are calculated at 0.007 mm in all configurations, which is negligible under the self-weight of the structure. The main difference in the displacement is in modelling the soil domain and the boundary conditions. In the case of ALID and ALID+VABC, the additional layers allow the soil to move both horizontally and vertically when compared to the ABC alone. This shows that the absorbing layers can be considered as part of the soil model to

include the effect of pressure distribution in addition to the original purpose, i.e., absorbing the wave propagation.

6.3.2 Dynamic Analysis

A nonlinear dynamic analysis is carried out using an explicit central difference scheme using LsDyna for ABC, ALID, and ALID+ABC radiating boundary conditions. El Centro earthquake motion obtained using 1D wave propagation, as shown in Fig. 6.6, is applied at the SSI interface after the static analysis is completed. Models are analysed for 30 seconds, and results are evaluated for verification.

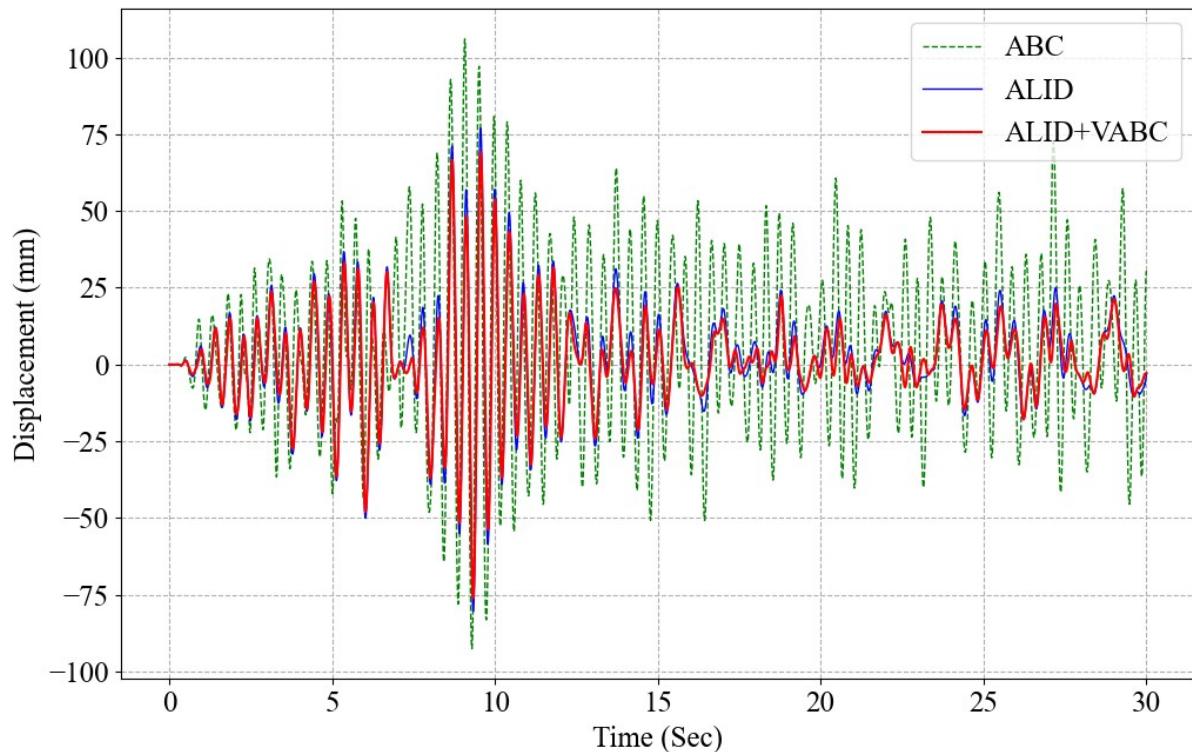


Figure 6.9: Displacement time history at the top centre of the building

The time history of displacements at the top centre of the building is shown in Fig. 6.9. From the results, it is noted that the maximum displacements for ABC, ALID, and ALID+VABC are 106 mm, 80.2 mm, and 76 mm, respectively. The maximum displacements are observed for ABC, ALID, and ALID+VABC at 8.8, 8.94, and 8.95 seconds, respectively. The reason for the delay in peak response in the case of ALID and ALID+VABC may be due to an increase in flexibility with additional absorbing layers. The increase in flexibility may vary depending on the amount of soil domain, but the present study does not take this parameter into account.

The displacement time history for the pile head is shown in Fig. 6.10. The maximum displacements for ABC, ALID, and ALID+VABC are 92.0 mm, 34.25 mm, and 30.29 mm, respectively. The difference in the displacements at pile heads and the top of the structure is higher in case ALID. The reason for the small difference at the top of the structure compared to a pile top is that the interference of the reflected waves is higher for the ABC model. Storey displacement and inter-storey drifts are shown in Figs. 6.11 and 6.12. Similar

observations are made, i.e., ALID+VABC performs better than ABC and ALID configurations.

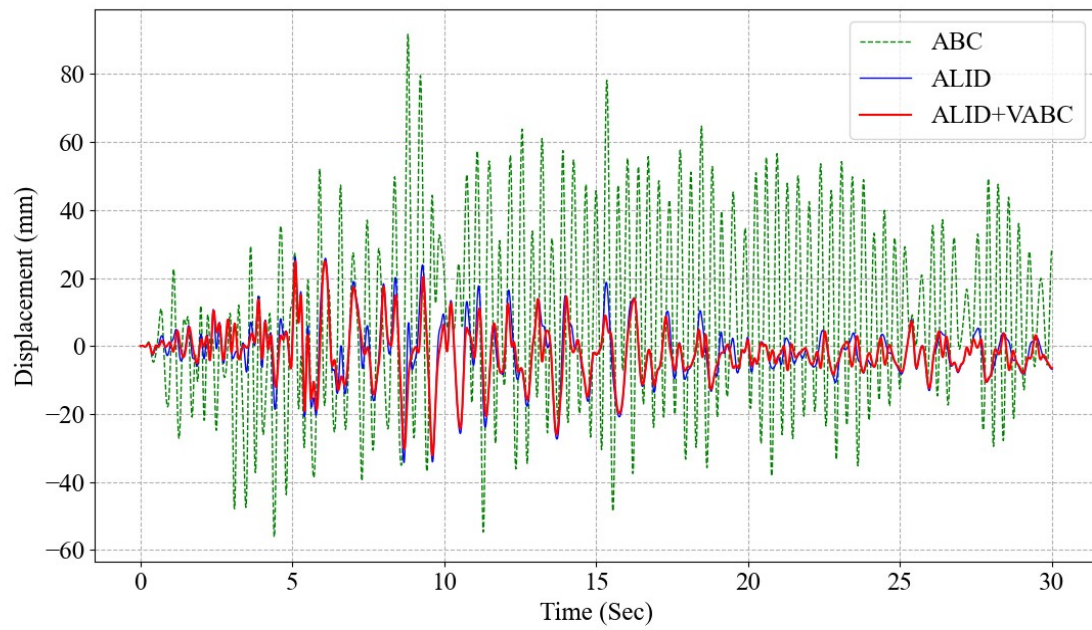
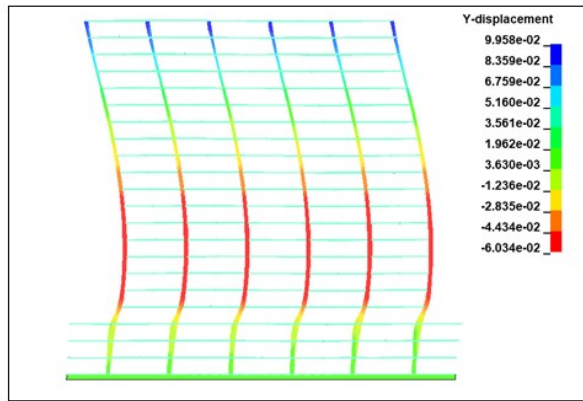
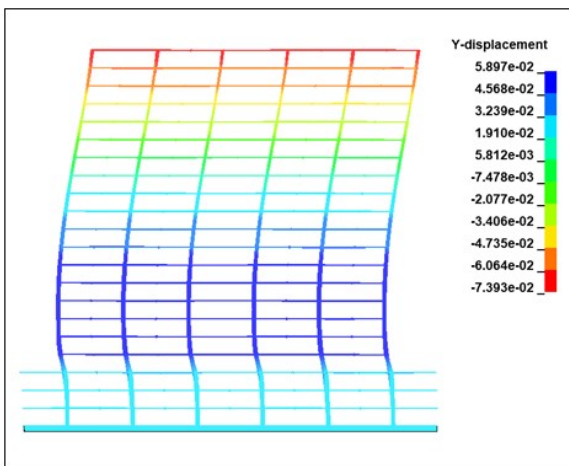


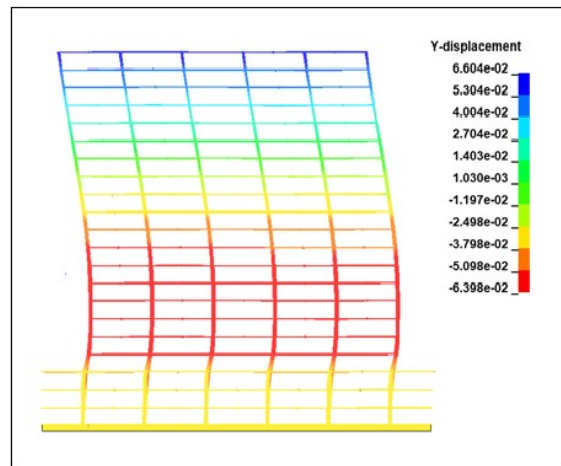
Figure 6.10: Displacement time history at the Pile Top near the centre of the building



a). Story displacement contour in ABC configuration



b). Story displacement contour in ALID configuration



c). Story displacement contour in ALID+VABC configuration

Figure 6.11: Storey displacement contour in ABC, ALID and ALID+VABC configurations

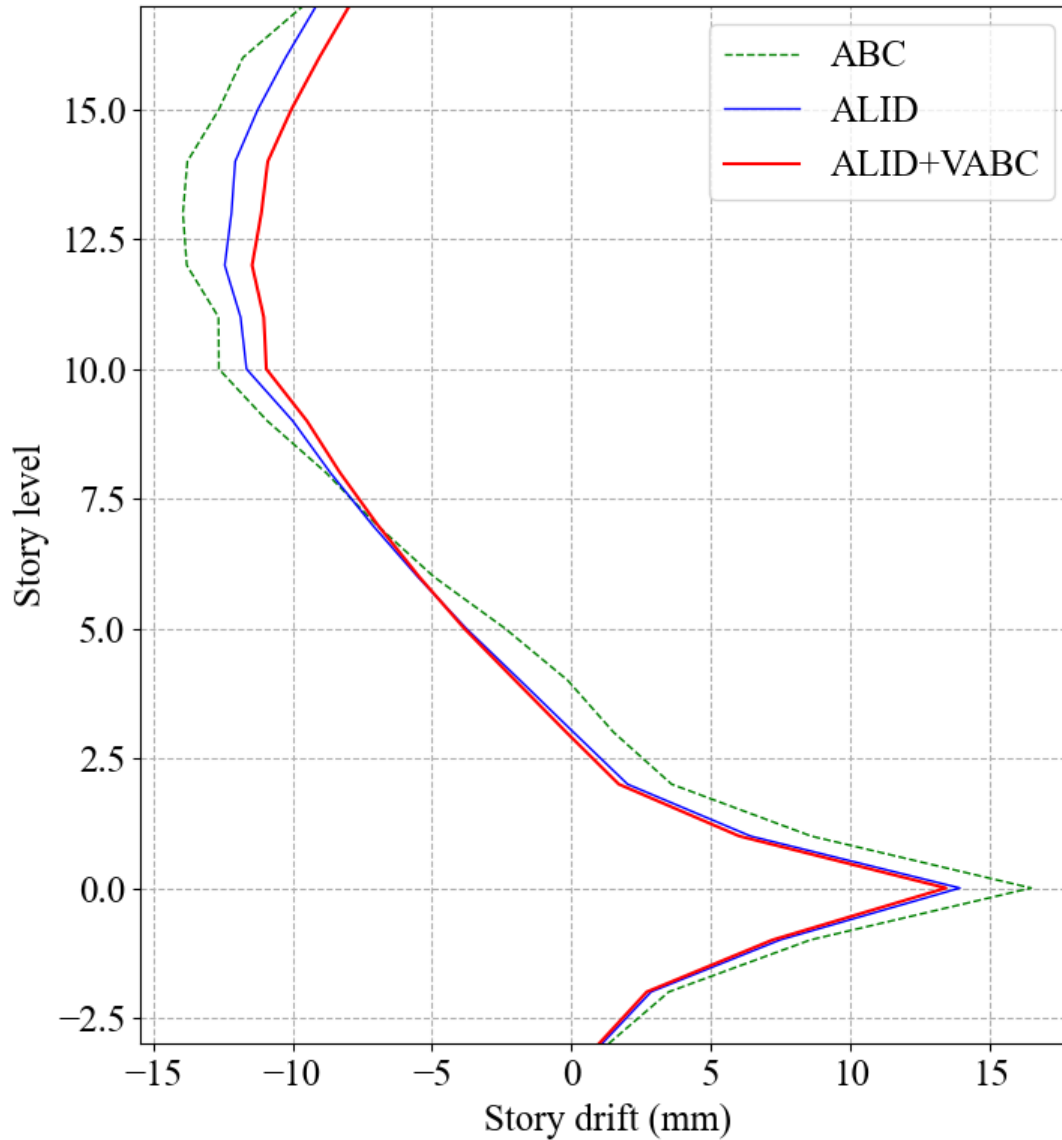


Figure 6.12: Storey drift in ABC, ALID and ALID+VABC configurations

6.4. Conclusions

A soil-structure-interaction analysis is carried out on a tall building with a G+18 along with a cellar and two basement floors. Both static and dynamic analysis are carried out in a staged manner. Three types of radiating boundary conditions were presented. 1). ABC, 2) ALID and 3). ALID + VABC. SRM has been excluded from the study since the absorbing region length for 30 elements is only 0.33λ for which SRM does not perform well, as shown in Section 5.3.1.1. The absorbing layers in ALID and ALID+VABC were also present in the static analysis since the damping properties did not influence the analysis.

Static analysis results were presented. The results show that the model with absorbing layers, i.e., ALID and ALID+VABC, produces more displacements compared to ABC since the finite elements in the absorbing layers are subjected to gravitational loads from above. This

proves that the absorbing layers can be used to reduce the actual model domain if they are modelled appropriately so that the size of the resulting model will not be increased with ALID and ALID+VABC.

The time-history response of the structure under El Centro earthquake loading was carried out, and results were presented. Three types of radiating boundary conditions were included in the study: a). ABC, b). ALID and c). ALID+ABC. The SRM has been excluded from the study since the absorbing region length for 30 elements is only 0.33λ and the SRM method needs an absorbing region of length at least equal to the wavelength λ as discussed in Section 5.3.1.1. The displacement time history at the top centre of the building shows that the maximum displacement recorded at the top of the building for ABC, ALID, and ALID+VABC is 106 mm, 80.2 mm, and 76 mm, respectively, at 8.8, 8.94, and 8.95 seconds. This shows that the ALID+VABC produces less displacements compared to the ABC and ALID boundary conditions. Similarly, the maximum displacements for ABC, ALID, and ALID+VABC are 92.0 mm, 34.25 mm, and 30.29 mm, respectively.

The higher displacements in the case of ABC and ALID compared with ALID+VABC are due to trapped radiating waves inside the domain. This shows that the ALID+VABC absorbs the radiating waves more efficiently compared with ABC and ALID, even when the absorbing medium length is 0.33λ .

7. Summary

7.1 Summary

The importance of soil-structure interaction has been well established in the literature over the past four decades, which includes experimental, analytical, and numerical approaches. The numerical study of soil-structure-interaction problems has been widely used in recent years due to an increase in the computational capacity of finite element modelling. Radiating boundary conditions play a major role in the numerical analysis of soil-structure interactions. To address the radiating boundary conditions problem, researchers have developed various kinds of formulations over the past few decades, such as: a) Absorbing Boundary Conditions, b) Absorbing Layers techniques which include Perfectly Matched Layers, Caughey Absorbing Layer Method, Absorbing Layers by Increasing Damping and Stiffness Reduction Method, c). Boundary element method, and d). Infinite elements.

This study presents an efficient radiating boundary condition that combines the absorbing layers (ALID) and absorbing boundary conditions (ABC). The major drawback of this approach is the impedance mismatch between ABC and ALID. ABCs are derived based on elastic wave propagations, and therefore, these boundary conditions work only on the elastic moduli part of VABC layers. To achieve the coherence between these layers, first absorbing boundary conditions for viscoelastic wave propagation (VABC) were developed (details were presented in chapter 4), and later these boundary conditions damping properties were matched with ALID absorbing layers (details were presented in chapter 5).

Results were presented using 1D, 2D, and 3D numerical models with an explicit time integration scheme in chapters 4, 5, and 6, respectively. The numerical modelling includes parameters such as wave incident angle, wave frequency, structural natural frequency, type of explicit scheme, etc. The conclusions drawn from the results are summarized in the next section.

7.2 Conclusions

VABC works for Maxwell type viscoelastic wave propagation, i.e., mass proportional Rayleigh damping is only applied for numerical modelling, and the following conclusions were drawn from the study:

1. Standard ABC is yielding reflections when material damping is included, and the reflections are increasing as the damping increases. The proposed method produces very few or negligible reflections under viscoelastic wave propagation when the waves impinge on the boundary in the normal direction.
2. when using standard ABC in presence of material damping factious permanent deformations are developed in the numerical model. With the proposed approach, the deformations are in very good agreement with the extended mesh model.
3. When the wave impinges the boundary other than normal direction, both ABC and VABC produce reflections. But the displacements in case of VABC are better converging towards the extended mesh model. However, the difference in permanent deformation is small in the case of 2D models as radiation damping is present.

4. For higher damping ratios i.e., above 10%, the performance of the proposed boundary conditions is degrading. It is also concluded that reflections aggregating at higher damping ratios increase with the analysis time. This suggests that the VABC convergence needs to be improved for higher damping ratios.
5. The procedure applied in the method does not converge when stiffness proportional damping is present. Therefore, the stiffness proportional damping terms are dropped in the final equations. If stiffness proportional damping is present in the domain, there is no advantage in using this method.

Later, a method for radiating boundary conditions was developed by combining the absorbing layers and Absorbing Boundary Conditions for viscoelastic wave propagation (ALID+VABC). The following conclusions were drawn from the study:

1. The additional cost of adding the ABC to ALID is very little, but the efficiency is improved many folds. The performance of ALID is poor when the absorbing region length is 1.5λ , which produces nearly 5% reflections, and the percentage of reflections increases to more than 50% if the absorbing region length is 0.33λ even when the wave is propagating in the normal direction to the boundary.
2. SRM approach works best when the absorbing region length is 1.5λ , but performs poor when the absorbing region length is less than λ . These two methods require many layers, especially if the mesh size in the domain is small. The present method overcomes this difficulty and performs well when the absorbing region length is 0.5λ or more.
3. The performance of ALID, SRM, and ALID+VABC degrades if the numerical model is subjected to a lower frequency than the designed frequency but performs excellently at higher incident frequencies.
4. The proposed approach uses features that are readily available in many commercial programs, such as LsDyna and Oasys GSA used in this investigation, but the novel feature here is assigning the correct setup and damping properties. The efficiency is slightly compromised when using the commercial software, as the software uses velocities computed in the middle of timesteps.

7.3 Limitations of the Study

The following are the limitations of this study:

- The VABC is efficient for low mass proportion damping and produces reflections for higher damping.
- The VABC cannot be used for stiffness proportional damping and other than Raileigh damping.
- The VABC cannot be used for soil material with hysteresis damping.
- The VABC produces reflections when imping other than normal direction
- The method cannot be used for nonlinear materials.
- The ALID+VABC works excellently for wave impingement in the normal direction. However, all the existing absorbing layer methods, including the present method, are very poor at absorbing wave energy when the wave is propagating at a higher inclination angle than its normal direction.

7.4 Suggestions for future work

The following suggestions are made for future work in this study:

- The VABC absorbing boundaries can be extended to include the stiffness proportional so that the boundaries can be applied to the materials with Raileigh damping.
- The VABC absorbing boundaries may be further extended to include the elastic-plastic hysteresis damping.
- The absorbing layers produce more reflections when the wave impinges at an angle greater than 45 degrees. The work produces excellent results if the absorbing layers can be improved so that there will not be any reflections when the waves propagate in directions other than normal.
- A detailed study may be carried out to provide guidelines on the soil domain size, i.e., the depth of the soil model from the foundation, based on parameters such as the height of the structure, type of absorbing boundary conditions, load, and natural frequencies of the structure.

7.5 Research Contributions

Published Journals:

1. Badry R.S., Pradeep Kumar R., (2018); *Local absorbing boundary conditions to simulate wave propagation in unbounded viscoelastic domains*. Comput Struct; 2018:1-16
2. Badry R.S., Maruthi Kott, Pradeep Kumar R., (2018) A Comparative Study of Absorbing Layer Methods to Model Radiating Boundary Conditions for the Wave Propagation in Infinite Medium, International Journal of Engineering & Technology 7 (3.35) (2018) 25-29"

Published Conferences:

1. Badry R.S., Pradeep Kumar R., (2018) Numerical Modelling of Radiating Boundary Conditions Combined with Modified Absorbing Boundary Condition for Viscoelastic Wave Propagation. International Conference on CST-2018. Sitges, Spain, Barcelona, 4-6 Sep, 2018.
2. Badry R.S., Pradeep Kumar R., (2018) Numerical Modelling of Radiating Boundary Conditions Combined for Wave Propagation in Nonlinear Unbounded Domain, 17th International Symposium on New Technologies for Urban safety of Mega Cities in Asia.At: IIIT- H, Hyderabad, India"

Submitted Journal:

1. Badry R.S., Pradeep Kumar R., *Numerical Modelling of Radiating Boundary Conditions Combined with Modified Absorbing Boundary Condition for Viscoelastic Wave Propagation*; Comput Struct;

8. References:

- [1] Anderson D.L., Ungless R.L., (1977); *Infinite Finite Elements*, International Symposium on Innovative Numerical Analysis in Applied Engineering Science, France
- [2] Astley, R. J., (2000); "Infinite elements for wave problems: A review of current formulations and an assessment of accuracy", *International Journal for Numerical Methods in Engineering*; 49: 951–976.
- [3] Badry R.S., Pradeep Kumar R., (2018); *Local absorbing boundary conditions to simulate wave propagation in unbounded viscoelastic domains*. *Comput Struct*; 2018:1-16
- [4] Badry R.S., Pradeep Kumar R., (2018); *Numerical Modelling of Radiating Boundary Conditions Combined with Modified Absorbing Boundary Condition for Viscoelastic Wave Propagation*. International Conference on CST-2018. Sitges, Spain, Barcelona, 4-6 Sep, 2018.
- [5] Banerjee, P.K., Butterfield, R., (1981), *Boundary element methods in engineering science*. McGraw-Hill Book Co.
- [6] Basu U. (2009); *Explicit finite element perfectly matched layer for transient three-dimensional elastic waves*. *International Journal for Numerical Methods in Engineering*; 77(2):151–176.
- [7] Bathe K.J., (2010); *Finite Element Procedures*, Pearson Education, Indian branch, New Delhi, India.
- [8] Berenger, J.P., (1994); *A perfectly matched layer for the absorption of electromagnetic waves*. *Journal of Computing in Physics*; 114(2):185–200.
- [9] Beskos, D. E. (1997); *Boundary element methods in dynamic analysis: Part II (1986-1996)*. *Applied Mechanics Reviews*, ASME, 50:149–19
- [10] Bettess P., (1978); *Infinite elements*, *International Journal for Numerical Methods in Engineering*; 11:54-64.
- [11] Bielak J., Loukakis K., Hisada Y. & Yoshimura C. (2003), *Domain Reduction Method for Three-Dimensional Earthquake Modeling in Localized Regions, Part I: Theory*. *Bulletin of the Seismological Society of America*; 93(2): 817-824.
- [12] Carcione JM, Kosloff D, and Kosloff R., (1988); *Wave propagation simulation in a linear viscoelastic medium*. *Geophysical Journal*, 95: 597–611
- [13] Carpenter, N. J., Taylor, R. L. and Katona, M. G. (1991); *Lagrange constraints for transient finite element surface contact*. *Int. J. Numer. Meth. Engng.*, 32: 103-128
- [14] Celep Z, Bazant ZP., (1983); *Spurious reflection of elastic waves due to gradually changing finite element size*, *Int, J. Num. Meth. in Eng*; 19:631–646
- [15] Chen Junwei, Shou Yundong, Zhou Xiaoping., (2022); *Implementation of the novel perfectly matched layer element for elastodynamic problems in time-domain finite element method*, *Soil Dynamics and Earthquake Engineering*
- [16] Chen Xiamoing, Duan Jin, Li Yungui., (2015); *Mass proportional damping in nonlinear time-history analysis*, 3rd International Conference on Material, Mechanical and Manufacturing Engineering (IC3ME 2015); 567-571
- [17] Chew W.C., Liu Q.H., (1996); *Perfectly matched layers for elastodynamics: a new absorbing boundary condition*, *Journal of Computational Acoustics*; 4(4): 341-359.
- [18] Cohen M. (1980); *Silent boundary methods for transient wave analysis*, PhD Thesis, California Institute of Technology.

- [19] Collino F., Tsogka C., (2001); *Application of the PML absorbing layer model to the linear elastodynamic problem in anisotropic heterogeneous media*, Geophysics; 66(1): 294-307.
- [20] Desai, C. S., Zaman, M. M., Lightner, J. G. and Siriwardane, H. J., (1984) ; Thin layer element for interfaces and joints. *Int. J. Numer. Anal. Meth. Geomech.*, 8: 19-43.
- [21] Engquist B. and Majda A., (1977); *Absorbing boundary conditions for the numerical simulation of waves*, *Mathematics of Computation*; 31: 629–651
- [22] Goodman R. E., Taylor R. L., and Brekke T. L., (1968) ; *A model for the mechanics of jointed rock*, *Journal of the Soil Mechanics and Foundations Division*, 94:637–660
- [23] Hall, W. S. and Oliveto, G. (2003); *Boundary Element Methods for Soil-Structure Interaction*. Kluwer Academic Publishers.
- [24] Hallquist J.O., Goudreau G.L., Benson D. J., (1985); Sliding interfaces with contact-impact in large-scale Lagrangian computations, *Computer Methods in Applied Mechanics and Engineering*; 51: 107-13.
- [25] Han H., Yin D., (2007); *Absorbing boundary conditions for the multidimensional Klein-Gordon equation*. *Commun. Math. Sci.*; 5(3), 743-764.
- [26] Han H., and Zhang, Z., (2008); *Split local absorbing conditions for one-dimensional nonlinear Klein-Gordon equation on unbounded domain*. *Journal of Computing in Physics*; 227(20):8992–9004.
- [27] Israeli M. and Orszag S.A., (1981); *Approximation of radiation boundary conditions*, *J. Comp. Phys*; vol. 41: 115-135.
- [28] Katona, M. G., (1983); *A simple contact–friction interface element with applications to buried culverts*. *Int. J. Numer. Anal. Meth. Geomech.*, 7: 371-384
- [29] Kellezi L., (1998); *Dynamic soil-structure interaction transmitting boundary for transient analysis*, PhD Thesis, Department of Structural Engineering and Materials, Technical University of Denmark.
- [30] Kramer, S. L., (2003); “Geotechnical Earthquake Engineering”. Pearson Education, Indian branch, New Delhi, India.
- [31] Komatitsch D., Martin R., (2007); *An unsplit convolutional Perfectly Matched Layer improved at grazing incidence for the seismic wave equation*. *Geophysics*; 72(5): 155-167.
- [32] Li H., and Wu X., (2011); *Local absorbing boundary conditions for nonlinear wave equation on unbounded domain*, *Phys. Rev. E* (84), 036707,
- [33] Lindman E.L., (1975) ; “Free-space” boundary conditions for the time dependent wave equation, *Journal of Computational Physics* ;18(1) :66-78,
- [34] Liu, J., Du, Y., Du, X., Wang, Z., and Wu, J. (2006). "3D viscous-spring artificial boundary in time domain." *Earthquake Engineering and Engineering Vibration*, 5 (1), 93-102.
- [35] Lysmer J., Kuhlemeyer R.L., (1969); *Finite dynamic model for infinite media*. *Journal of Engineering Mechanics. Div ASCE* 95(EM4):859–877.
- [36] Maheshwari, B. K., Truman, K. Z., El Naggar, M. H. and Gould, P. L., (2004) ; *Three dimensional finite element nonlinear dynamic analysis of pile groups for lateral transient and seismic excitations*, *Canadian Geotechnical Journal* ; 41: 118-133.
- [37] Marcinkovich C., Olsen K.B., (2003); *On the implementation of perfectly matched layers in a three-dimensional fourth-order velocity-stress finite difference scheme*, *Journal of Geophysical Research*; 108(B5): 2276.
- [38] Meza-Fajardo K.C., Papageorgiou A.S., (2008); *A Nonconvolutional, Split-Field, Perfectly Matched Layer for Wave Propagation in Isotropic and Anisotropic Elastic Media: Stability Analysis*, *Bulletin of the Seismological Society of America*; 98(4): 1811-1836.

- [39] Mur G. (1981); *Absorbing boundary conditions for the finite difference approximation of the time domain electromagnetic-field equations*, IEEE Transactions on Electromagnetic Compatibility; 23:377–382,
- [40] Oasys GSA 9.0., (2018); Oasys Ltd., London, England,
- [41] Oden J.T., and Pires E.B., (1984); *Nonlocal friction in contact problems in plane elasticity*, Finite Elements, Vol. 5, Special Problems in Solid Mechanics, Prentice-Hall, Inc.
- [42] Pettit J. R., Walker A., Cawley P., and Lowe M. J. S., (2014); *A Stiffness Reduction Method for efficient absorption of waves at boundaries for use in commercial Finite Element codes*, Ultrasonics; 54(7): 1868-1879.
- [43] Rajagopal P., Drozd M., Skelton E.A., Lowe M.J.S., Craster R.V., (2012); *On the use of absorbing layers to simulate the propagation of elastic waves in unbounded isotropic media using commercially available finite element packages*, NDT&E Int. 51:30–40.
- [44] Rodrigues A. and Dimitrovova Z., (2015); *The Caughey absorbing layer method – implementation and validation in Ansys software*, Latin American Journal of Solids and Structures; 12: 540-1564.
- [45] Saeed Izadian, Kamal Aghazade, Navid Amini, Yanghua Wang, *Semi-exact local absorbing boundary condition for seismic wave simulation*, Journal of Geophysics and Engineering, Volume 18, Issue 1, February 2021, Pages 62–73,
- [46] Sembalt J.F., Lenti L., Ali G. (2010); *A simple multi directional Absorbing Layer method to simulate elastic wave propagation in unbounded domains*, International Journal for Numerical methods in engineering; 1: 1-22.
- [47] Simo J.C., Wriggers P., and Taylor R.L., (1985); *A perturbed Lagrangian formulation for the finite element solution of contact problems*; Comp. Meth. Appl. Mech. Engng.; 50:163-180.
- [48] Sommerfeld, A., (1949); *Partial Differential Equations in Physics (Vol. 1)*. Academic Press.
- [49] Ting T.C.T., (1968); *Elastic-plastic boundaries in plane and cylindrical wave propagation of combined stresses*, Technical report 194, Dept of App. Mech.,
- [50] Ting T.C.T., (1976); *Wave speeds and slowness surface in elastic-plastic media obeying Tresca's yield condition*, Proceedings of 13th Annual Meeting Society of Engineering Science Sponsored by JIAFS Hampton, VA, November 1-3
- [51] Ungless R.L., (1973); *An Infinite Finite Element*, MA.Sc. thesis. University of British Columbia, Canada.
- [52] von Karman T., and Duwez P., (1950); *The propagation of plastic deformation in solids*. J. App. Phys.; 21:987-994.
- [53] White W., Villiappan S., Lee I.K., (1977); *Unified boundary for finite dynamic models*, Journal of the Engineering Mechanics Division, ASCE 103(EM5); 949-964.
- [54] Wolf J. P., (1985); *Dynamic Soil-Structure Interaction*. Prentice-Hall, Inc., Englewood Cliffs, New Jersey.
- [55] Yang H., Sinha, S. K. Feng Y., McCallen D. B., Jeremić B., (2018); *Energy dissipation analysis of elastic–plastic materials*. Computer Methods in Applied Mechanics and Engineering. 331, 309–326
- [56] Yoshimura C., Bielak J., Hisada Y. & Fernández A. (2003), “Domain Reduction Method for Three-Dimensional Earthquake Modeling in Localized Regions, Part II: Verification and Applications”, Bulletin of the Seismological Society of

America; 93(2):825-840

- [57] Yun C. B., Kim J.M., Yao Z.H., Yuan M.W., (2007); *Dynamic Infinite Elements for Soil-Structure Interaction Analysis in a Layered Soil Medium*, Comp. Methods In Engg and Science; 153-167
- [58] Zhicheng, X., Qiang, P., Shuang, W., and Changfeng, P. (2016). "*Input seismic motion based on the viscous-spring boundary: Analytical solution and numerical simulation*". International Journal of u-and e-Service, Science and Technology, 9 (6), 59-68.
- [59] Zienkiewicz O. C, Bettess P., (1976); *Infinite Element in the Study of Fluid-Structure Interaction Problems, Lecture Notes in Physics*, 58, Eds. Ehlers J. et al. Springer-Verlag, Berlin.
- [60] Zienkiewicz O. C., Bando K., Bettess P., Emson C. and Chiam T. C., (1985); *Mapped infinite elements for exterior wave problems*. International Journal for Numerical Methods in Engineering; 21:1229–1251.

APPENDIX A: Finite Element Formulation

A.1: Finite Element Formulation for 8-Node brick element

The stiffness and mass matrix for an 8-Node brick element is computed as follows

$$K^e = \int_v B^T D B dv$$

$$M^e = \int_v H^T \rho H dv$$

Where, B is strain-displacement matrix, D is elastic stress-strain matrix of the material. To generate a stiffness matrix for an element, integration must be performed over an element which may not be perfect cuboid. To avoid the difficulties in regular integration over the element, a numerical integration is performed transforming the regular element into Isoparametric element.

Consider a 3-D brick Isoparametric element with parent co-ordinate system ξ, η, μ . The shape functions have been introduced to map the cuboidal shape into the actual shape of the element with the coordinate system x, y, z

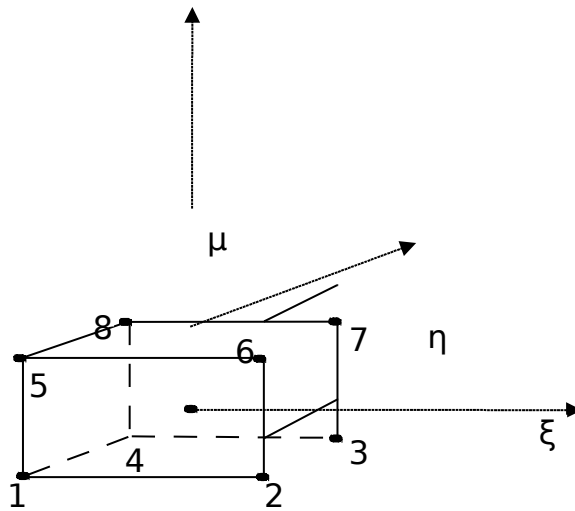


Figure A-1: 8 noded 3-D brick element in parent coordinate system

The shape function matrix H^m for 8 noded Isoparametric element is 3×24 matrix as presented as follows

$$H^m = \begin{bmatrix} H_1 & 0 & 0 & H_2 & 0 & 0 & \dots & H_8 & 0 & 0 \\ 0 & H_1 & 0 & 0 & H_2 & 0 & \dots & 0 & H_8 & 0 \\ 0 & 0 & H_1 & 0 & 0 & H_2 & \dots & 0 & 0 & H_8 \end{bmatrix}$$

Where H_i is the shape function and they can be defined for the brick element is as follows

$$H_1 = \frac{1}{8}(1-\xi)(1-\eta)(1-\mu) \quad H_2 = \frac{1}{8}(1+\xi)(1-\eta)(1-\mu)$$

$$H_3 = \frac{1}{8}(1+\xi)(1+\eta)(1-\mu) \quad H_4 = \frac{1}{8}(1-\xi)(1+\eta)(1-\mu)$$

$$H_5 = \frac{1}{8}(1-\xi)(1-\eta)(1+\mu) \quad H_6 = \frac{1}{8}(1+\xi)(1-\eta)(1+\mu)$$

$$H_7 = \frac{1}{8}(1+\xi)(1+\eta)(1+\mu) \quad H_8 = \frac{1}{8}(1-\xi)(1+\eta)(1+\mu)$$

These shape function formulae can be summarized as

$$H_i = \frac{1}{8}(1+\xi\xi_i)(1+\eta\eta_i)(1+\mu\mu_i)$$

The strain-displacement matrix B of an element can be defined as

$$B = \frac{\partial H}{\partial x}$$

Where x represents the directions i.e., x , y , and z . The above equation expands to

$$B = \begin{bmatrix} \frac{dH_1}{dx} & 0 & 0 & \frac{dH_2}{dx} & 0 & 0 & \dots & \frac{dH_N}{dx} & 0 & 0 \\ 0 & \frac{dH_1}{dy} & 0 & 0 & \frac{dH_2}{dy} & 0 & \dots & 0 & \frac{dH_N}{dy} & 0 \\ 0 & 0 & \frac{dH_1}{dz} & 0 & 0 & \frac{dH_2}{dz} & \dots & 0 & 0 & \frac{dH_N}{dz} \\ \frac{dH_1}{dy} & \frac{dH_1}{dx} & 0 & \frac{dH_2}{dy} & \frac{dH_2}{dx} & 0 & \dots & \frac{dH_N}{dy} & \frac{dH_N}{dx} & 0 \\ 0 & \frac{dH_1}{dz} & \frac{dH_1}{dy} & 0 & \frac{dH_2}{dz} & \frac{dH_2}{dy} & \dots & 0 & \frac{dH_N}{dz} & \frac{dH_N}{dy} \\ \frac{dH_1}{dz} & 0 & \frac{dH_1}{dx} & \frac{dH_2}{dz} & 0 & \frac{dH_2}{dx} & \dots & \frac{dH_N}{dz} & 0 & \frac{dH_N}{dx} \end{bmatrix}$$

The strain-displacement matrix can be expanded to the terms of Isoparametric dimension ξ , η , and μ as follows

$$B = \frac{\partial H}{\partial x} = \frac{\partial \xi}{\partial x} \frac{\partial H}{\partial \xi}$$

The above equation expands to

$$B = J^{-1} \frac{dH}{d\xi}$$

Where $\frac{dH}{d\xi}$ is estimated as

$$\frac{dH}{d\xi} = \begin{bmatrix} \frac{dH_1}{d\xi} & 0 & 0 & \frac{dH_2}{d\xi} & 0 & 0 & \frac{dH_8}{d\xi} & 0 & 0 \\ 0 & \frac{dH_1}{d\eta} & 0 & 0 & \frac{dH_2}{d\eta} & 0 & \dots & 0 & \frac{dH_8}{d\eta} & 0 \\ 0 & 0 & \frac{dH_1}{d\mu} & 0 & 0 & \frac{dH_2}{d\mu} & 0 & 0 & 0 & \frac{dH_8}{d\mu} \\ \frac{dH_1}{d\eta} & \frac{dH_1}{d\xi} & 0 & \frac{dH_2}{d\eta} & \frac{dH_2}{d\xi} & 0 & \frac{dH_8}{d\eta} & \frac{dH_8}{d\xi} & 0 & 0 \\ 0 & \frac{dH_1}{d\mu} & \frac{dH_1}{d\eta} & 0 & \frac{dH_2}{d\mu} & \frac{dH_2}{d\eta} & \dots & 0 & \frac{dH_8}{d\mu} & \frac{dH_8}{d\eta} \\ \frac{dH_1}{d\mu} & 0 & \frac{dH_1}{d\xi} & \frac{dH_2}{d\mu} & 0 & \frac{dH_2}{d\xi} & \frac{dH_8}{d\mu} & 0 & 0 & \frac{dH_8}{d\xi} \end{bmatrix}$$

Where $\frac{\partial \xi_j}{\partial x_j}$ can be written in terms of Jacobian matrix, and it can be defined as

$$J = \frac{\partial x}{\partial \xi} = \begin{bmatrix} \frac{dx}{d\xi} & \frac{dy}{d\xi} & \frac{dz}{d\xi} \\ \frac{dx}{d\eta} & \frac{dy}{d\eta} & \frac{dz}{d\eta} \\ \frac{dx}{d\mu} & \frac{dy}{d\mu} & \frac{dz}{d\mu} \end{bmatrix} = \frac{dH}{d\xi} x$$

Where, x is elemental nodal co-ordinates and can be defined as.

$$x^T = \{x_1 y_1 z_1 x_2 y_2 z_2 \dots x_8 y_8 z_8\}$$

The stiffness matrix and mass matrix can be estimated using gaussian numerical integration

$$K^e = \sum_{\xi, \eta, \mu=1}^2 w_\xi w_\eta w_\mu B^T DB |J|$$

$$M^e = \sum_{\xi, \eta, \mu=1}^2 w_\xi w_\eta w_\mu H^T \rho H |J|$$

Where, w_ξ , w_η , and w_μ are the integration weights in ξ , η , and μ directions, which are equal to 1 for normal integration of 8-node Isoparametric elements and the corresponding locations $\pm \frac{1}{\sqrt{3}}$. $|J|$ is the determinant of the Jacobian matrix. In explicit dynamic analysis the mass matrix is made diagonal by using lumping of the mass on to the diagonal terms using Horizontal or Vertical mass lumping technique.

The element stiffness and mass matrix K^e and M^e are in element local axis system. These matrices has to rotate to global axis before assembling into global stiffness and mass matrices.

A.2: 4-Node quadrilateral element for plane strain condition

The finite element formulation for 4-Node quadrilateral elements for pane strain condition is like 8-Node brick element considering 2-dimension only. The stiffness and mass matrix for the element is computed as follows

$$K^e = \int_v^{\square} B^T DB dv$$

$$M^e = \int_v^{\square} H^T \rho H dv$$

Consider a 2-D Isoparametric element with parent co-ordinate system ξ, η .

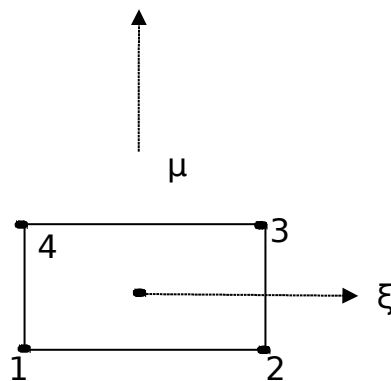


Figure A-2: 4-Node quadrilateral element

The shape function matrix H^m for 8 noded Isoparametric element is 3 x 24 matrix as presented as follows

$$H^m = \begin{bmatrix} H_1 & 0 & H_2 & 0 & \dots & H_8 & 0 \\ 0 & H_1 & 0 & H_2 & \dots & 0 & H_8 \end{bmatrix}$$

Where H_i is the shape function and they can be defined for the brick element is as follows

$$H_1 = \frac{1}{4}(1 - \xi)(1 - \eta) \quad H_2 = \frac{1}{4}(1 + \xi)(1 - \eta)$$

$$H_3 = \frac{1}{4}(1 + \xi)(1 + \eta) \quad H_4 = \frac{1}{4}(1 - \xi)(1 + \eta)$$

These shape function formulae can be summarized as

$$H_i = \frac{1}{4}(1 + \xi \xi_i)(1 + \eta \eta_i)$$

The strain-displacement matrix B of an element can be defined as

$$B = J^{-1} \frac{dH}{d\xi}$$

Where $\frac{dH}{d\xi}$ is estimated as

$$\frac{dH}{d\xi} = \begin{bmatrix} \frac{dH_1}{d\xi} & 0 & \frac{dH_2}{d\xi} & 0 & \frac{dH_4}{d\xi} & 0 \\ 0 & \frac{dH_1}{d\eta} & 0 & \frac{dH_2}{d\eta} & \dots & 0 \\ \frac{dH_1}{d\eta} & \frac{dH_1}{d\xi} & \frac{dH_2}{d\eta} & \frac{dH_2}{d\xi} & \frac{dH_4}{d\eta} & \frac{dH_4}{d\xi} \end{bmatrix}$$

Where $\frac{\partial \xi_j}{\partial x_j}$ can be written in terms of Jacobian matrix, and it can be defined as

$$J = \frac{\partial x}{\partial \xi} = \begin{bmatrix} \frac{dx}{d\xi} & \frac{dy}{d\xi} \\ \frac{dx}{d\eta} & \frac{dy}{d\eta} \end{bmatrix} = \frac{dH}{d\xi} x$$

Where, x is elemental nodal co-ordinates and can be defined as.

$$x^T = [x_1 \ y_1 \ x_2 \ y_2 \ \dots \ x_4 \ y_4]$$

The stiffness matrix and mass matrix can be estimated using gaussian numerical integration like 8-Node brick element using only in 2 dimensions.

A-3: Formulation of beam element

Consider the 2 Noded beam element with 6 DOFs 3 translations and 3 rotations.

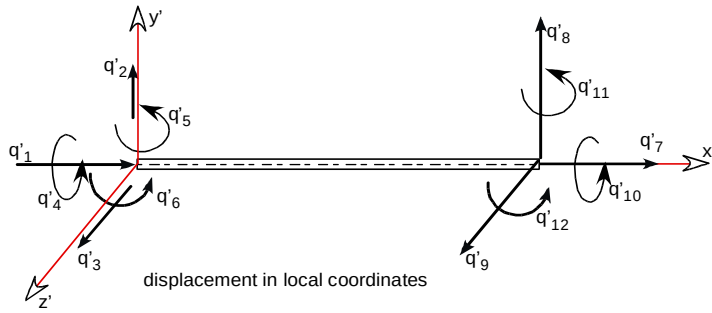


Figure A-3: 3-D beam element

The stiffness matrix of the beam element can be formulated by considering the modes of bending in the following figure.

The elemental stiffness matrix for the beam element without considering shear effects can be given as follows considering the 6 DOFs at each node.

$$K = E \begin{bmatrix}
\frac{A}{l} & 0 & 0 & 0 & 0 & 0 & -\frac{A}{l} & 0 & 0 & 0 & 0 & 0 \\
0 & \frac{12I_{yy}}{l^3} & 0 & 0 & 0 & \frac{6I_{yy}}{l^2} & 0 & -\frac{12I_{yy}}{l^3} & 0 & 0 & 0 & \frac{6I_{yy}}{l^2} \\
0 & 0 & \frac{12I_{zz}}{l^3} & 0 & -\frac{6I_{zz}}{l^2} & 0 & 0 & 0 & -\frac{12I_{zz}}{l^3} & 0 & -\frac{6I_{zz}}{l^2} & 0 \\
0 & 0 & 0 & \frac{GJ}{El} & 0 & 0 & 0 & 0 & 0 & -\frac{GJ}{El} & 0 & 0 \\
0 & 0 & -\frac{6I_{zz}}{l^2} & 0 & \frac{4I_{zz}}{l} & 0 & 0 & 0 & \frac{6I_{zz}}{l^2} & 0 & \frac{2I_{zz}}{l} & 0 \\
0 & \frac{6I_{yy}}{l^2} & 0 & 0 & 0 & \frac{4I_{yy}}{l} & 0 & \frac{6I_{yy}}{l^2} & 0 & 0 & 0 & \frac{2I_{yy}}{l} \\
-\frac{A}{l} & 0 & 0 & 0 & 0 & 0 & \frac{A}{l} & 0 & 0 & 0 & 0 & 0 \\
0 & -\frac{12I_{yy}}{l^3} & 0 & 0 & 0 & \frac{6I_{yy}}{l^2} & 0 & \frac{12I_{yy}}{l^3} & 0 & 0 & 0 & -\frac{6I_{yy}}{l^2} \\
0 & 0 & -\frac{12I_{zz}}{l^3} & 0 & \frac{6I_{zz}}{l^2} & 0 & 0 & 0 & \frac{12I_{zz}}{l^3} & 0 & \frac{6I_{zz}}{l^2} & 0 \\
0 & 0 & 0 & -\frac{GJ}{El} & 0 & 0 & 0 & 0 & 0 & \frac{GJ}{El} & 0 & 0 \\
0 & 0 & -\frac{6I_{zz}}{l^2} & 0 & \frac{2I_{zz}}{l} & 0 & 0 & 0 & \frac{6I_{zz}}{l^2} & 0 & \frac{4I_{zz}}{l} & 0 \\
0 & \frac{6I_{yy}}{l^2} & 0 & 0 & 0 & \frac{2I_{yy}}{l} & 0 & -\frac{6I_{yy}}{l^2} & 0 & 0 & 0 & \frac{4I_{yy}}{l}
\end{bmatrix}$$

The mass matrix is

$$M = \frac{\rho Al}{420} \begin{bmatrix}
140 & 0 & 0 & 0 & 0 & 0 & 70 & 0 & 0 & 0 & 0 & 0 \\
0 & 156 & 0 & 0 & 0 & 22l & 0 & 54 & 0 & 0 & 0 & -13l \\
0 & 0 & 156 & 0 & -22l & 0 & 0 & 0 & 54 & 0 & 13l & 0 \\
0 & 0 & 0 & 140\frac{J}{A} & 0 & 0 & 0 & 0 & 0 & 70\frac{J}{A} & 0 & 0 \\
0 & 0 & -22l & 0 & 4l^2 & 0 & 0 & 0 & -13l & 0 & -3l^2 & 0 \\
0 & 22l & 0 & 0 & 0 & 4l^2 & 0 & 13l & 0 & 0 & 0 & -3l^2 \\
70 & 0 & 0 & 0 & 0 & 0 & 140 & 0 & 0 & 0 & 0 & 0 \\
0 & 54 & 0 & 0 & 0 & 13l & 0 & 156 & 0 & 0 & 0 & -22l \\
0 & 0 & 54 & 0 & -13l & 0 & 0 & 0 & 156 & 0 & 22l & 0 \\
0 & 0 & 0 & 70\frac{J}{A} & 0 & 0 & 0 & 0 & 0 & 140\frac{J}{A} & 0 & 0 \\
0 & 0 & 13l & 0 & -3l^2 & 0 & 0 & 0 & 22l & 0 & 4l^2 & 0 \\
0 & -13l & 0 & 0 & 0 & -3l^2 & 0 & -22l & 0 & 0 & 0 & 4l^2
\end{bmatrix}$$

As stated in section A.1, the consistent mass matrix defined above usually lumped on to the diagonal nodes for explicit dynamic analysis.